PEOPLE'S DEMOCRATIC REPUBLIC OF ALGERIA

MINISTRY OF HIGHER EDUCATION AND SCIENTIFIC RESEARCH

FERHAT ABBAS UNIVERSITY – SETIF -1-

THESIS

Submitted to Institute of Optics and Precision Mechanics for the degree of

Doctorate 3rd Cycle –LMD

In Applied Optics and Photonics

By

Younes Slimi

Title

Optical, Electronical and Structural Study of Scandium Aluminum Nitride Alloy for Optoelectronic Applications

Defended on : 03/12/2023.
In front of the composed committee of

Chairman	**Nabil Belkhir**	**Professor**	**UFAS- Setif -1**
Supervisor	**Mohamed Bouafia**	**Professor**	**UFAS Setif -1**
Co-Supervisor	**Stefan Krischok**	**Professor**	**Technical University of Ilmenau-Germany**
Examiner	**Aïssa Manallah**	**Professor**	**UFAS Setif -1**
Examiner	**Abderrahmane Bouabellou**	**Professor**	**University of Constantine-1**

REPUBLIQUE ALGERIENNE DEMOCRATIQUE ET POPULAIRE

MINISTERE DE L'ENSEIGNEMENT SUPERIEUR ET DE LA RECHERCHE SCIENTIFIQUE

UNIVERSITÉ FARHAT ABBAS SETIF-1-

THÈSE

Soumis à l'Institut d'Optique et de Mécanique de Précision pour le grade de doctorat 3éme cycle–LMD

En optique et Photonique Appliquées

Présenté par

Younes Slimi

Titre

Etude optique, électronique et structural de l'alliage de nitrure d'aluminium scandium pour application optoélectroniques.

Soutenue le : 03/12 /2023

Président	**Nabil Belkhir**	**Professeur**	**UFAS- Sétif -1**
Encadrant	**Mohamed Bouafia**	**Professeur**	**UFAS Sétif -1**
Co-encadrant	**Stefan Krischok**	**Professeur**	**Université d'Ilmenau-Allemagne**
Examinateur	**Aïssa Manallah**	**Professeur**	**UFAS Sétif -1**
Examinateur	**Abderrahmane Bouabellou**	**Professeur**	**Université de Constantine-1**

الملخص

هذه الأطروحة، تقدم دراسة حول طبقات $Sc_XAl_{X-1}N$ المتناثرة لاستخدامها في تطبيقات الإلكترونيات الضوئية فوق البنفسجية بشكل رسمي، والصمامات الثنائية الباعثة للضوء LEDs والصمام الثنائي الليزر فوق البنفسجي-UV .
LED

بإضافة كمية معينة من سكانديوم إلى الهيكل السداسي لAlN الموضوعة على قاعدة السليسيوم(111) Si، نرى تغييرات في طبيعة المركب في نظام المواد.

يسمح التحليل الطيفي للانبعاث الضوئي بالأشعة السينية، الذي تم تنفيذه في هذا العمل، بتحديد النسبة المئوية x من السكانديوم في عيناتنا .يتم تحديد معلمة الشبكة c ل $Sc_XAl_{X-1}N$ السداسية بالاعتماد على x بواسطة حيود الأشعة السينية. بالإضافة إلى ذلك، يعتبر التحليل الطيفي للأشعة المرئية وفوق البنفسجية وقياس القطع الطيفي من الخصائص البصرية المستخدمة لتحديد طاقة الربط ومعامل الامتصاص لنتريد الألومنيوم سكانديوم .علاوة على ذلك، يتم إجراء التحليل الطيفي بالأشعة تحت الحمراء للحصول على نظرة عامة مفصلة عن تطور النطاقات الاهتزازية في
$Sc_XAl_{X-1}N$ كدالة لx.

ScAlNهي مادة مركبة ذات أهمية كبيرة خاصة في التطبيقات الكهرو ميكانيكية والإلكترونية الضوئية .نظرًا لخصائصه الضوئية التي تؤثر على تأثيرات معظم الخواص الكهربائية والميكانيكية، فإن حساب الخصائص المذكورة سابقًا له أهمية قصوى .لتحقيق هذا الهدف تم اختبار العديد من النظريات لنمذجة هذه الخصائص؛ سيعرض هذا العمل طريقة العناصر المحدودة، ونظرية رايلي-رايس، والتقريب المتوسط الفعال EMA .يتكون هذا العمل من محاكاة معلمات ScAlN من أجل تحسين خصائص الصمام الثنائي الباعث للضوء .لهذا الغرض، يتم استخدام برنامج GVDMلمحاكاة المواد المدروسة في نظام LED تم بذل جهود كبيرة لتكييف متطلباتنا مع البرنامج وتحقيق أفضل نتيجة ممكنة مع البيانات من المواد المستخدمة .كانت النتائج التي تم الحصول عليها مرضية ومتوافقة مع الجزء النظري

Abstract

This manuscript presents a study on sputtered $Sc_xAl_{1-x}N$ layers for use in ultraviolet optoelectronics applications such as light-emitting diodes (LEDs) and ultraviolet laser diodes (UV-LDs). By adding a certain amount of scandium into the hexagonal structure of AlN deposed on silicon Si (111) substrate, changes in the compound can be observed. In this work, X-ray photoemission Spectroscopy (XPS) is used to determine the concentration of Scandium in the samples. The lattice parameter c of hexagonal $Sc_xAl_{1-x}N$ is determined by X-ray diffraction (DRX). Optical characterizations such as UV-VIS spectroscopy and spectroscopic ellipsometry (SE) are used to determine the binding energy and absorption coefficient of scandium aluminum nitride. Scanning Electron Microscopy (SEM) is used to determine the roughness of the samples and to analyze the morphology of the ScAlN. Energy Dispersive X-ray (EDS) is used to characterize a sample's chemical characteristics or determine its element composition.

Additionally, infrared spectroscopy is performed to obtain a detailed overview of the vibrational bands in $Sc_xAl_{1-x}N$, as a function of x. ScAlN is a composite material of great interest, particularly in electromechanical and optoelectronic applications where its optical properties influence most electrical and mechanical properties. To model these properties, several theories such as the finite element method, the Rayleigh-Rice theory, and the effective medium approximation (EMA) were tested. This work focuses on simulating ScAlN parameters to improve the properties of a light-emitting diode. For this purpose, the GPVDM software is used to simulate the studied materials in an LED system. Considerable efforts were made to adapt the requirements to the software to achieve the best possible result with the data from the material used. The results obtained were satisfactory and in agreement with the literature.

Résumé

Ce manuscrit présente une étude sur les couches $Sc_xAl_{1-x}N$ pulvérisées destinées à être utilisées dans des applications optoélectroniques ultraviolettes telles que les diodes électroluminescentes (DEL) et les diodes laser ultraviolettes (UV-LD). En ajoutant une certaine quantité de scandium dans la structure hexagonale de l'AlN déposée sur un substrat de silicium Si (111), des modifications du composé peuvent être observées. Dans ce travail, la spectroscopie de photoémission de rayons X (XPS) est utilisée pour déterminer la concentration de scandium dans les échantillons. Le paramètre de réseau c de l'hexagonal $Sc_xAl_{1-x}N$ est déterminé par diffraction des rayons X (DRX). Des caractérisations optiques telles que la spectroscopie UV-VIS et l'ellipsométrie spectroscopique (SE) sont utilisées pour déterminer l'énergie de liaison et le coefficient d'absorption du nitrure d'aluminium scandium. La microscopie électronique à balayage (MEB) est utilisée pour déterminer la rugosité des échantillons et analyser la morphologie du ScAlN. Les rayons X à dispersion d'énergie (EDS) sont utilisés pour caractériser les caractéristiques chimiques des échantillons et déterminer ses compositions en éléments.

De plus, la spectroscopie infrarouge est réalisée pour obtenir un aperçu détaillé des bandes vibrationnelles dans la structure $Sc_xAl_{1-x}N$, en fonction de x. Vu que le ScAlN est un matériau composite d'un grand intérêt, notamment dans les applications électromécaniques et optoélectroniques, ses propriétés optiques influencent la plupart des propriétés électriques et mécaniques. Pour modéliser ces propriétés, plusieurs théories telles que la méthode des éléments finis, la théorie de Rayleigh-Rice et l'approximation du milieu effectif (EMA) ont été testées. Ce travail se concentre également sur la simulation des paramètres ScAlN pour améliorer les propriétés d'une diode électroluminescente. A cet effet, le logiciel General-purpose Photovoltaic Device Model (GPVDM) est utilisé pour simuler les matériaux étudiés dans un système LED. Des efforts considérables ont été déployés pour adapter les exigences au logiciel afin d'obtenir le meilleur résultat possible avec les données expérimentales utilisées. Les résultats obtenus par cette procédure hybride étaient satisfaisants et en accord avec la littérature.

Acknowledgements

Words cannot fully express the gratitude. I hold toward the individuals who have played a pivotal role in my journey toward this degree. My heartfelt appreciation goes out to my esteemed supervisors, Professor **Bouafia Mohamed** and Professor **Krischok Stefan**, for their unwavering guidance, insightful discussions, and invaluable suggestions throughout this research endeavor. Their mentorship and encouragement have been instrumental in shaping my academic growth and fostering my passion for scientific inquiry.

I am deeply indebted to the members of my thesis jury for their insightful contributions and unwavering support. Pr. **Belkhir Nabil**'s expertise in identifying missing key points and providing clear explanations has significantly enhanced the quality of my research. Additionally, I am immensely grateful for the scientific and administrative support throughout the defense and the project as a whole. His unwavering commitment to excellence has inspired me to strive for the highest academic standards.

Professor **Bouabellou Abderrahmane'**s keen interest in the project's scientific details and his meticulous approach to scrutinizing my work have been invaluable.

I extend my deepest gratitude to Professor **Manallah Aïssa** for graciously accepting the jury position despite facing personal health challenges. His willingness to dedicate his time and attention to my work reflects his dedication to academia and his commitment to nurturing young researchers.

I would also like to express my sincere appreciation to the entire **Setif University community**, particularly the **Optics and Mechanics Institute**, for creating a stimulating and supportive environment for research. My gratitude extends to **ZMN** and the **Faraday Bau** Department of Physics, for their extensive support services, ranging from technical assistance to valuable administrative guidance.

I read in a book that if you want to be successful find a mentor, I have had the opportunity to have Dr. **Rüdiger Schmidt-Grund** as my scientific mentor; I cannot put into words how grateful I am for his help and guidance.

I wish to express my thanks to all my colleagues from Technische Physik 1 and Postgraduate School in **zentrum Für Micro and Nano** in **Technishce Universität Ilmenau** for their hospitality and support throughout my stay in Germany.

Particular thanks to M.Sc. **Rebecca Petrich** for her Co-Operation, time management, and scientific discussions ranging from sample preparations measurement organizing, results interpretation, and connecting with other people from the community.

I thank MSc. **Hauke Lars Honig** for the support in XRD analysis. I would like to further thank MSc. **Kai Daniel Hanke** for his help with XRD machine problems fixing.

A thank you is to Ms. **Noor el Ain Zahra** for formatting this dissertation and for the occasional scientific help seeing my work from the perspective of a scientist outside of the same discipline.

I would like to thank **my Family**, who have supported me mentally and psychologically all my life.

Without the collective support of these individuals and institutions, the completion of this thesis would not have been possible. Their unwavering belief in my potential has fueled my determination to pursue further academic endeavors and contribute meaningfully to the field of research.

Last but not least I have to acknowledge the **German Academic Exchange Service DAAD** for funding my research stay in Tu-Ilmenau for two consecutive years under the program Research Grants: Bi-nationally supervisor doctoral degree, 2021/2022 Funding program number:57552338.

Abbreviations

FCC	Face Centred Cubic
STM	Scanning tunnelling microscope.
Mo	Molybdenum
Pt	Platinum
Ti	Titanium
Ar	Argon
InAs	Indium Arsenide
GaAs	Gallium Arsenide
InP	Indium Phosphide
Si	Silicon
NaCl	Sodium Chloride
MgO	Magnesium Oxide
GaN	Gallium Nitride
AlN	Aluminum Nitride
InN	Indium Nitride
ScAlN	Scandium Aluminum Nitride
LED	Light Emission Diode
HCP	Hexagonal Close Packed
Eg	Band Gap Energy
MOCVD	Metal–Organic Chemical Vapor Deposition
MOVPE	Metal–Organic Vapor Phase Epitaxy
HVPE	Hydride Vapour Phase Epitaxy

IR	InfraRed
MEMS	Microelectromechanical systems
RE-Doped	Rare Earth Doped
CBM	Conduction Band Minimum
VBM	Valence band maximum
PMUT	Piezoelectric Micro-Machined Ultrasonic Transducers
MOEMS	Micro-Opto-Electro-Mechanical Systems
DLP	Digital Light Processor
DMD	Digital Micro Mirror Device
XPS	X-ray Photoemission spectroscopy
UV-Vis	Ultraviolet-Visible Spectroscopy
SE	Spectroscopic Ellipsometry
DC	Direct Current
RF	Radio Frequency
XRD	X-Ray Diffraction
RC	Rocking Curve
FWHM	Full Width at Half Maximum
SEM	Scanning Electron Microscopy
FE-SEM	Field Emitter Scanning Electron Microscopy
EDX	Energy Dispersive X-Day Spectroscopy
MSE	Mean Square Error
EMA	Effective Medium Approximation
FTIR	Fourier Transform InfraRed Spectroscopy

DF	Dielectric Function
ESCA	Electron Spectroscopy Chemical Analysis
PDF	Powder Diffraction File
AFM	Atomic Force Microscope
VASE	Variable Angle Spectroscopic Ellipsometry
FEM	Finite element method
LO	Longitudinal Optical
RRT	Rayleigh-Rice theory
GPVDM	General-Purpose Device Model
MBE	Molecular Beam Epitaxy
RMS	Root Mean Square
MGT	Maxwell-Garnett Theory

Table of Contents

Abstract……………………………………………………………………………….…i

Acknowledgements……………………..……………………………………….…… ii

Abbreviations………………………………………………………..…………. iv

I. General Introduction 1

A/ THEORETICAL PART

II. Materials Study ....

II.1 Introduction 5

II.2 Crystal structure and basic properties of wide bandgap SC 5

II.3 Group III-nitrides 9

II.3.1 Crystal structure 9

II.3.2 Properties of Group III-nitrides 11

II.4 Aluminum Nitride 14

II.4.1 Crystal structure 15

II.4.2 Application of aluminum nitride 15

II.5 Rare earth elements 17

II.5.1 Rare earth applications 21

II.6 Scandium Aluminum nitride alloys 22

II.7 LEDs and MEMS Technology 26

III. Description of characterization techniques 30

III.1 Introduction 31

III.1.1 X-Ray Diffraction (XRD) 31

III.1.2 Scanning Electron Microscopy SEM 32
III.1.3 Energy Dispersive X-Ray EDX 33
III.1.4 Ellipsometry Spectroscopy 34
III.1.5 Ultraviolet-Visible (UV-Vis) Spectroscopy 35
III.1.6 X-Ray Photoemission Spectroscopy (XPS) 36
III.1.7 Fourier Transform Infrared Spectroscopy (FTIR) 37

B/ EXPERIMENTAL AND SIMULATION PART

IV. Material Preparation And Analysis 39

IV.1 Introduction 40

IV.2 Characterization of ScAlN Samples 40

IV.2.1 First Group 41
IV.2.1.1 Co-Sputtering 42
IV.2.1.2 Spectroscopic Characterization Techniques of the First Group 43
IV.2.1.2.1 X-Ray Diffraction (XRD) 43
IV.2.1.2.2 Scanning Electron Microscopy SEM 46
IV.2.1.2.3 Energy Dispersive X-Ray EDX 48
IV.2.1.2.4 Ellipsometry Spectroscopy 52
IV.2.2 Second Group 55
IV.2.2.1 Spectroscopic Characterization Techniques of the Second Group 56
IV.2.2.1.1 Ultraviolet-Visible (UV-Vis) Spectroscopy 56
IV.2.2.1.2 X-Ray Photoemission Spectroscopy (XPS) 60
IV.2.2.1.3 Spectroscopic Ellipsometry 63
IV.2.2.1.4 X-Ray Diffraction (XRD) 67
IV.2.3 Third Group 69
IV.2.3.1 Spectroscopic Characterization Techniques of the Third Group 71
IV.2.3.1.1 Spectroscopic Ellipsometry 71
IV.2.3.2 Effective Medium Theory (EMT) 73
IV.2.3.2.1 Introduction 73
IV.2.3.2.2 Implementation of EMA in Determination of ScAlN Dielectric Function 75

IV.2.4 Fourth Group ... 78

IV.2.4.1 Spectroscopic Characterization Techniques of the Fourth Group ... 80

IV.2.4.1.1 Fourier Transform Infrared Spectroscopy (FTIR) ... 80

IV.3 Conclusion ... 83

V. SIMULATING LEDS BASED ON SCALN ... 84

V.1 Introduction ... 85

V.2 Software General-Purpose Device Model-GPVDM Description ... 85

V.3 Optical Properties ... 87

V.3.1 The Dielectric Constant ε(ω) ... 87

V.3.2 Refractive Index n (ω) ... 91

V.3.3 Extinction Coefficient K(ω) ... 92

V.3.4 Reflectivity R (ω) ... 93

V.4 Piezoelectric properties ... 94

V.4.1 The Piezoelectric Effect ... 94

V.4.2 Electrical Properties of a Piezoelectric Material ... 94

V.5 Modelling Theories of Optical Properties ... 96

V.5.1 Finite Element Method (FEM) ... 97

V.5.2 Maxwell's Equations ... 98

V.5.2.1 Maxwell's Equations in the Time Regime ... 98

V.5.2.2 Maxwell's Equations in the Harmonic Regime ... 99

V.5.3 Meshing ... 100

V.5.4 Grid-Based Meshing Method (Quadtree2D/Octree3d Methods) ... 102

V.5.5 Frontal Method or Frontal Advancement ... 102

V.5.6 Meshing Method Based on Delaunay Triangulation ... 104

V.6 Rayleigh-Rice Theory (RRT) and Effective Media Approximation (EMA) ... 105

V.6.1 Rayleigh-Rice Theory (RRT) ... 105

V.6.1.1 The Effective Media Approximation (EMA) ... 106

V.7 Simulation of the Optoelectronic Device (LED) ... 106

V.8 Results and Discussion 109

VI. GENERAL CONCLUSION 116

VII. REFERENCES.. 121

List of Tables

Table II.1: Structural, electrical, thermal, and optical characteristics of wurtzite AlN, GaN, and InN.

Table II.2: The electronic configurations of lanthanides in metallic and ionic forms.

Table IV.1: Comparison of ScAlN deviations measured at 6KV.

Table IV.2: Scandium content and ScAlN thickness.

Table IV.3: Photon energy of $Sc_xAl_{1-x}N$ samples.

Table IV.4: The elements existing in the sample and their relative atomic concentration.

Table IV.5: Layer thicknesses and Cauchy parameters of $Sc_xAl_{1-x}N$ layer.

Table IV.6: Layer thicknesses and concentrations of Scandium in ScAlN samples.

Table IV.7: Scandium and aluminum content in the ScAlN (scandium aluminum nitride) samples.

Table IV.8: Comparison of the peak positions k of the vibrational modes E_2^{high} and A_1 (LO) from Infrared Spectroscopy in [1/cm].

Table V.1: Piezoelectric coefficients of III-Nitrides alloys

Table V.2: Results for the different concentrations

List of Figures

Figure II.1: Crystal structure, (a) the FCC unit cell (111), (010) plans. (b) the zinc blend crystal structure, (c) Crystal structures can be observed directly with a scanning tunneling microscopy (STM) image of an InAs (111), (d) The simple hexagonal unit cell spanned by a1, a2 and

Figure II.2: Scheme of optical transition in semiconductor with a (a) direct bandgap and (b) indirect bandgap.

Figure II.3: The unit cells of (a) the diamond cubic crystal structure, (b) the hexagonal diamond, (c) the zincblende, and (d) the wurtzite.

Figure II.4: The AlN Wurtzite and zinc blende structure.

Figure II.5: The 15 lanthanides of the periodic table.

Figure II.6: Bandgap values for wurtzite and zincblende structure of InN, GaN and AlN and their alloys as a function in the lattice constant.

Figure II.7: Hexagonal scandium Aluminum nitride ($Sc_xAl_{1-x}N$).

Figure II.8: (a) Direct band gap diagram (b) state density of AlN.

Figure II. 9: Visualization of the scale of MEMS.

Figure II. 10: The four sectors of MEMS.

Figure II.11: MEMS Technology Diagram.

Figure II. 12: DLP Technology images, Texas Instruments.

Figure II. 13: LEDs applications.

Figure III.1: Principle of X-Ray Diffraction analysis.

Figure III.2: Principle of SEM.

Figure III.3: Principal of EDX.

Figure III.4: Schematic diagram of the geometry of an ellipsometry measurement.

Figure III.5: Schematic diagram of the XPS technique.

Figure III.6: A schematic of the interferometer used in a Fourier Transform Infrared Spectrometer.

Figure IV.1: The samples of the First group.

Figure IV.2: Co-sputtering machine.

Figure IV.3: Schematic of a typical sputtering system in either the DC or the RF Configuration.

Figure IV.4: (a) AlN sputtered at Room temperature.(b) AlN sputtered at 300°C.

Figure IV.5: (a) XRD scan rocking curves of ScAlN sample, (b) XRD scan rocking curves of $Sc_{35}Al_{65}N$ sample.

Figure IV.6: Changes in FWHM as a function of Scandium percentage.

Figure IV.7: Scanning electron micrograph of ScAlN.

Figure IV.8: Sample chemical composition indication the scandium percentage present in the samples verses the expected values at 6KV.

Figure IV.9: Sample chemical composition indication the scandium percentage present in the samples verses the expected values at different voltages.

Figure IV.10: Wafer geometry and line scan positions.

Figure IV.11: Experimental and generated data of sample SC%=25.

Figure IV.12: Dielectric Function by SE of different Sc percentages.

Figure IV.13: Cary 5000 UV-Vis spectroscopy with software.

Figure IV.14: Reflectance spectra of the scandium aluminum nitride.

Figure IV.15: a, b, c, d, e, f showing band gap for ScAlN with 6%, 12%, 24% and 36% of scandium, respectively.

Figure IV.16: Ultra-high vacuum system with an attached XPS system.

Figure IV.17: XPS overview spectrum of $Sc_{0.36}Al_{0.64}N$ after 20 minutes of sputtering.

Figure IV.18: a, b, c is magnified picture of curves describing (Sc and N, Al, O).

Figure IV.19: Spectroscopic ellipsometry.

Figure IV.20: The relation between refractive index, wavelength, and scandium content.

Figure IV.21: Absorption coefficient of ScAlN.

Figure IV.22: X-Ray Diffraction machine.

Figure IV.23: The X-ray diffractograms of the ScAlN thin films.

Figure IV.24: Lattice constant of ScAlN.

Figure IV.25: The samples of the third group.

Figure IV.26: Spectral magnitude (Ψ) and phase (Δ) measured by ellipsometry at 75°, 70°, 65° on different samples.

Figure IV.27: Air /thin film/substrate multiple wave interference.

Figure IV.28: a, b, c, d is Epsilon effective, Maxwell and experimental results vs photon energy of scandium aluminum nitride with scandium ratio of 0%, 1.6%, 14.4% and 25.1% respectively.

Figure IV.29: Experimental results of all samples 0% to 25.1% scandium vs photon energy.

Figure IV.30: (a) ScAlN in transparent box, (b) ScAlN samples on the substrate holder, (c) the components of the sample ScAlN.

Figure IV.31: Bio-Rad FTS 3000 spectrometer.

Figure IV.32: Determination of the peak positions on the wavenumber as a function of the scandium content x in $Sc_xAl_{1-x}N$.

Figure IV.33: Graphical representation of the values in the Table III.8 for comparing the phonon positions of E_2^{high} and A_1 (LO).

Figure V. 1: Representation of the epsilon evaluation of Sc-AlN as a function of the gap energy for different percentage of scandium Sc = 0% 1.6% 14.4% and 25.1%.

Figure V. 2: Representation of the real epsilon evaluation of Sc-AlN as a function of the gap energy for different percentage of scandium Sc = 0% 2% 14% and 25.1%.

Figure V. 3: Representation of the imaginary epsilon evaluation of Sc-AlN as a function of the gap energy for different percentage of scandium Sc = 0% 2% 14% and 25.1%.

Figure V.4: The evaluation of the refractive index of Sc-AlN as a function of the gap energy for different percentage of scandium Sc = 0% 2% 14% and 25.1%.

Figure V. 5: The evaluation of the extinction coefficient of Sc-AlN as a function of the gap energy for different percentage of scandium Sc = 0% 2% 14% and 25.1%.

Figure V.7: Distribution of crystalline classes and their electrical owners.

Figure V. 8: Chronologies on the development of different simulation models and their numerical modeling methods for optoelectronic devices.

Figure V. 9: Some types of mesh elements.

Figure V. 10: Illustration of a grid (a 2D example).

Figure V.11: Illustration of the edge advancement method.

Figure V.12: Delaunay triangulation and any triangulation.

Figure V.13: Welcome window of GPVDM.

Figure V.14: Choice of the optoelectronic device for the simulation.

Figure V.15: Introduction of the optical parameters.

Figure V.16: The layer editor and the material types.

Figure V.17: The emitted light of a Sc-AlN based LED.

Figure V.18: Photon density for x=0%.

Figure V.19: The 2D photon distribution for x=0%.

Figure V.20: 3D distribution of the photon density for x=0%.

I. General introduction

Nanotechnology is an interdisciplinary field of science that deals with controlling, designing, and synthesizing materials at the atomic and molecular levels. In particular, it involves constructing nanoscale devices and features. The process of nanotechnology requires the controlled addition of atoms to create nanostructures with at least one dimension smaller than 40 nanometers. The "bottom-up" approach, which is a fundamental aspect of nanotechnology, involves building structures from the ground up, while the "top-down" approach involves the removal of material from a larger piece of material. The "bottom-up" approach is the primary method used in industry [1]. Nanoscale materials exhibit unique properties that arise from their reduced dimensions, such as increased surface area, quantum confinement effects, and changes in electronic structure. For example, previously inert metals become highly catalytically active when their dimensions are reduced to the nanoscale [2, 3]. Additionally, materials with an indirect band gap in bulk can become direct band gap materials, while magnetic materials can undergo a phase transition from ferromagnetic to superparamagnetic[4,5]. Furthermore, quantum confinement effects appear, bringing new opportunities and obstacles. Spectroscopy is an essential tool in the study of semiconductors, providing crucial insights into the characteristics of matter. Semiconductor nanostructures, such as carbon nanotubes, nanoribbons, nanowires, and quantum dots, have unique electrical and optical properties that are vital for their applications in modern electronic gadgets [6, 7]. The electrical conductivity of semiconductors lies between that of conductors and insulators, and it is easily adjustable across a broad range. The band structure of semiconductors arises from the periodic potential of a semiconductor crystal, and it manifests itself in the energy band structure of electrons in the crystal. A band gap is a range of energy levels in which no electron states are allowed in a semiconductor. The states below the gap are entirely filled by electrons, while the states above the gap are unoccupied [8]. At absolute zero, filled or empty bands do not transmit net current, rendering these materials insulators. Scandium is a rare earth metal with a fascinating history. It was discovered in 1878 by Swedish chemist Lars Fredrik Nelson through spectroscopic analysis of minerals. Scandium is present in all rare earth minerals, although only in trace amounts. Scandium iodide is used to create a

highly efficient light source similar to sunlight in mercury vapor lamps, which are used for filming indoors or at night. Scandium aluminum alloy is utilized in high-end bicycle frames, baseball bats, and Russian MIG fighter planes due to its unique properties. The objective of this work is to characterize the optical, electronic, and structural properties of scandium aluminum nitride in $Sc_xAl_{1-x}N$ thin film, prepared by co-sputtering. The manuscript consists of three chapters and a general conclusion. The first chapter introduces the field of nanotechnology and the unique properties of nanoscale materials, including quantum confinement effects, band gaps, and melting points. The second chapter discusses the use of spectroscopy in the study of semiconductors, including their electrical and optical characteristics, band structure, and conductivity. The third chapter provides a detailed discussion of scandium, including its discovery, properties, and applications, such as Scandium iodide and Scandium aluminum alloy. The conclusion summarizes the findings and provides an outlook for future research in this field, such as the potential use of scandium in catalysis and electronics.

A/ Theoretical Part

II. Material Study

II.1 Introduction

In this chapter, we will present the crystal structure of wide bandgap Semiconductor of III group Nitride and aluminum nitride, its physical properties and its applications. In addition, we will talk about properties and applications of scandium, since we are going to study an alloy material $Sc_xAl_{1-x}N$ it is necessary to talk a little bit about it.

II.2 Crystal structure and basic properties of wide bandgap SC

A crystal is a substance that has long-range organization. Diamonds and rock salt are well-known examples of crystals, but most metals also have a crystalline structure. This contrasts with amorphous materials such as polymers, which lack long-range organization. Depending on their energy band structure, crystals can be insulators, semiconductors, or metals [8].

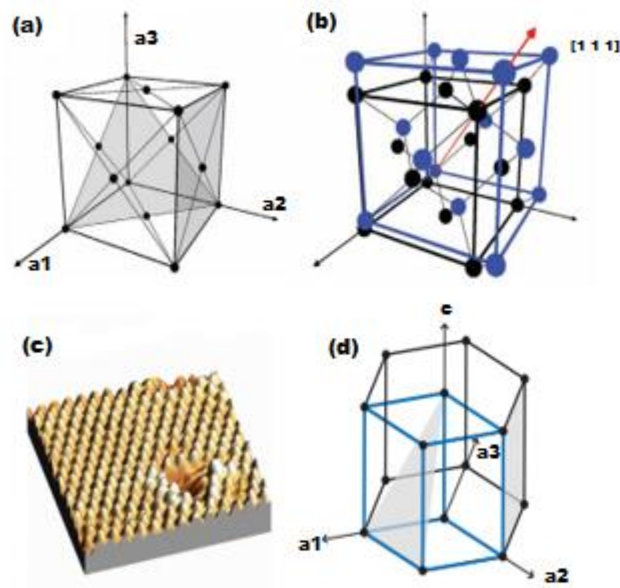

Figure 0I.1: Crystal structure, (a) the FCC unit cell (111), (010) plans. (b) the zinc blend crystal structure, (c) Crystal structures can be observed directly with a scanning

tunnelling microscopy (STM) image of an InAs (111), (d) The simple hexagonal unit cell spanned by a1, a2 and c [8]

III-V semiconductors are compound materials made up of elements from periodic system groups III and V, such as GaAs and InP (Figure 0I.1). These are costlier than Si, and the material's degree of perfection is lower. These materials, on the other hand, have utility that Si does not. The most significant distinction is that most of them have a so-called direct band gap, which means that electrons may relax to lower energy states (recombine with holes) with conserved momentum while emitting light (photons). Thus, III-Vs are used in light-emitting devices like LEDs and lasers. [6]

A direct bandgap in semiconductor physics indicates that the minimum of the conduction band is immediately above the maximum of the valence band in the k space. An indirect semiconductor, on the other hand, is one that has a bandgap in which the minimum energy in the conduction band is displaced by a k vector relative to the top of the valence band. Because photons have little momentum, optical transitions in which both the beginning and final states are band states are permitted only if the crystal momentum is preserved. Vertical transitions are processes represented by vertical lines in the $E(k)$ diagram. Momentum must be provided from other sources, such as impurities and phonons, for non-vertical transitions to occur. Indirect transitions are those that involve a photon state and a phonon or impurity state. Inter-band transitions from the top of the valence band to a conduction band valley at or near the zone border are two key instances of indirect radiative transitions, as are intra-valley transitions responsible for free-carrier absorption. The optical transition (emission) processes in semiconductors with a direct bandgap and an indirect bandgap are depicted in Figure 0I.2. Theoretical foundations for indirect optical transitions may be found in, for example [9], but working scope here was confined to defining the rate of phonon-assisted optical transitions.

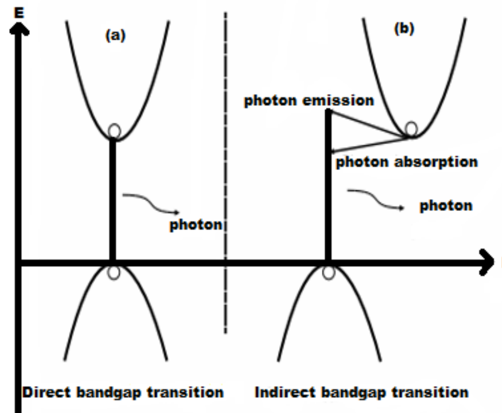

Figure 0I.2: Scheme of optical transition in semiconductor with a (a) direct bandgap and (b) indirect bandgap [9]

Covalent connections bind the Group III atoms tetrahedrally to the nitrogen atoms. Group III-nitrides such as (Ga, Al, In) N exist in two crystalline structures:

1. Hexagonal Structures: Hexagonal structures, also known as Wurtzite, exhibit hexagonal symmetry, with the unit cell having the form of a rhombus.
2. Cubic crystal structure: The cubic crystal structure contains a unit cell in the shape of a cube and comes in three varieties:
   2.1. Primitive cubic, which has one atom in each of the unit cell's four corners.
   2.2. Body-centered cubic, which is like the primitive cubic but has an atom in the center of the unit cell.
   2.3. Face-centered cubic (FCC), which is like the primitive cubic but contains atoms at the center of the unit cell's faces. The FCC lattice is one of two close-packed lattices that reach the maximum packing density. The other is the hexagonal close-packed lattice (HCP).

The most fundamental distinction between them is in the order in which their atomic layers are stacked. Assume, for example, that the model of tight packing of spheres corresponds to atoms. If the first reference layer is labelled as "A," the next layer of spheres on top ("B") can be set in place. The most fundamental distinction between them is in the order in which their atomic layers are stacked. Assume, for example, that the model of tight packing of spheres corresponds to atoms. If we label the first reference layer as "A", the layer of spheres on top ("B") can be placed in the spaces between three contacting spheres from the A-layer below. The spheres can be positioned in the gaps between the three contacting spheres from the B-layer below. The main difference between FCC and HCP arises from the packing of the third layer, as the spheres can be arranged in two different ways:

* First, the spheres of the third layer are arranged in such a manner that they are not directly above the A-layer, in which case the layer is referred to as a C-layer to reflect this distinct location. This yields a stacking sequence of ABCABC..., which corresponds to the FCC lattice.
*Secondary, in such a way that the spheres of the third layer are exactly above the A-layer, in which case the layer is an A-layer once more. The result is an ABABAB stacking sequence... and is equivalent to the HCP lattice.

The diamond cubic crystal structure is based on the FCC lattice and is a mixture of two interpenetrating FCC sub-lattices separated by 14 the length of the diagonal of the cubic cell. Figure II.3a depicts the unit cell of the diamond cubic crystal structure. When all the lattice sites are filled by the same type of atom, the name diamond cubic is used. If, on the other hand, each sub-lattice is filled by a different type of atom, we get the zincblende structure (Figure. II.3c), which is the configuration in which most III-V crystallize [10].

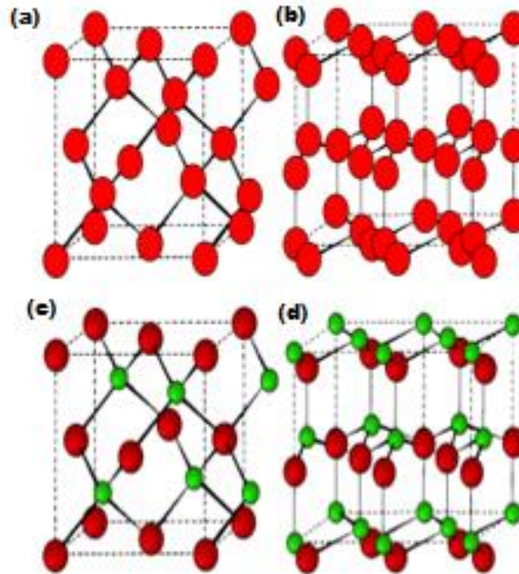

Figure I0.3: The unit cells of (a) the diamond cubic crystal structure, (b) the hexagonal diamond, (c) the zincblende, and (d) the wurtzite [10]

On the one hand, (a) and (c) have the same structure as (b) and (d), but in (a) and (b), the lattice points are filled by the same kind of atoms, but in (c) and (d), each sub-lattice is inhabited by a different type of atom. As a result, several names are employed to describe them. The Bravais lattice and the base are combined in such a way that two atoms with a certain distance and angle between them occupy each point of the Bravais lattice. [11].

II.3 Group III-nitrides

II.3.1 Crystal structure

Group III nitrides are an outstanding material system. This materials system has enabled deep ultraviolet (300 nm or photon energy > 4.1 eV based on high Al content $Al_xGa_{1-x}N$ quantum wells [QWs]), ultraviolet (400 nm or photon energy > 3.1 eV based on $In_yGa_{1-y}N$ QWs), ultraviolet (400 nm or photon energy = 2.7 eV based on $In_yGa_{1-y}N$ QWs), blue (455 n (LDs).

This spectrum of direct bandgaps is not available in any other materials system. There were no effective ultraviolet or blue LEDs prior to the introduction of nitrides as optoelectronic materials, and green LEDs based on II-VI materials had low lifetimes due to the ease of dislocation production in the active areas of the II–VIs.

This spectrum of direct bandgaps is not available in any other materials system. There were no effective ultraviolet or blue LEDs prior to the introduction of nitrides as optoelectronic materials, and green LEDs based on II-VI materials had low lifetimes due to the ease of dislocation production in the active areas of the II–VIs. Compared to classical materials like GaAs, which have dislocation densities of 10^4 cm^{-2}, Group III nitride-based devices perform well with densities of over 10^8 cm–2. However, if the dislocation density exceeds 10^{10} cm^{-2}, the performance deteriorates, which has led to efforts to promote the use of bulk GaN wafer, as discussed in Fujito et al. However, when the nitrides are very resistant to oxidation (and etching), they are mechanically rigid and exhibit no signs of protracted defect motion at ordinary operating temperatures. GaN-based LEDs are widely used in colored illumination applications, such as green traffic lights. White light is generated when blue LEDs are paired with a yellow-emitting phosphor; consequently, GaN has been the material that permitted the field of solid-state lighting. Violet GaN-based LEDs with a 405 nm wavelength are already widely used in high-definition optical data storage [12].

AlN, GaN, and InN of the binary group III-nitrides can crystallize in three structural phases: (a) wurtzite, (b) zincblende, and (c) rock-salt (NaCl). At ambient temperatures, however, the wurtzite structure is the thermodynamically stable phase [13-14]. The zincblende structure is metastable and may be stabilized by heteroepitaxial thin film growth on cubic structure (001) crystal planes such as Si, MgO, and GaAs [15]. At high pressure, a phase change to the rock-salt structure occurs [15]. In many ways, the structures of wurtzite and zincblende are comparable. The group III element is surrounded in both cases by four atoms of the group V element, which are placed at the corners of a tetrahedron. Similarly, the group V element is surrounded by four group III atoms. In

addition, in both constructions, the twelve next-closest neighbors are the same distance apart. The fundamental variation between the structures of wurtzite and zincblende is seen exclusively in the third nearest neighbors, indicating that they have distinct stacking sequences. The stacking sequence of the wurtzite structure along [0001] is ABAB, whereas the stacking sequence of the zincblende structure along [001] is ABCABC, where A, B, and C correspond to permitted locations of the III-N pairings of the closed-packed layers. A flaw in the stacking process might cause one structure to be transformed into another or generate a structural defect. At high pressures, the wurtzite structure can be converted into the rock-salt structure. The bond nature changes primarily from covalent to ionic and from four to six-fold coordination of atoms throughout this metamorphosis. Experimentally, the structural phase change was seen at pressures of 22.9 GPa, 52.2 GPa, and 12.1 GPa for AlN, GaN, and InN, respectively [16-17].

II.3.2 Properties of Group III-nitrides

III-nitride semiconductors and their alloys are direct band gap semiconductors, as previously stated. A semiconductor's band gap energy is a critical characteristic that influences its transport and optical properties, as well as a variety of other phenomena. The main technical benefit of the III-nitride system is that the band gap can be controlled by alloying GaN with InN and/or AlN, allowing it to span a wide spectral range from deep UV (AlN = 6.2 eV) to near IR (InN = 0.7 eV). Therefore, depending on the mix of In or Ga or Al in the alloy system, ternary, and quaternary alloy systems of AlN, GaN, and InN (such as InGaN, InAlN, AlGaN, and AlGaInN) can have continuous band gap energies ranging from 0.7 eV to 6.2 eV. The high polarization of III-nitrides is a distinguishing feature [18, 19]. The wurtzite structure of the III-nitride materials exhibits spontaneous polarization along the c-axis due to the lack of a center of symmetry and the high ionicity of the metal-nitrogen bonds. Additionally, the application of an external strain to this structure results in piezoelectric polarization. As a result, the net polarization is made up of two parts:

(1) Spontaneous polarization, which is inherent in the material, and (2) strain-induced piezoelectricity, both of which are impacted by the polarity of the III-nitrides. The optical and electrical characteristics of wurtzite III-nitrides are influenced by spontaneous and piezoelectric polarizations. III-nitrides have extremely strong chemical bonds. III-nitride semiconductors have a high melting point, mechanical strength, and chemical stability due to this strong chemical bonding. Furthermore, their strong bonding renders them resistant to the high-current electrical deterioration and radiation damage seen in the active portions of light-emitting devices [20]. These materials are also thermally conductive. Devices based on III- nitride can work at elevated temperatures as well as in harsh conditions. The electrical characteristics, notably carrier concentration and mobility, determine the performance and efficiency of III-nitride-based electronic devices. Using Hall measurements, a range of electron mobility and background concentration values for AlN, GaN, and InN have been determined. Carrier mobility is affected by several parameters, including temperature, electric field, doping concentration, and semiconductor material quality. The value of carrier mobility is low when the lattice mismatch is considerable. Using a buffer layer during nucleation minimizes strain and increases carrier mobility. The optical characteristics of III-nitride-based devices are determined by critical parameters such as the materials' refractive index and dielectric constant. Table II.1 [13] lists some of the most important structural, electrical, thermal, and optical characteristics of wurtzite AlN, GaN, and InN.

Property	**AlN**	**GaN**	**InN**
Thermal expansion coefficient (300K)			
a (x10^{-6} K^{-1})	4.2	5.59	5.7

c ($x10^{-6}$ K^{-1})	5.3	3.17	3.7
Thermal conductivity ($Wcm^{-1}K^{-1}$)	2.0	1.3	0.8
Melting point(°C)	>3000	>2500	>1100
Bulk Modulus (GPa) (300K°	210	210±10	140
Refractive index	2.2	2.35	2.56
Bond Length(Å)	1.89	1.94	2.15
Cohesive energy per bond (eV)	2.88	2.24	1.93
Lattice constant (Å)	$^{a}3.11$, $^{c}4.97$	$^{a}3.18$, $^{c}5.18$	$^{a}3.54$, $^{c}5.70$
Energy gap (eV)	6.2	3.39	0.7
Effective electron mass (m)	0.48	0.2	0.06
Electron mobility ($cm^2V^{-1}s^{-6)}$	300 Theo	1000 Theo	14000 Theo
	426 Expt	900 Expt	3980 Expt
Peak drift velocity ($x10^7$ cms^{-1})	0.02	3.1	4.3
Electron concentration (cm^{-3})	$<10^{16}$	$\sim10^{17}$	$>10^{19}$
Dielectric constant	ε_0=8.5±0.2	ε_0=10.0	ε_0=15.3
	ε_∞=4.68- 4.84	ε_∞=5.5	ε_∞=8.4

Table 0I.1: Structural, electrical, thermal, and optical characteristics of wurtzite AlN, GaN, and InN.

Although most III-Nitride semiconductors, particularly those for industrial-scale manufacturing, are typically produced using metal–organic chemical vapor deposition (MOCVD), metal–organic vapor phase epitaxy (MOVPE), and HVPE, these processes have significant limitations. These manufacturing processes are distinguished by relatively high growth temperatures (>900°C). As a result, when the sample is cooled to room temperature from such elevated temperatures, it is subjected to a significant amount of stress. Furthermore, due to the dissociation of InN at such elevated temperatures, the inevitability of such elevated temperatures has hampered the creation of high-quality InN and related alloys, which are prospective candidates for IR and terahertz (THz) optoelectronic applications [21]. All these procedures, however, entail the treatment and use of toxic precursors as by-products, making these approaches less environmentally friendly and dangerous to human health, which has become a serious problem at the global level [22].

II.4 Aluminum Nitride

Aluminum Nitride AlN is a semiconductor with a large band gap (6.2 eV). It is a high thermal conductivity electrical insulator. AlN is also a refractory material with good oxidation [23-24] and abrasion resistance. It can be used as an optoelectronic substrate in the ultraviolet sector and in electronics for the fabrication of microwave power transistors. There is now a lot of research being done to create UV emission diodes out of gallium aluminum nitride. Experiments have allowed for wavelengths in the order of 210 nm [25], and the gap of the aluminum nitride would theoretically enable emissions up to 200 nm. However, further study will be required before such electronic substances may be sold on the market.

II.4.1 Crystal structure

Wurtzite (hexagonal) and Zinc Blende (cubic) are the two polytype crystal formations of AlN. (Figure. II.4). The Wurtzite structure is made up of two hexagonal sublattices of nitrogen and aluminum atoms offset by a vector of 0.3869 degrees (0, 0, 1). The Zinc Blende is made up of two face-centered cubic sublattices of nitrogen and aluminum atoms displaced by one-quarter of a vector (1,1,1). The hexagonal phase is the most thermodynamically stable configuration [26]. The Al-N phase diagram reveals that there is only one solid AlN compound, i.e., one without a solid solution domain. This compound can exist in two crystal forms, hexagonal or face-centered cubic, depending on the processing circumstances.

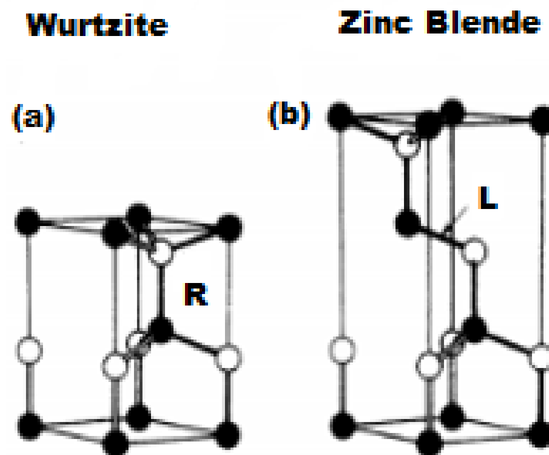

Figure 0I.4: The AlN Wurtzite and zinc blende structure [26]

According to the SiC polytype nomenclature, the AlN Wurtzite structure (space groupP63mc) is of type 2H (Figure II.4a and Figure II.4b). The equivalent lattice parameters are area c= 3.11A and c = 4.98A [27].

II.4.2 Application of aluminum nitride

AlN thin films may be produced using a variety of growing processes. Researchers from all around the world have used a variety of methodologies to investigate the various

development mechanisms and their relationship to the functional features of AlN. The most often used technologies, for example, are pulsed laser deposition (PLD) [28-29], chemical vapor deposition (CVD) [30], and physical vapor deposition (PVD) [31]. Reactive magnetron sputtering (RMS) has gained popularity in the PVD industry, notably in the industrial sector, because to its low cost, simplicity, large-scale production application, and the excellent quality of coatings that can be obtained at low temperatures [32].

Many uses are possible because of AlN's physical, chemical, mechanical, and optical capabilities. For example, AlN has outstanding acoustic qualities due to its high piezoelectric coefficients, particularly d33, which give an opportunity to improve the performance of MEMS devices. Furthermore, the broad optical bandgap of AlN of 6.2 eV allows for the emission of a deep UV wavelength of about 200 nm for opto-electronic applications. Indeed, an AlN LED with a 210 nm emission wavelength has already been described [26]. Furthermore, the high thermal conductivity of AlN, which is about 300 and 130 W/mK [47] in bulk and thin film, is significant in high temperature working devices. Manipulation of the optical characteristics of this optically transparent material also poses a significant challenge for future applications, particularly in optical quantum circuits. For this reason, three functional qualities are most important. First, the AlN thin film's c-axis out of plane orientation is required to take advantage of its highest second order nonlinearity for wavelength conversion and electro-optical effects. Second, the high ordinary refractive index of AlN deposited on Si wafer (usually 2.1) is required for minimal loss in silicon integrated AlN photonic circuits [33]. This high refractive index allows for substantial light confinement over extended distances, resulting in the appearance of a non-linear optical effect on the chip scale. [34] Third, the wide range of AlN transparency (bandgap near to 6 eV) may be used to create devices with a wide operating band from UV to IR wavelengths. AlN is an ideal option for integrated nonlinear optics due to the combination of the following characteristics. AlN is an excellent host material for magnetic and optical experiments with transition and rare earth elements due

to its high transparency in the UV-visible region and dielectric characteristics. As a result, the next sections will focus on the properties of AlN alloys[35].

II.5 Rare earth elements

The word rare earth is made up of two parts. The first component, rare, refers to the difficulty of locating these elements in pure crystals or free metal phases, not to their relative abundance in the earth's crust. It is more plentiful than silver or lead. Furthermore, these compounds coexist in oxides, indicating the difficulties in separating them. This is the meaning of the second component of the term, earth, as described by the Greeks as a substance that could not be transformed further by heat [36].

Rare-earth metals are defined as the 15 lanthanides found below the main body of the periodic table and the elements Scandium and Yttrium, as seen in Figure II.5.

Figure 0I.5: The 15 lanthanides of the periodic table [37]

These lanthanide elements are distinguished by electron occupancy of the 4f level (from 0 in La to 14 in Lu). Lanthanides' interest stems from their properties, which are mostly dependent on the occupancy of the 4f level. Although the word Lanthanides refers to the 14 elements from Ce to Lu that have partially or filled 4f electrons, Scandium (Sc), Yttrium (Y), and Lanthanum (La) can all be classified as Lanthanides. They have comparable chemical and physical characteristics to the 14 lanthanides elements, despite lacking electrons at the 4f level. The analogy of their electrical arrangement of the outer shell three electrons with the lanthanides (3 d 4s) 3 for Sc, (4 d 5 s) 3 for Y, and (5d 6 s) 3 for La is the rationale for uniting these three elements. As a result, it has all the features of lanthanides that are not dependent on the 4f electrons [37]. Despite the lanthanide elements having identical underlying electrical structures, the slight changes between them result in a wide range of features, particularly in optical performance. As a result, the electrical arrangement must be studied to comprehend the essential features of lanthanides. The electronic configurations of lanthanides in metallic and ionic forms are listed in the (Table II. 2) below:

Atom		**Ln3+**	**Ln4+**	**Ln3+**
La	$[Xe]5d^1s^2$	[Xe]		
Ce	$[Xe]4f^15d^16s^2$	$[Xe]4f^1$	[Xe]	
Pr	$[Xe]4f^36s^2$	$[Xe]\ 4f^2$	$[Xe]4f^1$	
Nd	$[Xe]\ 4f^46s^2$	$[Xe]\ 4f^3$	$[Xe]4f^2$	$[Xe]\ 4f^4$
Pm	$[Xe]\ 4f^56s^2$	$[Xe]\ 4f^4$		

Sm	[Xe] $4f^{6}6s^{2}$	[Xe] $4f^{5}$		[Xe] $4f^{6}$
Eu	[Xe] $4f^{7}6s^{2}$	[Xe] $4f^{6}$		[Xe] $4f^{7}$
Gd	[Xe] $4f^{8}5d^{1}6s^{2}$	[Xe] $4f^{7}$		
Tb	[Xe] $4f^{9}6s^{2}$	[Xe] $4f^{8}$	[Xe] $4f^{7}$	
Dy	[Xe] $4f^{10}6s^{2}$	[Xe] $4f^{9}$	[Xe] $4f^{8}$	[Xe] $4f^{10}$
Ho	[Xe] $4f^{11}6s^{2}$	[Xe] $4f^{10}$		
Er	[Xe] $4f^{12}6s^{2}$	[Xe] $4f1^{1}$		
Tm	[Xe] $4f^{13}6s^{2}$	[Xe] $4f^{12}$		[Xe]$4f^{13}$
Yb	[Xe] $4f^{14}6s^{2}$	[Xe] $4f^{13}$		[Xe] $4f^{14}$
Lu	[Xe] $4f^{14}5d^{1}6s^{2}$	[Xe] $4f^{14}$		

Table II.2: The electronic configurations of lanthanides in metallic and ionic forms

RE-doped semiconductors have piqued the interest of scientific and industrial groups to incorporate RE emission into microelectronic technology. Combining the benefits of semiconductor electrical structure as well as its compatibility with chip technology with the emission capabilities of the RE will pave the way for new and widespread lighting technologies. Exploiting these properties has resulted in a wide range of applications, particularly in color displays and flat panel technologies. Because of the compatibility of silicon with silicon microelectronic fields, RE-doped silicon is the most researched system in this approach. However, silicon has substantial downsides, such as an indirect bandgap,

which leads to large undesired non-radiative processes. Furthermore, because of its low bandgap value (1.12 eV), doping with RE ions is confined to a few elements that emit in the IR region [35]. As a result, considerable research into alternative semiconductor hosts has been promoted to overcome the silicon drawbacks. The primary qualities to consider while looking for new hosts are compatibility with silicon substrates, direct bandgap (to eliminate non-radiative process), and wide bandgap value (to cover the visible light range). It was discovered that III-V semiconductor compounds efficiently provide integration compatibility with silicon microelectronic technology. [38] Among them, III-nitride compounds, particularly GaN and AlN, are of particular interest because to their direct and broad bandgap characteristics.

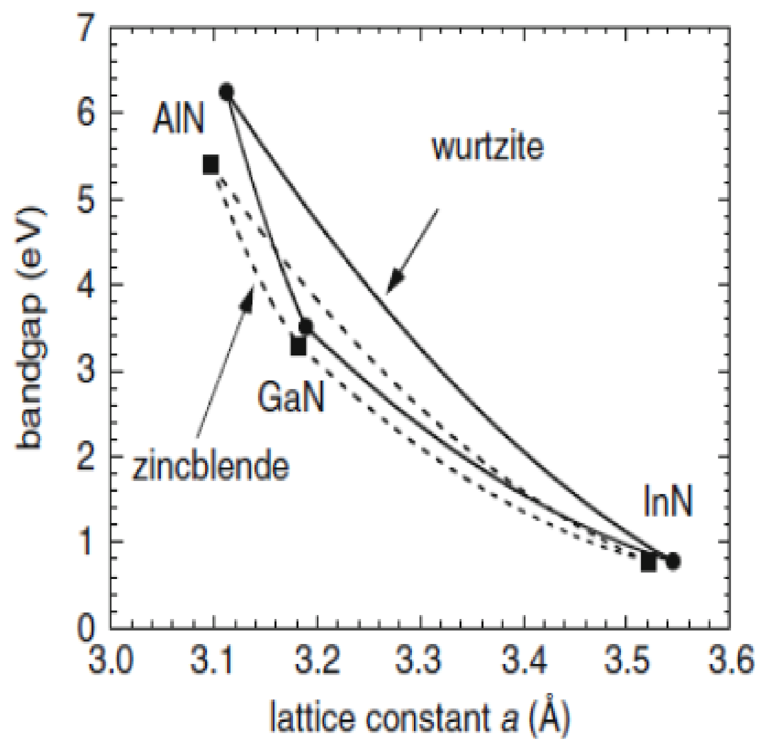

Figure 0I.6: Bandgap values for wurtzite and zincblende structure of InN, GaN and AlN and their alloys as a function in the lattice constant [38]

II.5.1 Rare earth applications

Many research groups took use of AlN's advantage to begin figuring out the behavior of RE in AlN, particularly to boost UV-Vis's light emission. As activators in AlN host materials, many rare earth elements have been employed. The majority of lanthanide element-doped AlN has been reported, and they cover the light spectrum from UV (Gd), [39] blue (Ce, Eu, Tm), [40-41] green (Tb), [42] yellow (Dy), [43] red (Sm, Eu) [43] to IR (Yb, Nd) [44-45], demonstrating the adaptability and efficiency of AlN host material. AlN has also been refined into a variety of final forms, including thin films, powders [41], and bulk ceramics. [46] Furthermore, RE-doped AlN has been reported in a variety of microstructures, including amorphous [47], polycrystalline [48], and single crystal [49]. With so many reports of employing RE-doped AlN for lighting, a thorough knowledge of the optical reaction of these RE within AlN and III-nitrides generally turned into some of the most wanted materials out there.

Understanding the excitation process of doping III-nitrides with rare earth is critical for improved interpretation of luminescence characteristics and improves our fundamental understanding of these materials. Despite a substantial portion of this study being devoted to finding and drawing a general excitation mechanism responsible for the excitation of optically active rare earth ions in semiconductors, the specific mechanism remains vague. However, we feel that the RE-doped III-nitride excitation mechanism should not be generalized. Because of the numerous means to give excitation energy to the REs ions, it may be analyzed case by case. The deep lying location of the core 4f levels in RE3+, which is protected by the outer 5s and 5p orbitals and makes the energy delivery process difficult [35], is one of the most challenging obstacles to understanding the excitation mechanism of these levels. Excitation mechanisms may be split into two groups in general: direct and indirect processes.

- Direct excitation mechanism: The pumping in this process is intended to be resonant with the difference in energy between the exited state and the ground of

the 4f levels in the RE. However, as previously stated, because these 4f levels are buried in the RE's core, the absorption cross section is extremely low. As a result, for excitation, the direct technique is inefficient. However, owing to its simplicity and developments in diode laser technology, it can be employed in some instances since it can directly pump numerous REs ions at different wavelengths at various parts of the light spectrum [50-51].

- Indirect excitation mechanism: The excitation energy could be provided via a mediator termed a sensitizer in this manner. This is a popular method of transferring energy to "activator" species that emit energy. When the activator's absorption cross section is low in a particular spectral range, for example, a sensitizer with a cross section high absorption in that range can be selected to efficiently transmit to the activator from that spectral range the intended excitation energy. The host and/or other transition metals or RE ions will function as sensitizers in RE-doped semiconductors. Due to the participation of several excitation channels, the excitation process becomes extremely difficult to comprehend in this scenario. Because the structure and optical picture in a co-doping system grow more intricate, the host lattice is employed to serve the role of photo - catalyst in the simple technique rather than integrating additional ions.

II.6 Scandium Aluminum nitride alloys

ScAlN is a piezoelectric semiconductor material with excellent dielectric properties that has largely gone untapped in terms of its applicability in microelectronics. »The fact that Scandium Aluminum is particularly well suited for power electronic components owing to its physical qualities has previously been demonstrated, « says Dr.-Ing. Michael Mikulla, project manager for Fraunhofer IAF. The project's goal is to grow lattice matched ScAlN on a GaN layer and afterwards fabricate transistors with high current carrying capacity with the resultant heterostructures. Functional semiconductor architectures based on wide bandgap materials, such as gallium nitride and scandium aluminum nitride, enable transistors with extremely high voltages and currents. These devices achieve increased

power density per chip surface, faster switching rates, and higher overall operating temperatures. This equates to lower switching losses, improved energy efficiency, and smaller systems, Mikulla [52] explains, "By mixing both semiconductors, GaN and ScAlN, we hope to double the maximum achievable power output of our systems while dramatically decreasing the energy requirement."

Combining AlN and Scandium Sc is an intriguing prospect for creating new multipurpose materials with even broader ranges of piezoelectric, mechanical, and chemical capabilities. The result will be a novel material that mixes the characteristics of Sc and AlN. Scandium nitride, in its pure state, shares several of the AlN has attractive physical qualities such as hardness and strength, as well as high temperature stability and strong electrical transport capabilities.

Sc-N is a suitable candidate for combining with AlN because of these properties. Sc-N has a poor solubility in AlN, although according to its phase diagram, numerous compounds are soluble. At 1000°C, ternary compounds Sc - Al - N can be produced. Surface alloying or reducing the crystal size are two strategies that might be used to boost this solubility. Even trace quantities of Sc absorbed into AlN should have an influence on the electrical band structure [53].

Scientists from many colleges and research organizations have joined forces to investigate scandium aluminum nitride (ScAlN). $Sc_xAl_{1-x}N$ is a novel materials system composed of an alloy of group III a (transition metal) nitrides and group III b nitrides with a stable hexagonal crystalline structure for $x < 0.55$. As opposed to gallium nitride (GaN), this novel material structure may be more suitable for future power electronics [54].

The hexagonal $Sc_xAl_{1-x}N$ ratio was projected to decrease, whereas (a) the lattice parameter was expected to rise as Sc concentration increased. Zhang et al. studied the phase stability of $Sc_xAl_{1-x}N$ and discovered that $Sc_xAl_{1-x}N$ favors the hexagonal structure up to x = 0.56, whereas Haglund et al. investigated the mixing of different $Sc_xAl_{1-x}N$ structures and discovered that $Sc_xAl_{1-x}N$ should continue to stay in the hexagonal structure up to $x \leq 0.45$ [55].

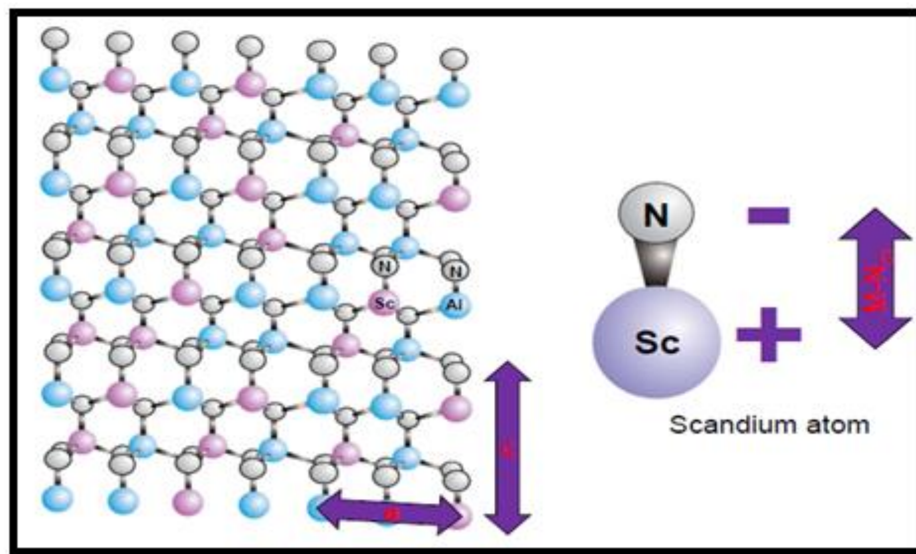

Figure 0I.7: Hexagonal Scandium Aluminum nitride ($Sc_xAl_{1-x}N$) [56]

The optical gap energy of $Sc_xAl_{1-x}N$ was anticipated to turn indirect as the Scandium ratio increased above 0.25 because the conduction band minimum (CBM) and valence band maximum (VBM) shifted towards M from, as shown in (Figure II.8), due to the Scandium 3d states influence on $Sc_xAl_{1-x}N$ CBM, which flattens the electron dispersion as the Scandium concentration increases [57].

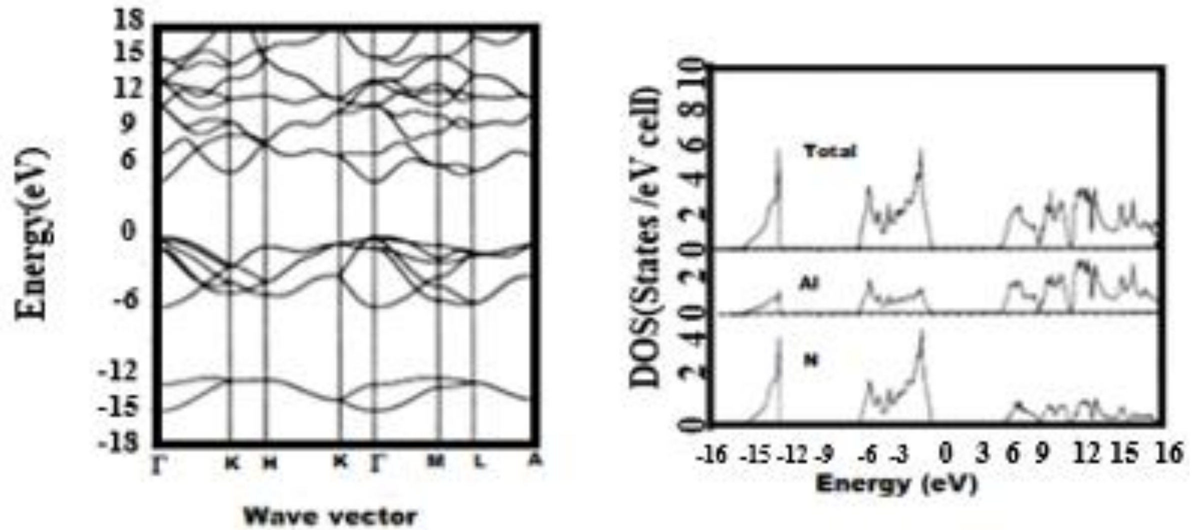

Figure 0I.8: (a) Direct band gap diagram (b) state density of AlN [58]

Scandium alters the ionic covalent bonding ratio, causing the hexagonal structure to collapse. This leads in a considerable increase in the piezoelectric response to AlN; however, if the scandium concentration exceeds 40%, the system transforms into a cubic structure and loses piezoelectricity [59].

Fabrication and characterization of piezoelectric micro-machined ultrasonic transducers (PMUT) based on scandium doped Aluminum nitride ($Sc_xAl_{1-x}N$) thin films [59]. Scandium Aluminum nitride thin layered films were formed by reactive magnetron sputtering and shaped using a reactive ion etching technique using chlorine-based chemistry at a rate of 160 nm/min [60].

This rare earth alloy (A_xB_{1-x} C) is made up of AC molecules with a molar percentage of x and BC molecules with a fraction of x. (1-x). As a result, the physical property G(x) may be expressed as a straightforward analytical interpolation of the characteristics of these two binary molecules [61]. Physical property G's average value of is as follows:

$$G(x) = xGAC + (1 - x)GBC \qquad (II - 1)$$

The lattice parameters of ternary alloys, for example, are frequently computed using Vegard's law [62]:

$$\alpha\,(x) \;=\; x\,\alpha AC \;+\; (1-\;x)\,\alpha BC \qquad (\mathrm{II}-2)$$

With:

AC denotes the lattice parameter of compound AC.

BC denotes the lattice parameter of compound BC.

x denotes the molar concentration.

The variation of the band gap Eg, as a function of concentration x may be calculated as follows:

$$Eg\,(Ax\;B\;1-x\;C) \;=\; x\;Eg\,(AC) +\; (1-x)Eg\,(BC) +\; x\,(1-x)b\,(Ax\;B\;1-x\;C) \qquad (\mathrm{II}-3)$$

With:

E_g *(AC)* stands for the gap of the composite material AC.

E_g *(BC)* stands for the gap of the compound BC,

b represents the curvature parameter (bowing), which is frequently demonstrated experimentally.

The structural features and disorder dominating in the ternary alloy's oscillations are the causes of bending.

II.7 LEDs and MEMS Technology

Aluminum nitride (AlN) piezoelectric material is now being investigated as an operator layer in microelectromechanical systems (MEMS). The key benefits of AlN for MEMS

manufacturing are its process compatibility and chemical stability with silicon technology, furthermore its availability of low-temperature procedures for its deposition (300-400 C°). A microelectromechanical system (MEMS) is a microsystem made of semiconductor materials that is around the size of a square millimeter (Figure II.9). It has one or more mechanical elements and employs electricity as an energy source to achieve a sensor or actuator function, with at least one configuration having micrometer dimensions.

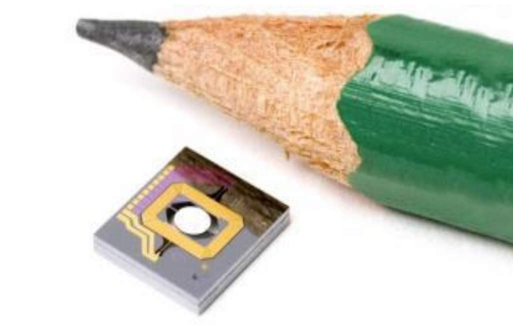

Figure 0I.9: Visualization of the scale of MEMS [63]

The growth of microtechnology centered on MEMS (based on the photolithography principle) has resulted in an explosion of applications and a division of the area. We discover four families that are linked to their application frameworks (Figure II.10).

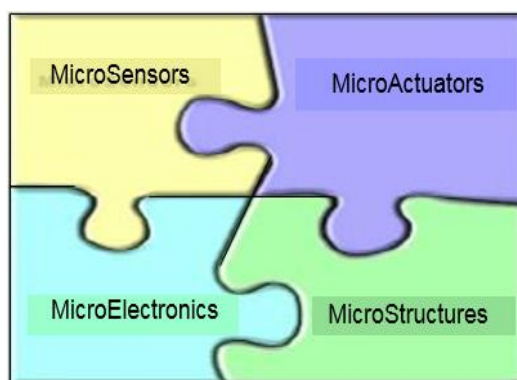

Figure 0I.10: The four sectors of MEMS [64]

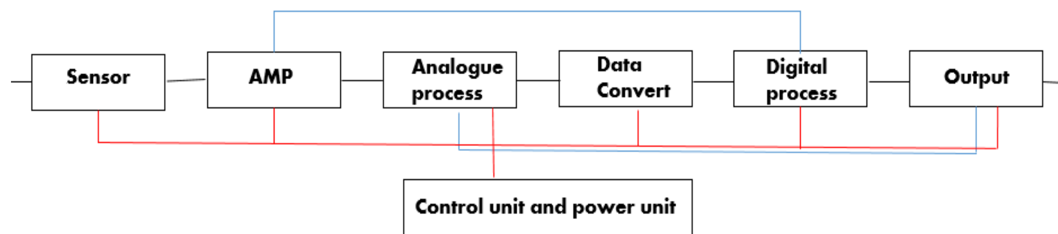

Figure 0I.11: MEMS Technology Diagram [64]

MOEMS is a subtype of MEMS that is an opto-electro-mechanical microsystem. These devices, made of semiconductor materials, can collect, or alter information signals on a tiny scale. MOEMS are currently widely used in video projectors, where millions of mirrors (a few microns apiece) define each picture pixel (DMD technology: Digital Micro Mirror Device or DLP: Digital Light Processor). Figure II.12:

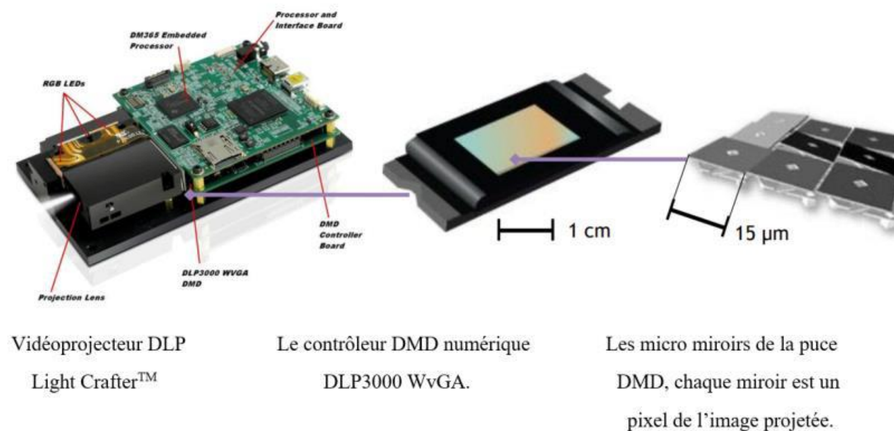

Figure I0.12: DLP Technology images, Texas Instruments [65]

The semiconductor III-N family offers a wide range of technologically significant uses, notably in light-emitting diodes (LEDs). A light-emitting diode (LED) is an optoelectronic device that emits light when an electric current passes through it. When an electric current travels through an LED, it creates monochromatic or polychromatic non-coherent radiation because of the conversion of electrical energy. The earliest LEDs that were

commercialized generated infrared, red, green, and later yellow light [66]. The introduction of the blue LED, together with technological and assembly developments, enabled the emission wavelength band to be covered, stretching from ultraviolet (350 nm) to infrared (2000 nm).

LEDs with high power have begun to penetrate the lighting industry, progressively replacing traditional incandescent and discharge lamps. This advancement is mostly owing to the development of efficient III-N-based blue and white LEDs. LEDs have several advantages, including extended life, compact size, quick reaction, and low power usage (high efficiency). LEDs are now marketed for a wide range of applications, including general lighting, projectors, displays, and so on, because of the huge gain in efficiency they provide over traditional light sources.

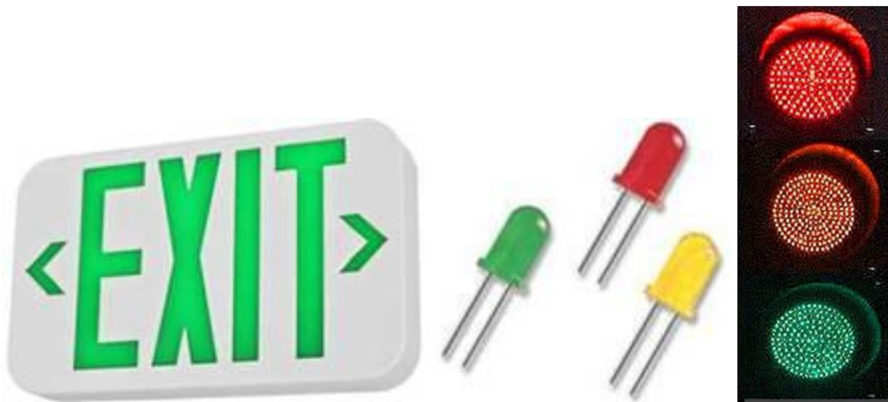

Figure 0I.13: LEDs applications [67]

III. Description of characterization techniques

III.1 Introduction

Thin films play a very important role in all devices; they are used in the industry of semiconductors and are deposited by various techniques.

This chapter is dedicated to describing the experimental techniques that have been used during this thesis. The chapter is organized in two parts dealing with film synthesis, structure, composition and optical analysis.

The aim is to provide a brief description of each apparatus and their operating principles.

III.1.1 X-Ray Diffraction (XRD)

XRD is a non-destructive method for identifying crystalline phases and orientations, determining atomic arrangement, measuring thin film and multilayer thickness, and determining structural characteristics (strain, grain size, epitaxy, phase composition, preferred orientation).

XRD is based on the creation of X-rays in a cathode X-ray tube by heating a tungsten filament in a vacuum to produce electrons, which bombard the target (anode). Cu, Mo, Al, and Mg are the most common anodes. When the incident rays contact with the sample, constructive interference, and a diffracted ray result, according to Bragg's Law.

$$n\lambda = 2d \sin \theta \qquad \text{(III-1)}$$

The wavelength of electromagnetic radiation is related to the diffraction angle and lattice spacing in a crystalline sample by this law [68].

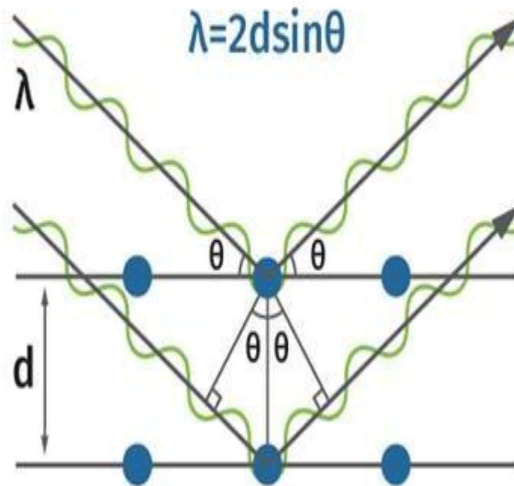

Figure IIII.1: Principle of X-Ray Diffraction analysis [68]

III.1.2 Scanning Electron Microscopy SEM

Scanning electron microscopy SEM uses electron for imaging. The incident electron beam is scanned in a raster pattern across the surface of the sample, and the backscattered or the secondary electrons emitted are detected. When a cathode emits electrons under the application of an extremely high electric field, it is also known as a field emitter-FE-SEM, which gives better images. Although the sample preparation is simple. The electron beam can cause degradation of biological material and therefore can be used for limited samples [69].

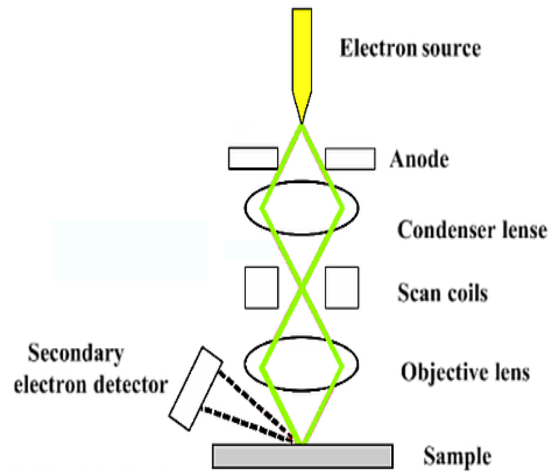

Figure III.2: Principle of SEM [70]

III.1.3 Energy Dispersive X-Ray EDX

EDS or EDX is an analytical method used to characterize a sample's chemical characteristics or determine its element composition. It depends on looking into how a source of X-Ray excitation interacts with a material [71].

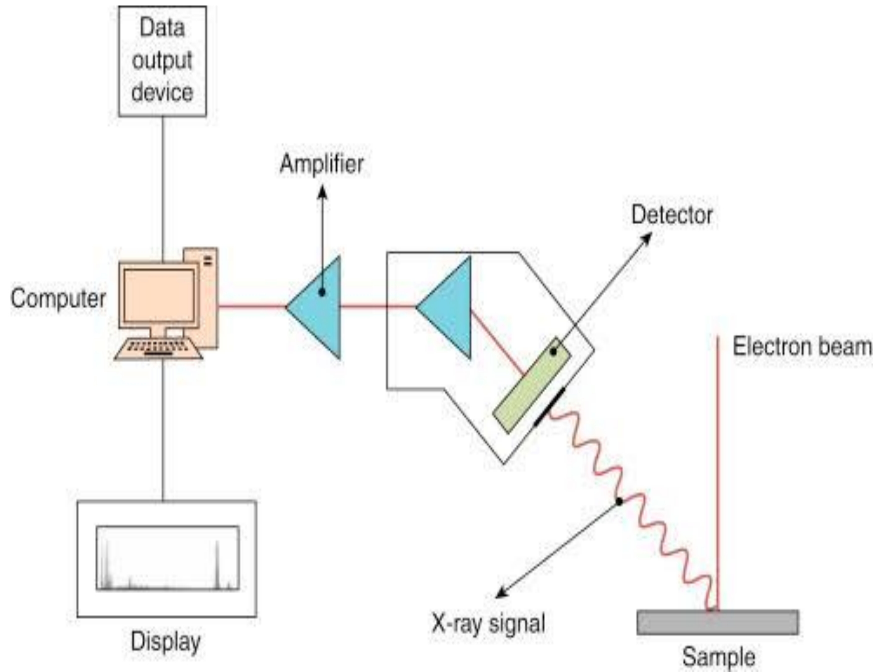

Figure III.3: Principal of EDS [72].

III.1.4 Ellipsometry Spectroscopy

Spectroscopic ellipsometry is a non-contact, non-destructive, and non-invasive optical technique based on changes in the polarization state of light. The measuring geometry is shown in Figure III.4. This is made up of an incident ray of linearly polarized light that is reflected on the sample and then elliptically polarized in most cases.

Ellipsometry is used to measure and, both of which describe the output elliptical polarization state, and to determine thin films, surface roughness, and thickness. According to the parameters, Δ and ψ are connected to the complex Fresnel reflection coefficients [73].

$$\Delta = \delta i - \delta r \qquad (III-2)$$

$$\tan(\psi) = \frac{r_p}{r_s} \qquad (III-3)$$

$$\rho = \frac{r_p}{r_s} = \tan(\psi) e^{i\Delta} \qquad (III-4)$$

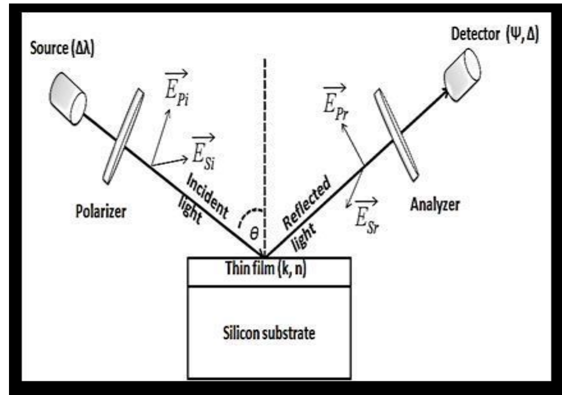

Figure IIII.4: Schematic diagram of the geometry of an ellipsometry measurement [74]

There are two models for determining thickness and refractive index. The Cauchy dispersion relation works well with transparent materials, but piezoelectric materials are transparent only for light with a photon energy less than their band gap (3eV). We also analyzed the Tauc-Lorentz Oscillator relations [74] to get the correct optical constants.

III.1.5 Ultraviolet-Visible (UV-Vis) Spectroscopy

The optical properties of semiconductors, such as the band gap and refractive index, are routinely investigated using UV-Vis reflectance and absorption spectrophotometry. Because they correspond to the two components of light-matter interactions, reflectance and absorption measurements are complementary to each characterization technique.

Light with wavelengths ranging from 190 nm to 1200 nm can be generated by the light source for both absorption and reflectance measurements. The energy of an electromagnetic wave can be calculated using Equation (III-5):

$$E = \frac{hc}{\lambda} \qquad (\mathrm{III}-5)$$

Where E is the energy in eV (1 eV = 1.602×10^{-19} J).

h is the Planck's constant (6.626×10^{-34} J.s).

C is the speed of light (3×10^{8} ms^{-1}) and λ is the wavelength of the light.

As a result, UV-Vis spectrophotometry can measure energies between 6.53 eV and 1.55 eV. The light shines perpendicularly onto the sample surface to measure the reflectance,

and the detectors are positioned around the light source to measure the reflected light near the surface normal. The relationship between the absorption coefficient and the band gap is shown in Equation (III-6).

For direct and indirect optical transitions, n = 1/2 and 2 correspondingly. The x intercept can be calculated by extrapolating the linear region in the Tauc Figure, which yields the band gap of the materials.

$$\alpha h\nu = (h\nu - Eg)\, n \qquad (III - 6)$$

The background calibration for UV-VIS reflectance was done by shining light onto the black specimen stage, while reference measurements were taken on a silicon (Si 111) substrate [75].

III.1.6 X-Ray Photoemission Spectroscopy (XPS)

X-ray Photoelectron Spectroscopy (XPS), commonly known as ESCA, is a type of X-ray photoelectron spectroscopy (electron spectroscopy for chemical analysis). The photoelectrons emitted by irradiating the sample with an X-ray beam are analyzed by the XPS technique, which involves evaluating the energies of the photoelectrons emitted by irradiating the sample with an X-ray beam. MgK (1253.6 eV) and AlK (1253.6 eV) are the most widely used sources (1486.6 eV). The incoming photons penetrate the solid only to a limited depth (1–10 m) and react with the atoms in this region via the photoelectric effect, ejecting excited electrons with kinetic energy equal to [76]:

$$Ec = h\nu - E_L - w_a \qquad (III - 7)$$

With:

$h\nu$: Photon energy.

E_L: binding energy.

W_a: work function.

When the photon's energy is only higher than the binding energy of the ripped-off electron, photoemission efficiency is highest [77]

The elemental makeup, chemical state, and electronic state of the elements present in a material are all measured using XPS.

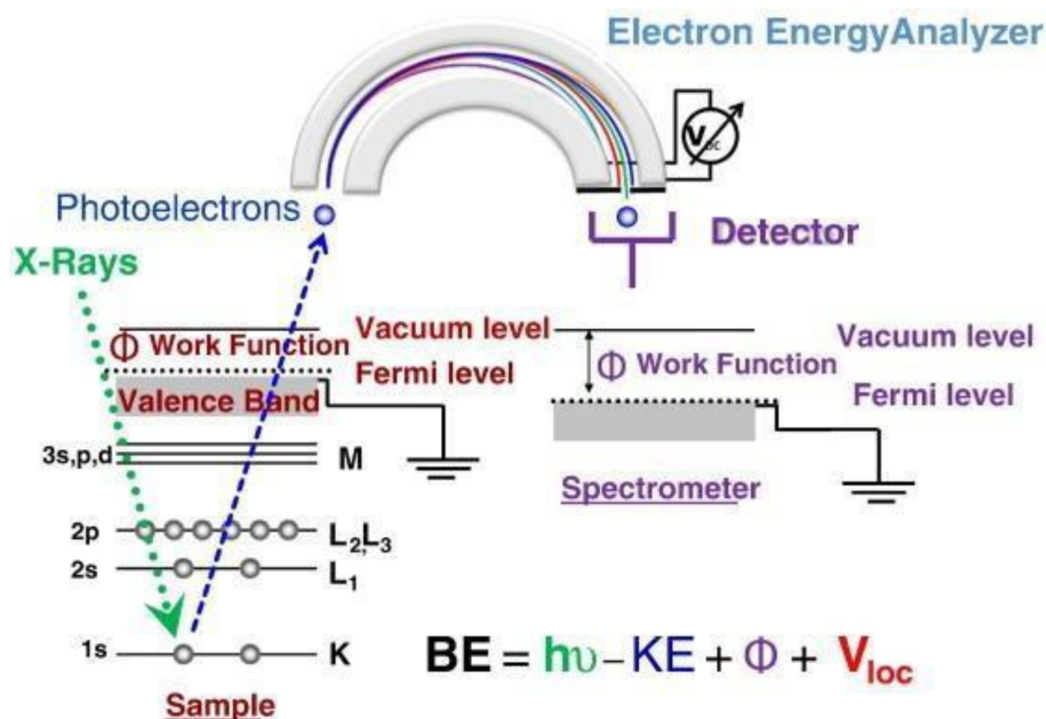

Figure IIII.5: Schematic diagram of the XPS technique [77].

III.1.7 Fourier Transform Infrared Spectroscopy (FTIR)

Fourier transform infrared spectroscopy is an analytical technique for measuring how much light a sample absorbs at each wavelength and obtaining information about the vibration frequencies of the bonding system of materials. It is used to measure how much light a sample absorbs at each wavelength and obtain information about the vibration frequencies of the bonding system of materials [27].

The sample is passed through the interferometer (the interferometer in an FTIR operates on the same principles as the one employed in the Michelson–Morley experiment) to the detector by infrared light from the source. The signal is then amplified before being converted to digital. The Fourier transform analysis is then carried out. The typical IR range utilized in FTIR is 400 cm-1 to 4000 cm-1, which corresponds to photons with sufficient energy to cause a group of atoms to vibrate with respect to their bonds [78].

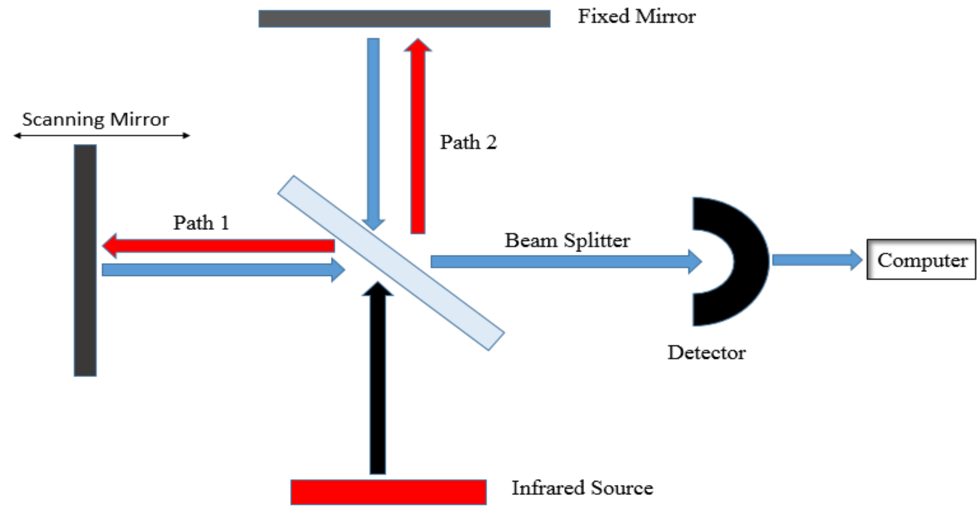

Figure III.6: A schematic of the interferometer used in a Fourier Transform Infrared Spectrometer.

B/ EXPERIMENTAL AND SIMULATION PART

IV. Material Preparation and Analysis

IV.1 Introduction

This chapter is devoted to the description of four different group of samples (Sc_xAl_{1-x} N) with different percentage(x) of scandium and different thickness of the thin films (ScAlN) and the molybdenum, platinum, titanium interlayers.

All the samples were prepared using co-sputtering with two targets (Sc and Al) both at 99,999% pure at different temperatures applied to the substrate.

The air-reactive silicon substrates are first chemically stripped in a bath of hydrofluoric acid, in order to eliminate the oxide layer thus produced. This operation is carried out just before deposition in order to avoid the formation of oxide during storage of the substrate. Nitrogen gas is pumped into the chamber at a constant rate to ensure the Al and Sc atoms creating bonds together and with Nitrogen to create ScAlN molecules on the substrate surface.

After the preparations of the samples ($Sc_xAl_{1-x}N$), we characterized them by using Scanning Electron Microscopy (SEM), X-Ray Diffraction (XRD), UV-VIS spectroscopy, Spectroscopic ellipsometry (SE), X-Ray Photoemission spectroscopy (XPS) and Energy dispersive X-ray EDX.

In order to show the effect of scandium ratio on the relative permittivity we use effective medium approximation more specifically plan layer effective medium and Maxwell Garnet method that is the most adapted to be used with ellipsometry spectroscopy.

IV.2 Characterization of ScAlN Samples

The Fraunhofer FEP in Dresden (Germany) and Evatec AG in Switzerlan provided four types of samples ($Sc_xAl_{1-x}N$) with variable percentages (x) of scandium and different thicknesses of thin films (ScAlN). X-Ray Photoemission Spectroscopy (XPS), X-Ray Diffraction (XRD), UV-VIS spectroscopy, and Spectroscopic Ellipsometry were used to evaluate these samples, which were generated by co-sputtering with two targets at different temperatures (ES). We employ effective medium approximation, namely the plan layer effective medium and the Maxwell Garnet method, which is well suited for ellipsometry spectroscopy, to determine the effect of the scandium ratio on relative permittivity.

IV.2.1 First Group

Scandium aluminum nitride ($Sc_xAl_{1-x}N$) thin films with a thickness of approximately 100 nm were generated utilizing co-sputtering from a scandium and an aluminum target at ambient temperature 300°C on (100) silicon substrates. Wafers were cleaned with chemical processes and sonar bathes to lose any substances on the surface between silicon and ScAlN.

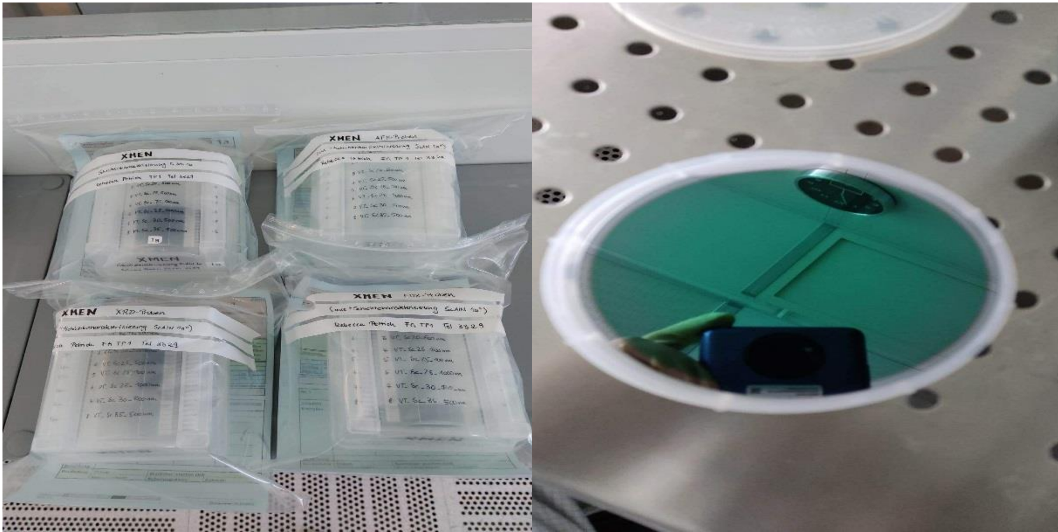

Figure IV.1: The samples of the first group

Figure IV.2: Co-sputtering machine

IV.2.1.1 Co-Sputtering

Thin film deposition techniques include sputtering. The method involves bombarding the target material (which can be an element, alloy, compound, or mixture) with energetic ions (often Argon) created in plasma, with free electrons ejected from the negatively charged target surface hitting with the Argon gas atoms' outer electronic shell. A high-speed attraction between the positively charged inert gas atoms and the negatively charged target material results from the collision's momentum, which "sputters off" atomic-sized particles from the target source material. These particles pass through the sputter coater's vacuum deposition chamber and deposit a thin material film on the substrate's surface. Low-pressure plasma can be used to execute this operation in a vacuum chamber [79].

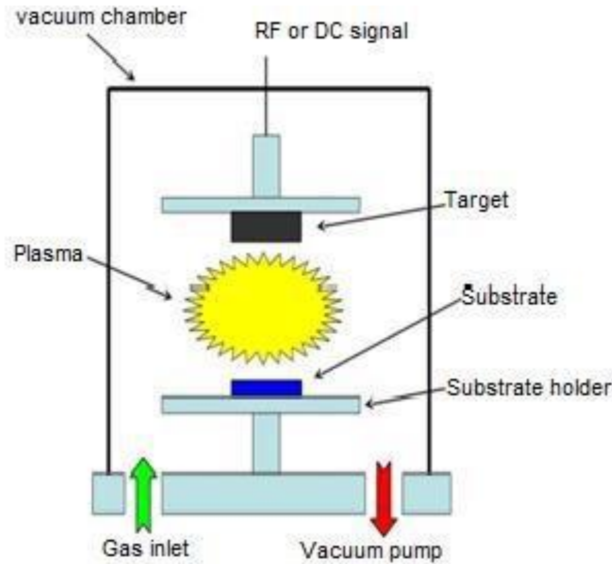

Figure IV.3: Schematic of a typical sputtering system in either the DC or the RF configuration [79]

Co-sputtering occurs when two target materials are sputtered in the vacuum chamber at the same time, and it is frequently used in conjunction with reactive magnetron sputtering to create thin films that are compounds, such as alloys or composites. In the optical and architectural glass industries, it is widely employed. Reactive co-sputtering of two target materials, such as silicon and titanium with dual magnetron sputtering, allows for the precise and careful control of the refractive index or shading effect of the glass for a variety of applications, from large-scale surfaces, like skyscraper architectural glass, to eyewear. It is also commonly employed in the manufacture of solar panels [80].

IV.2.1.2 Spectroscopic Characterization Techniques of the First Group

IV.2.1.2.1 X-Ray Diffraction (XRD)

To make the new samples we had to consider many variables to arrive at the best set up we grew AlN (Aluminum nitride) at room temperature and at 300°C. Both samples were analyzed using XRD. Figure IV.4 displays the results of the analysis. It indicates that the AlN sample measured at room temperature is R-planned and highly polycrystalline. In contrast, the AlN sputtered at 300°C is C-planed and quasi-monocrystalline, with the (002)

phase having the highest intensity at approximately theta=36°. Based on this information, we prepared samples of ScAlN (scandium aluminum nitride) by co-sputtering AlN and ScN at 300°C. The elaboration parameters were changed to obtain samples of varying Scandium percentages. To see the effect of varying Sc percentages on the compound parameters (Dielectric function, crystal structure, Lattice parameters)

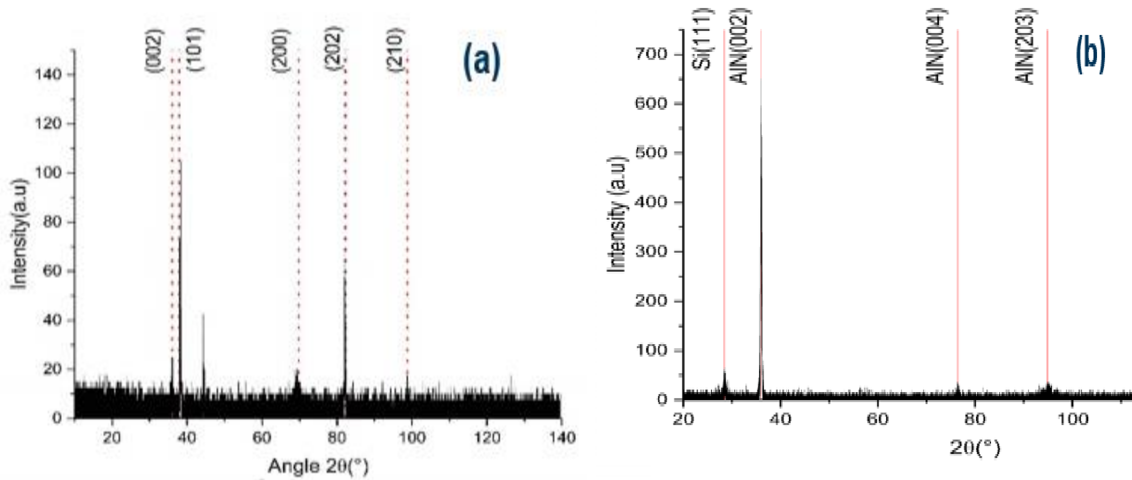

Figure IV.4: (a) AlN sputtered at Room temperature. (b) AlN sputtered at 300°C.

An X-Ray diffractometer was used to identify crystal phases. As seen in the image, the sample except for the peak for the AlN Wurtzite structure and the Si substrate and showed no other contaminants. The XRD pattern showed several peaks corresponding to the AlN crystallographic planes (002), (101), (200), (202), and (210). The intensity and the dominant orientation were greatest in the (100) plane. The (002) peak began to take center stage as the prevailing orientation [81].

Figure IV.4 show the peaks of pure AlN and ScAlN thin films. The (002) peak and small (111) peak of Si were shifted to a slightly lower angle compared with that of AlN, indicating an expansion of the crystalline lattice according to Bragg's law [82].

An effective method for checking perfection when the surfaces are not parallel is the rocking curves (Omega scan). The sample is tilted, and the detector is fixed at the expected BRAGG reflection's center. The top of a flawless crystal will be extremely sharp.

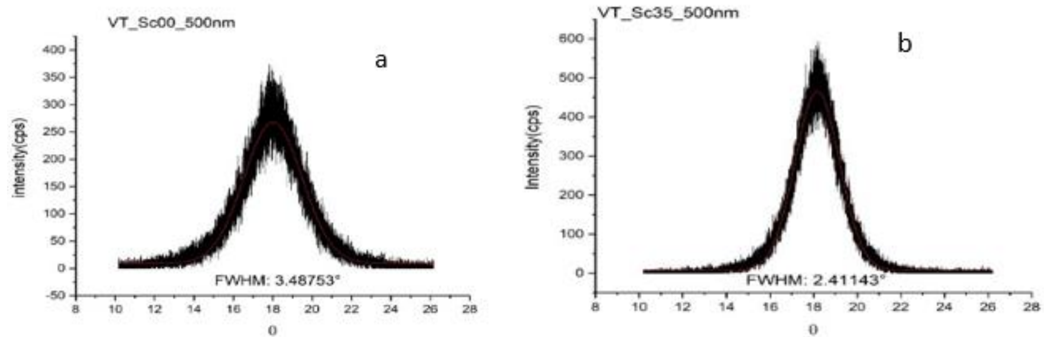

Figure IV.5: (a) XRD scan rocking curves of ScAlN sample, (b) XRD scan rocking curves of $Sc_{35}Al_{65}N$ sample.

A rocking curve measurement is performed by rocking the thin film sample (500nm) while the detector is fixed at a fixed 2Θ angle to record diffraction intensities to check the full width at half-maximum intensity (FWHM) of the peak.

The density of edge dislocation in the XRD scan rocking curves is inversely proportional to the (102) plan's FWHM value. the FWHM of the (102) plans are discovered to be nearly identical to those of the (002) planes at various Scandium ratios as shown in Figure (IV.5) and that the FWHMS of both the 002 and 102 planes decreases with increasing Scandium ratio. According to this finding, greater scandium is necessary for the development of an AlN layer of superior quality. Nevertheless, when the ratio exceeds a certain value the full width at half-maximum starts increasing again which is consistent with the assumption of a phase separation between ScN and AlN the compound is leaning towards becoming cubic.

The rocking curve of the ScAlN (002) peak was also measured and is shown in Figure (IV.6). The full-width-half-maximum (FWHM) of the (002) peak for the AlN film and for the ScAlN film, indicating that the c-axis of the ScAlN film is well-aligned and predicting good piezoelectric properties [69].

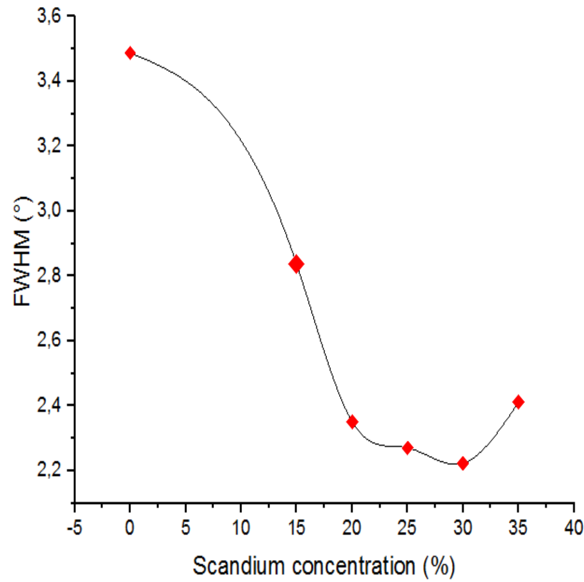

Figure IV.6: Changes in FWHM as a function of Scandium percentage

The x-ray diffraction measurements showed a phase shift in the crystal orientation depending on the increase of the scandium percentage, up until 25%, and then we can see a phase separation that would also explain the behavior of the refractive index.

High ratio will reduce the crystals quality and is not favorable for the formation of AlN crystals in high quality.

IV.2.1.2.2 Scanning Electron Microscopy SEM

The samples were then put under an SEM (Scanning Electron Microscopy) to determine the roughness of the samples at different magnifications and submitted to different potentials and to analyses the morphology of the samples (Figure IV.7).

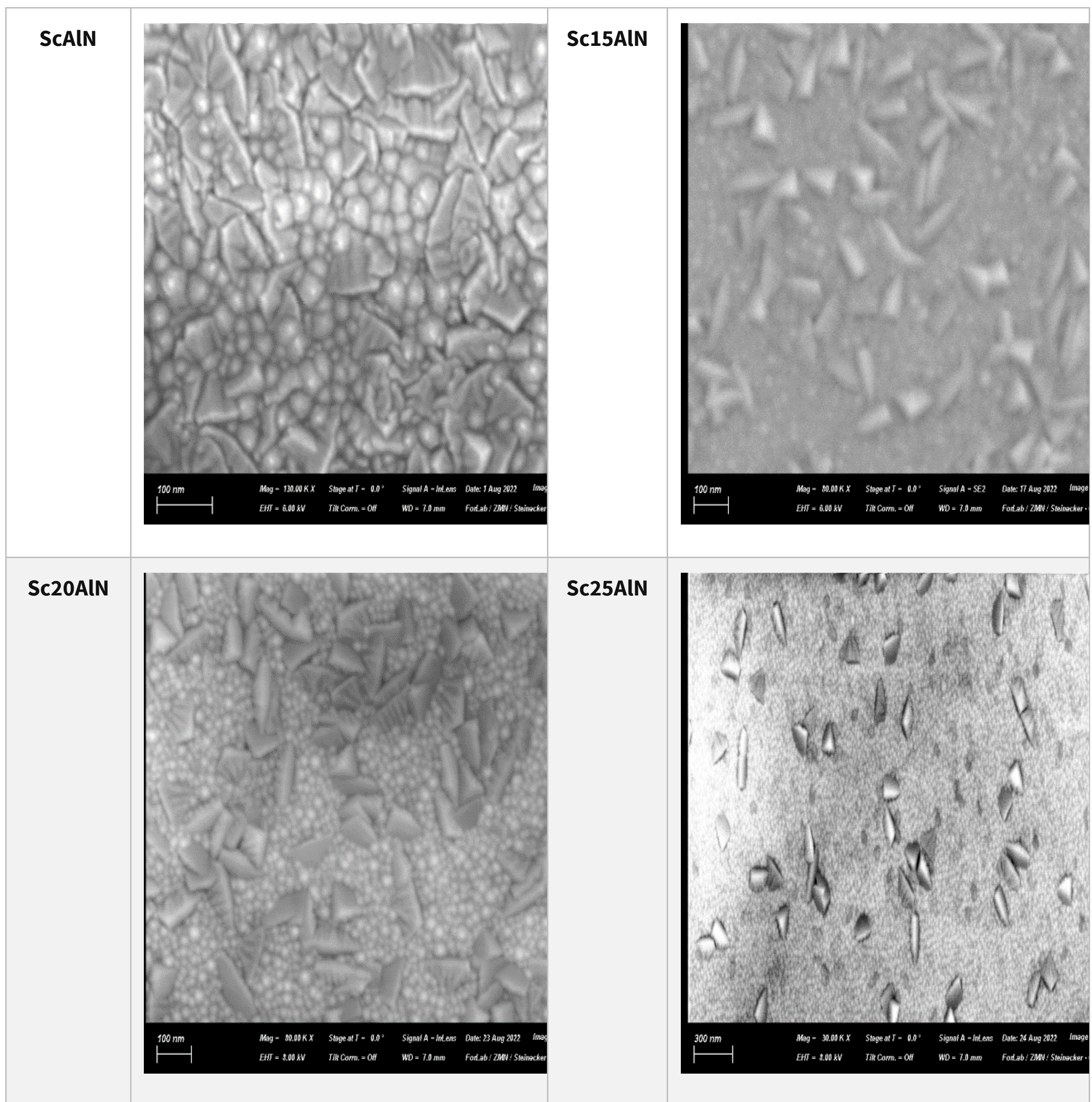
ScAlN
Sc15AlN
Sc20AlN
Sc25AlN

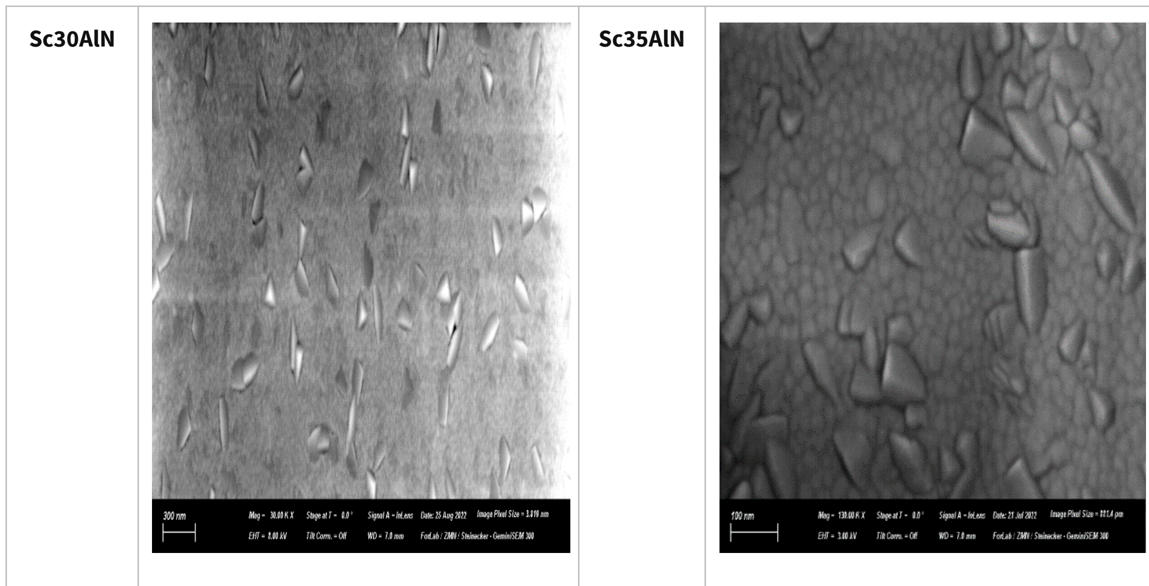

Figure IV.7: Scanning electron micrograph of ScAlN samples.

These figures shows an SEM of the ScAlN surface deposited on silicon. The surface appeared to be coated with small particulates having a grain size (The film consists of many grains).

The pictures of AlN layers developed at various scandium ratios are shown in plan-view and cross-sectional views in Table II.1, there were numerous evenly spaced whiskers this observation matches the XRD patterns because of their distinct orientations.

Higher magnifications revealed that the wires grew perpendicular to the substrate surface.

IV.2.1.2.3 Energy Dispersive X-Ray EDX

After depositing the layers, the percentage of scandium present in each sample had to be investigated compared to the expected values from the elaboration process. EDX was used to determine the samples chemical composition Table IV.1.

Sample	Rand Worth [At. -%]	Deviation [At. -%]	Worth in between [At. -%]	Deviation [At. -%]	Mid value [At. -%]	Deviation [At. -%]
Sc15AlN	8,9	-6,10	8,78	-8,22	8,78	-8,22
Sc20AlN	14,72	-5,28	14,49	-5,51	14,42	-5,58
Sc25AlN	20,94	-4,06	20,87	-4,13	20,63	-4,37
Sc30AlN	27,36	-2,64	27,07	-2,93	27,02	-2,98
Sc35AlN	33,78	-1,22	33,26	-1,74	33,56	-1,44

Table IV.1: Comparison of ScAlN deviations measured at 6KV.

For samples with a high scandium content, the deviation is smaller (absolute and relative). EDX line scan measurement shows the chemical composition of the sample in the Table IV.1 indicates that the values of scandium percentage present in the compound is overall lower than the expected percentages of the growth calculated from manipulating the sputtering parameters, however the higher percentages , lower deviation. We can deduct from this that the allowing processing time in the initial phase once the crystals are formed the compound gains higher concentrations faster. It should be taken under advisement that the samples used in this work will retain their names, but the scandium percentages are what we see in the table above.

To determine the above-mentioned parameters, we measurand our samples with XRD to determine the crystal structure of the ScAlN growth and observe the peak shift dependence to Sc percentage Figure IV.8.

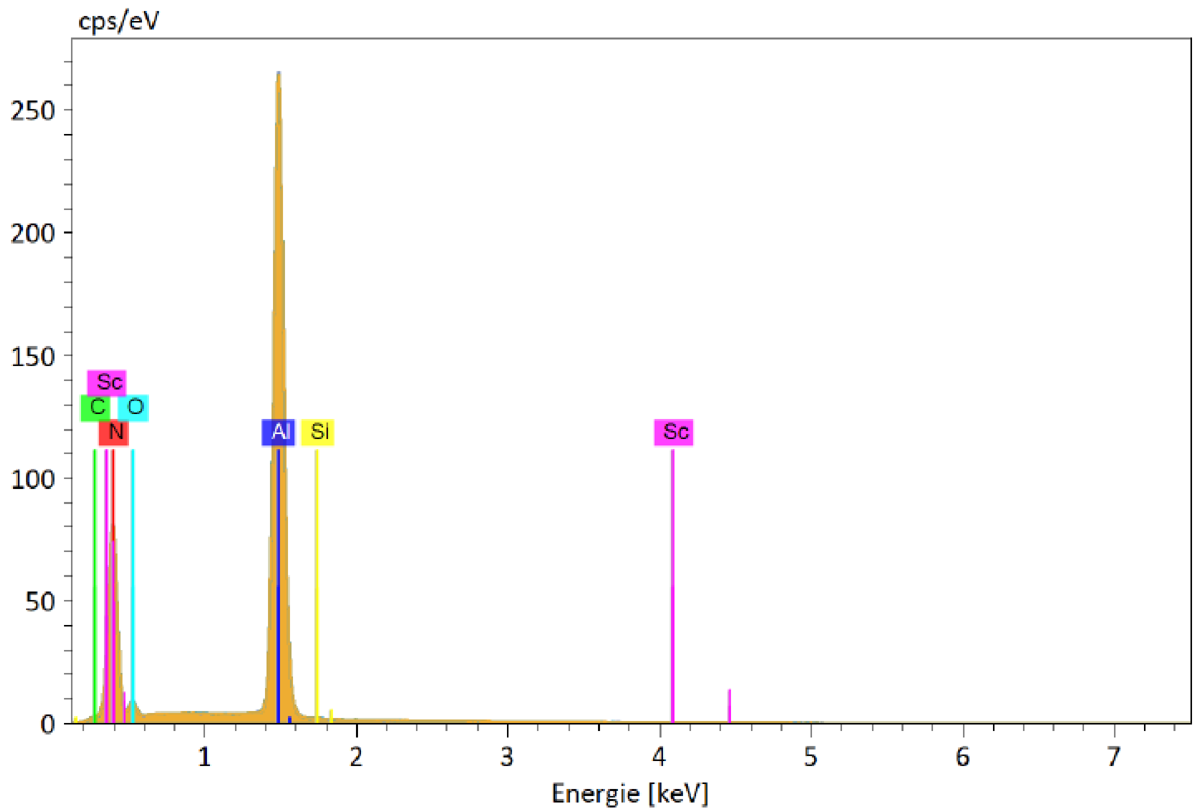

Figure IV.8: Sample chemical composition indication the scandium percentage present in the samples verses the expected values at 6 KV.

Figure shows EDX results with the peaks as labelled representing chemicals as expected. We can see Al, Sc and Nitrogen, The main component of the topmost layer.

We see also silicon peak representing the substrate, meaning the voltage used penetrate the layer and probed the substrate. Even though the samples where thoroughly cleaned substances such as carbon and oxygen are extremely hard to clean from the surface.

.

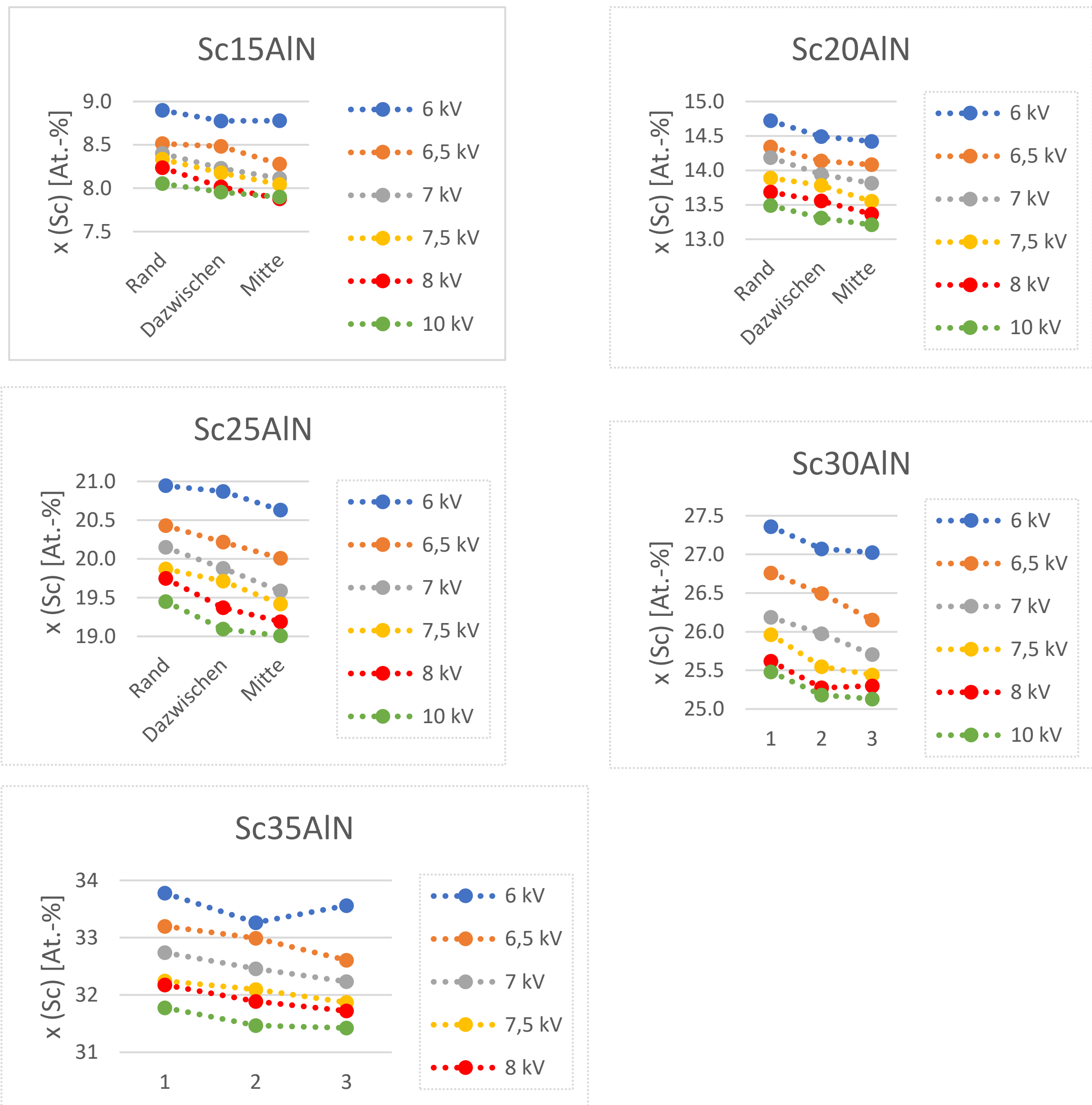

FigureIV.9: Sample chemical composition indication the scandium percentage present in the samples verses the expected values at different voltages.

With increasing acceleration voltage, a smaller proportion of scandium is measured (although sample is unmodified). Scandium portion is used for all samples and acceleration voltages from the position as follows measured:

- At the edge most
- in between lies also the values in between.

- In the middle least

Almost all values deviate quite strongly from the actual composition of the sample.

IV.2.1.2.4 Ellipsometry Spectroscopy

Ellipsometry spectroscopy (SE) was then used to determine the layers thicknesses, roughness, and dielectric function of each sample then they were compared to each other to see the influence of Sc percentage on the dielectric function. The samples were also measured in various positions. Figure (IV.10) geometrically relevant to the wafer uniformity and then analyzed to determine the sample surface uniformity.

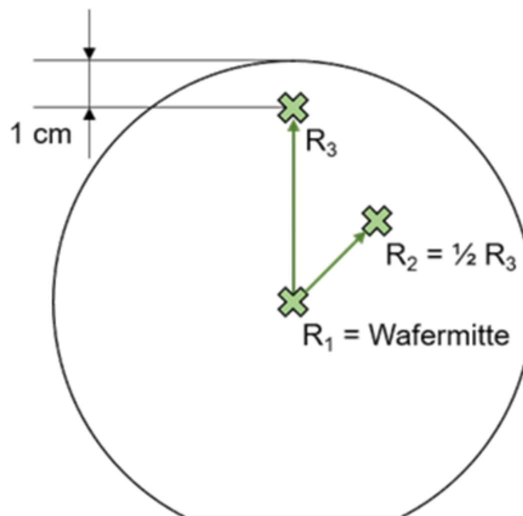

Figure IV.10: Wafer geometry and line scan positions

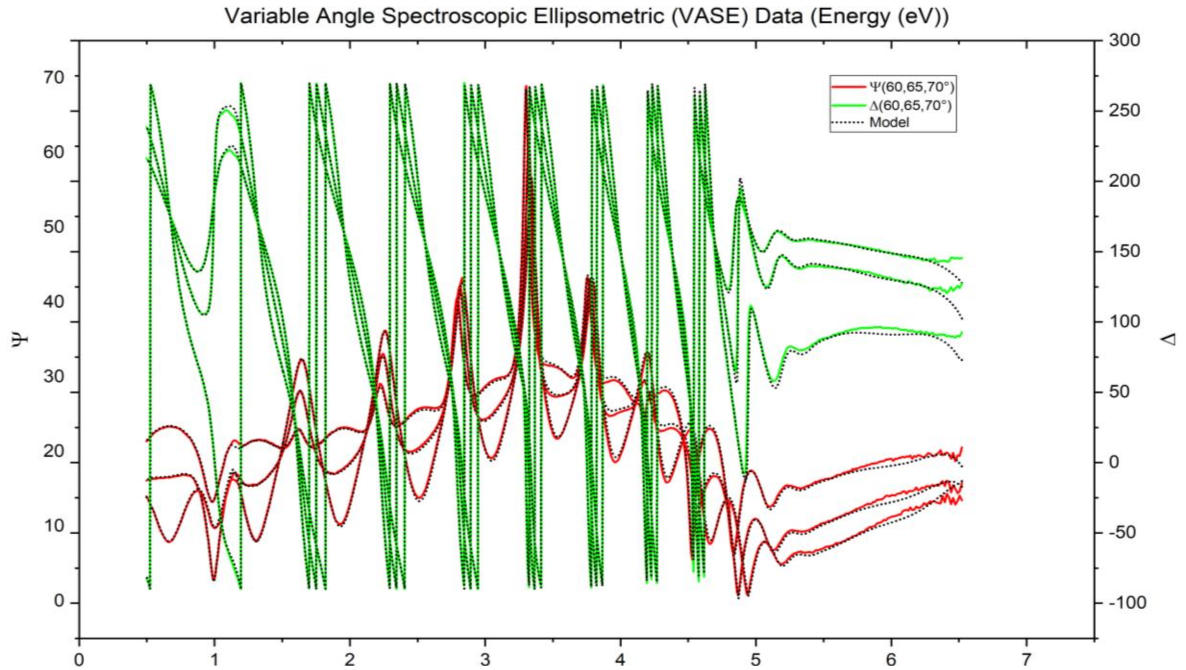

Figure IV.11: Experimental and generated data of sample SC%=25

Here is an overview of the results of a sample with 25% Sc. It shows that the fit is quite good except at the higher energy levels which is overly sensitive to the surface roughness.

- The MSE of this model is at 10.048.
- The thicknesses of the samples vary between 478 and 509 nm with an uncertainty of +- 0,2nm.
- In addition, a roughness of 5to10nm with an uncertainty of 0,1nm.

We have determined the dielectric function (DF) and thickness of the samples by means of spectroscopic ellipsometry in the spectral range (190-2500) nm. The measured spectra of the ellipsometry angles Ψ and Δ as well as of depolarization were then analyzed by a multi-layer model consisting of substrate, ScAlN thin film and a surface roughness bounded by air. The DF of ScAlN have been modelled with a B-spline function approach considering both, $\varepsilon_{\perp}$ and $\varepsilon_{\parallel}$, i.e., the DF perpendicular and parallel to the optic axis of this optically uniaxial material. The surface roughness we have modelled by an isotropic mixture of 50% air and 50% ScAlN DF.

XRD measurements were performed with an XRD Bruker D8HR with a Cupper anode (λ= 1.5406 Å) and in 2θ range (20-140) °. Diffract EVA analyzed the results with the PDF4 database as references to obtain lattice constants as a function of Sc content as well as information on structural quality.

Information on surface roughness and real structure properties we have obtained from AFM measurements carried out using a Dimension 3000 AFM. We used tapping mode with cantilever resonant frequency of 53 kHz. Measurement was performed on a square area of 2 μm.

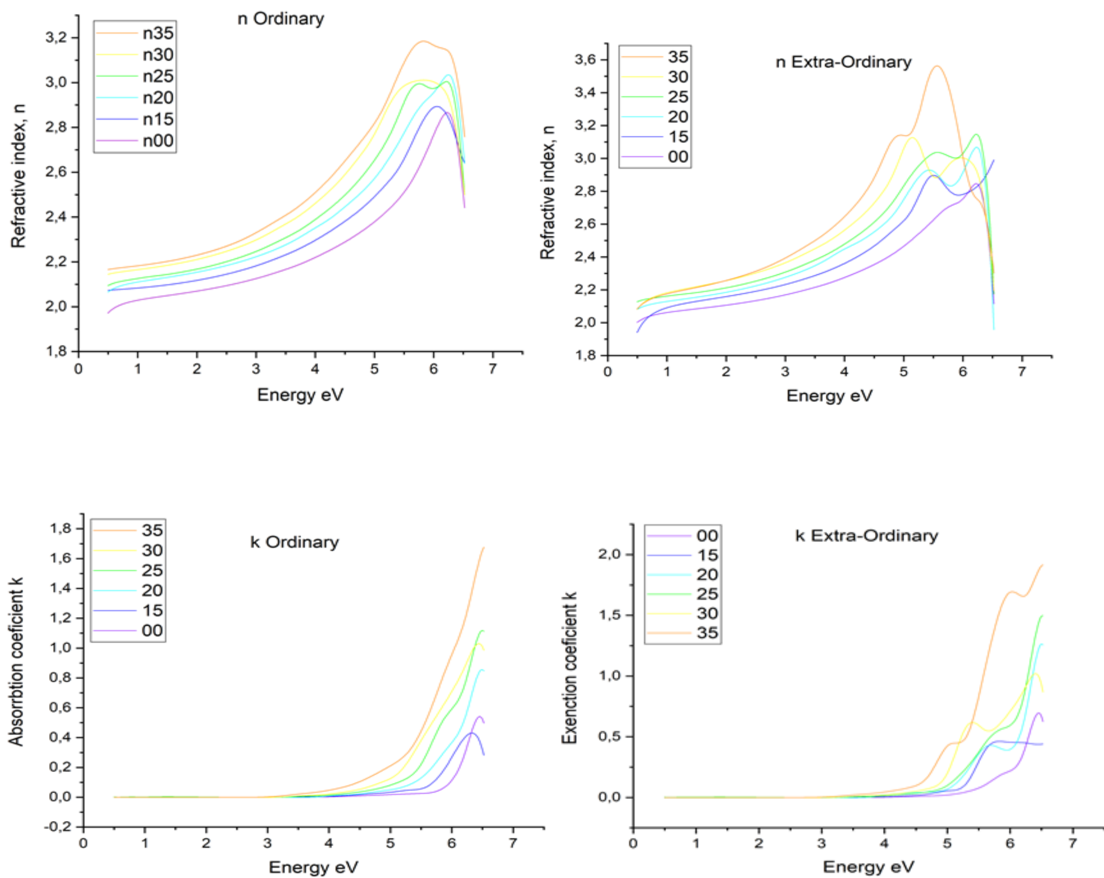

Figure IV.12: Dielectric Function by SE of different Sc percentages.

The calculated ε ordinary and extraordinary refractive indices and absorption coefficients show that the refractive index is increasing notably with the increase of the scandium percentage; however, we see a strange behavior in the percentages above 25%, which is

probably related to a phase separation due to the increase of scandium atoms in the crystal structure.

IV.2.2 Second Group

We have two types of samples, five samples with molybdenum interlayer and the other without it [Fraunhofer FEP in Dresden (Germany)]:

- Scandium aluminum nitride ($Sc_xAl_{1-x}N$) thin films with a thickness of approximately 100 nm were generated utilizing co-sputtering (Figure II.2) from a scandium and an aluminum target at ambient temperature 300°C on (100) silicon substrates with a molybdenum interlayer.
- The other sample contains 10% Scandium and is coated on silicon at a thickness of 500 nm. The percentages of scandium and layer thickness of each sample are shown in the Table IV.2 below:

Samples	Scandium content [%]	Thickness [nm]
1	6	421
2	12	169
3	18	161
4	24	159
5	36	165

Table IV.2: Scandium content and ScAlN thickness

X-ray spectroscopy was used to determine the scandium content of these samples, and a Sentech 500 Ellipsometry was used to determine the film thickness.

IV.2.2.1 Spectroscopic Characterization Techniques of the Second Group

IV.2.2.1.1 Ultraviolet-Visible (UV-Vis) Spectroscopy

In this thesis, we used UV-VIS spectroscopy type Cary 5000, version 1.12, for the characterization of the samples (Table IV.2). It has a scanning range of between 250 nm and 2500 nm.

We start by calibrating the machine with an integrating sphere (spatially integrating radiant flux). The sample is then put at a port opening opposite the entrance port, where it reflects the incident flux. Graphs excel tables, or both are used to present spectroscopic data. Version 3.00 of the software that comes with this computer.

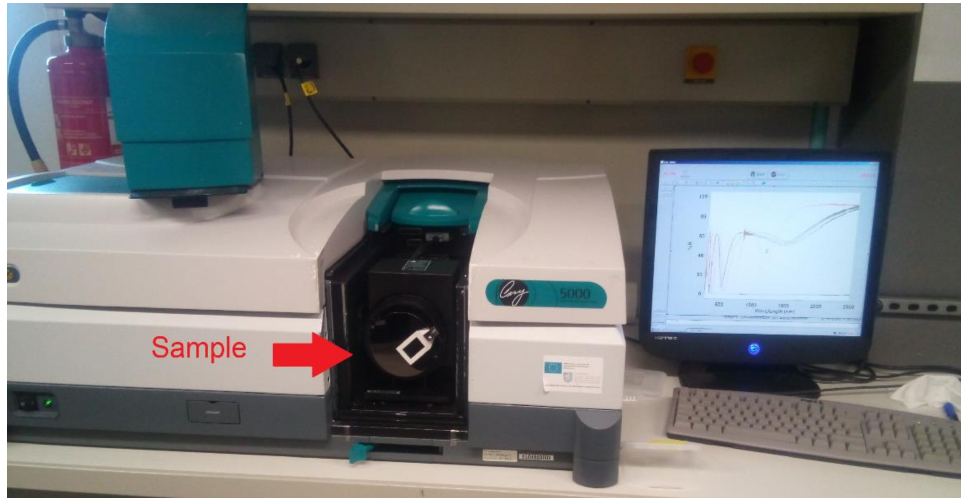

Figure IVV.13: Cary 5000 UV-Vis spectroscopy with software.

We acquired these reflectance curves against wavelength after measuring and characterization of the materials.

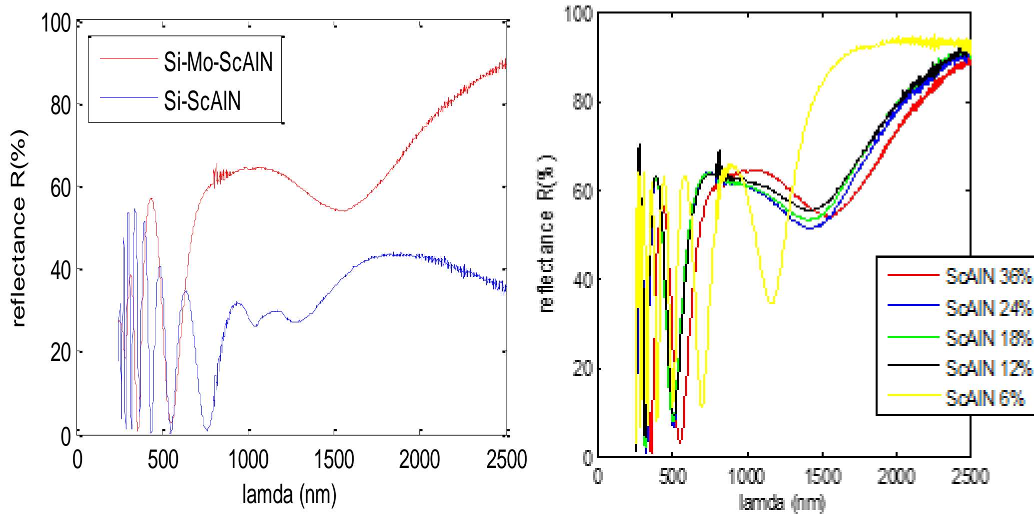

Figure IV.14: Reflectance spectra of the scandium aluminum nitride.

Because molybdenum is a metal with high reflectivity (>400 nm), ScAlN placed on the silicon substrate and on the molybdenum, layer has a higher reflectance than ScAlN deposited simply on the silicon substrate.

In the UV area, there is increased oscillation (250 nm-400 nm). The thickness of the layers is to blame for this. Because the sample with a layer of molybdenum has a lower reflectance than the one without, molybdenum is absorbent in this location.

The Kubelka-Munk equation was used to compute the optical band gap energy (E_{gap}), which is based on the transformation of diffuse reflectance measurements to predict E_{gap} values with high precision. It is particularly useful in the case of endlessly thick samples. The Kubelka-Munk for any wavelength is described by:

$$F(R) = \frac{(1 - R_\infty)^2}{2R_\infty} = \frac{K}{S} \qquad (IV - 1)$$

Where: *F(R)* is the Kubelka-Munk function or absolute reflectance.

k is the absorption coefficient and so is the scattering coefficient.

Finding the *F(R)* value and plotting a graph of $[F(R)h\nu]^{1/2}$ against h is the next step.

Extrapolating the linear section of UV-Vis curves yielded E_{gap} values.

The graphs of $[F(R)h]^{1/2}$ against photon energy were drawn using the MATLAB application.

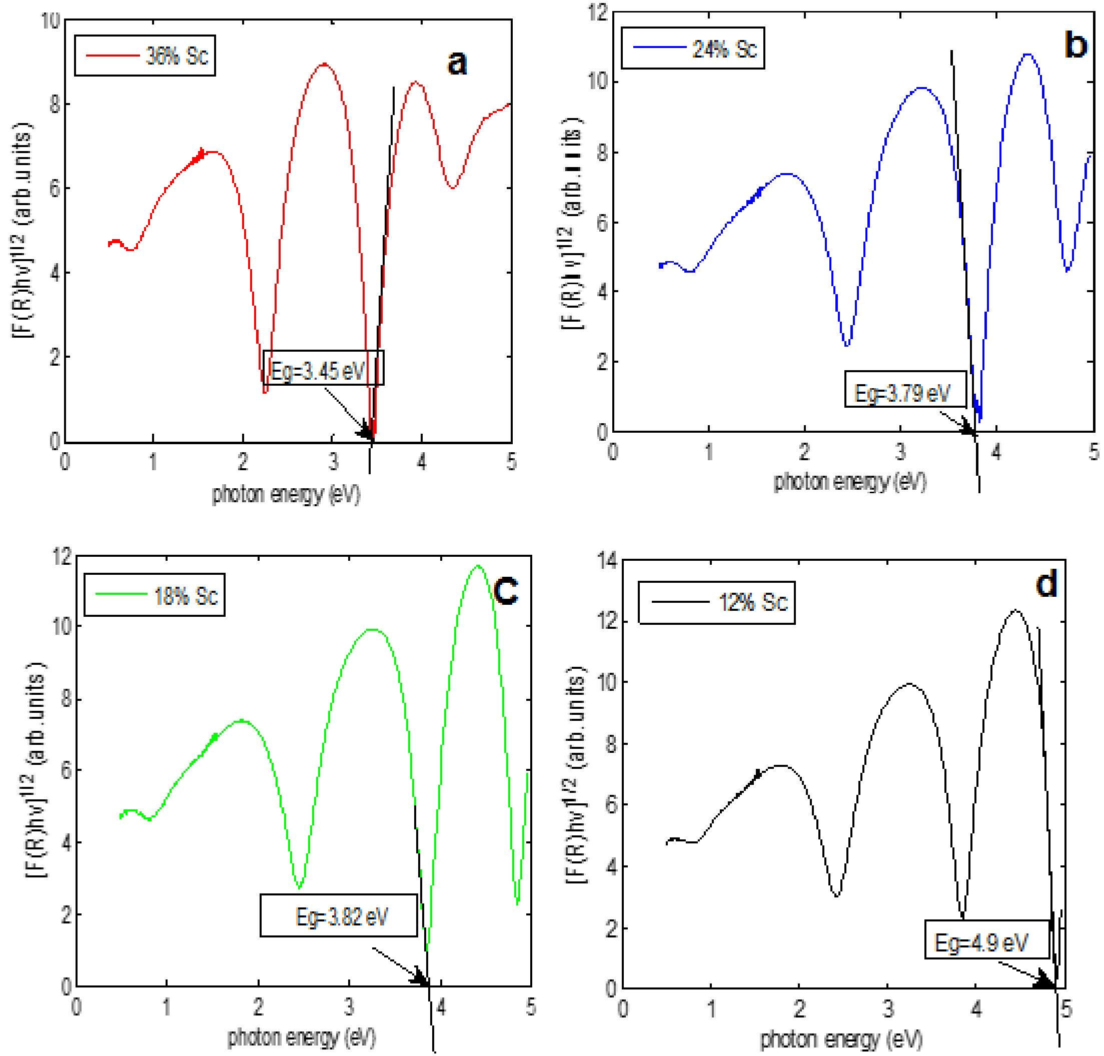

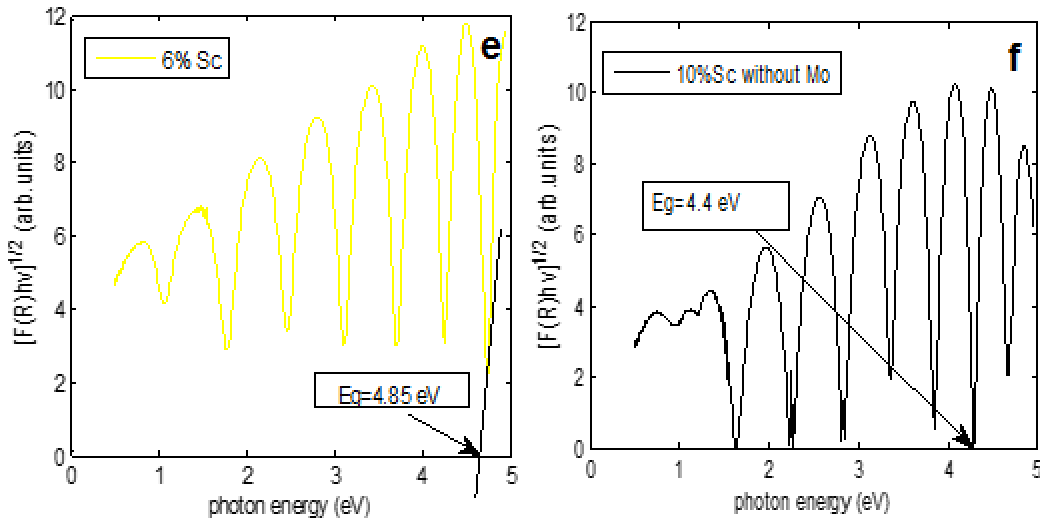

Figure IV.15: a, b, c, d, e, f showing band gap for ScAlN with 6%, 12%, 24% and 36% of scandium, respectively.

Scandium content x [%]	Photon energy [eV]
6	4.85
12	4.9
18	3.82
24	3.79
36	3.45

Table IV.3: Photon energy of $Sc_xAl_{1-x}N$ samples.

In the UV, however, the binding energy and scandium concentration are inversely related.

As a result, as the scandium percentage rises, the lattice shrinks, resulting in a smaller distance between the conduction and valance bands, and hence a smaller band gap.

IV.2.2.1.2 X-Ray Photoemission Spectroscopy (XPS)

We used X-ray photoelectron spectroscopy to describe the samples (ScAlN). ScAlN samples are irradiated with monochromatic X-rays (AlK with an energy of 1486.6 eV) for the procedure to work. To avoid contamination of the material and get spectra with high resolution, XPS experiments must be performed at a pressure of 2.10^{-8} mbar in ultra-high vacuum. Argon beam sputtering was used to clean the samples previously polluted by the atmosphere. The surface is attacked with high-energy argon ions, which causes surface adsorbates to be removed.

The goal of this XPS investigation of ScAlN samples is to acquire an accurate quantification of all elements present in the sample as well as to identify any potential contaminants. The measurements were collected at a center for micro and nanotechnology (ZMN-Ilmenau).

Figure IV.16: Ultra-high vacuum system with an attached XPS system.

Following characterization, we discovered the following spectrums and Table:

Because the scandium-to-aluminum ratio is 0.3, the sample contains much more aluminum than scandium.

Element	O1s	Sc2p	N1s	C1s	Ar2p	Al2p
Atomic concentration [rel. at%]	12,3	13,9	36,4	1,1	3,6	32,7

Table IV.4: The elements existing in the sample and their relative atomic concentration.

Based on the peak area, we utilized the program (CASA XPS) to determine the amount of each element in the sample (which equals the peak intensity).

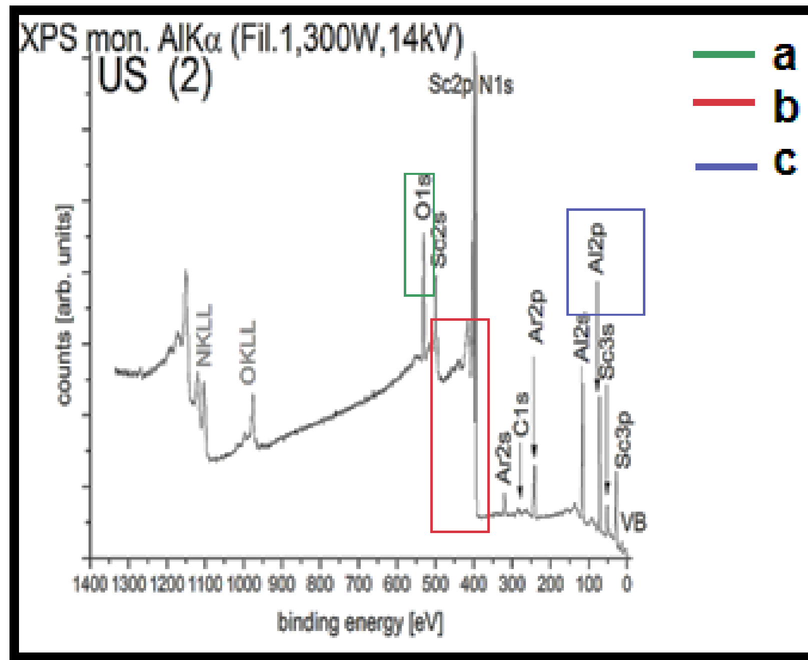

Figure IV.17: XPS overview spectrum of $Sc_{0.36}Al_{0.64}N$ after 20 minutes of sputtering.

The peaks of all elements present in the sample, along with their binding energies, are shown in the spectrum.

The two argon states, Ar 2s and Ar 2p can be viewed in this overview spectrum. They are caused by the sputtering process. Although the argon does not react chemically with the ScAlN samples, some of it is integrated into the surface during the sputtering process.

Carbon-related contaminations were almost eliminated by sputtering. After 20 minutes of sputtering, very minor traces of carbon may be recovered. They could be linked to the remaining gas in the climatic chamber, which causes some re-contamination throughout the measurement process. Despite 20 minutes of sputtering, the sample contains a large amount of oxygen (see Tab IV.4). After such a long sputtering period, finding that much oxygen could indicate oxygen inclusion during the sample's production process.

The Al2p peak and the Sc2p peak show oxygen atoms were present on the sample surface. There are two components to the Al2p peak: One component has a binding energy of 72.3 eV and is associated to Al-N (Aluminum nitride) bonds, while the other has a binding energy of 73.8 eV and is related to Al-O bonding (see Figure IV.18.c). The Sc2p core level state fitting also shows two different chemical states: Sc-N bonding, which involves the bulk of Sc surface atoms, and Sc-O bonding. The presence of Sc and Al oxide species can also be established by looking at the O1s core level state.

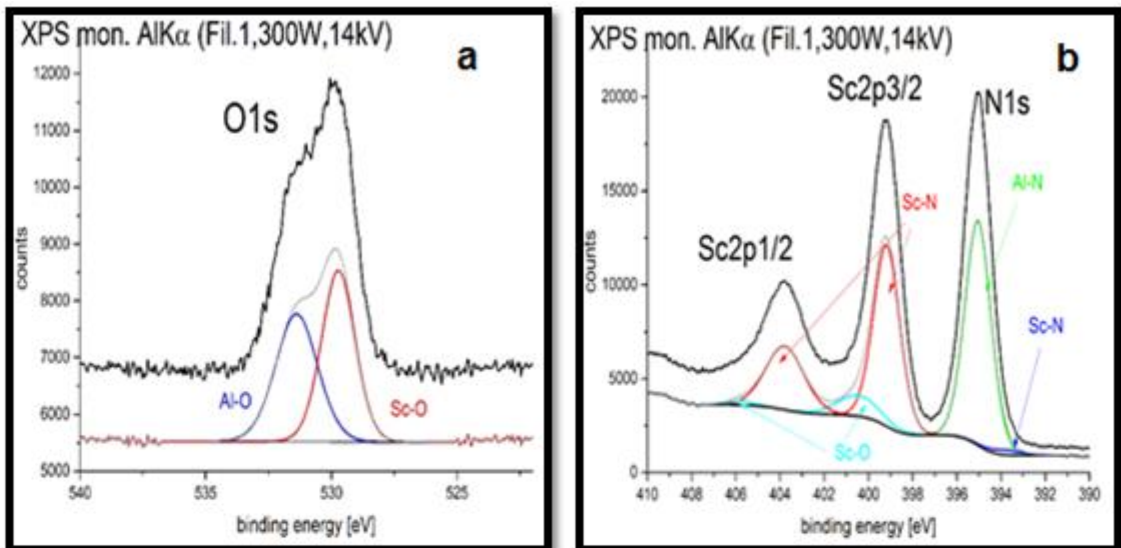

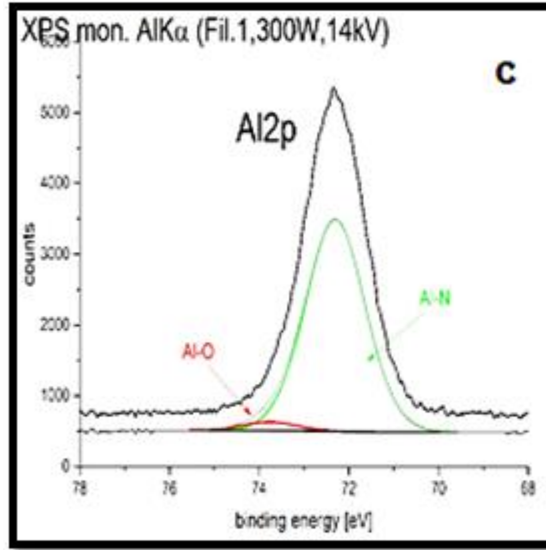

Figure IV.18: a, b, c is magnified picture of curves describing (Sc and N, Al, O)

The O1s core level state has two components: the component at 529.7 eV can be related to Sc oxide, while the component at 531.4 eV can be associated to Al oxide, based on literature regarding Al oxides and the differing electro-negativities of Sc and Al.

IV.2.2.1.3 Spectroscopic Ellipsometry

In this study, the Tauc-Lorentz model was found to be a good measuring tool for determining the layer thicknesses, refractive indices, dielectric functions, and optical characteristics [74]. V-VASE ellipsometry was used to characterize the samples shown in Table IV.2 and Figure IV.19.

To achieve the best results, we must first calibrate the machine by setting the polarizer and analyzer to the sample axis using the standard sample before each measurement cycle. After that, we must maximize the signal to get the best results.

Finally, a unique software WVASE 32, J.A. Woollam program was used to regulate the outcomes (*n* and *k*).

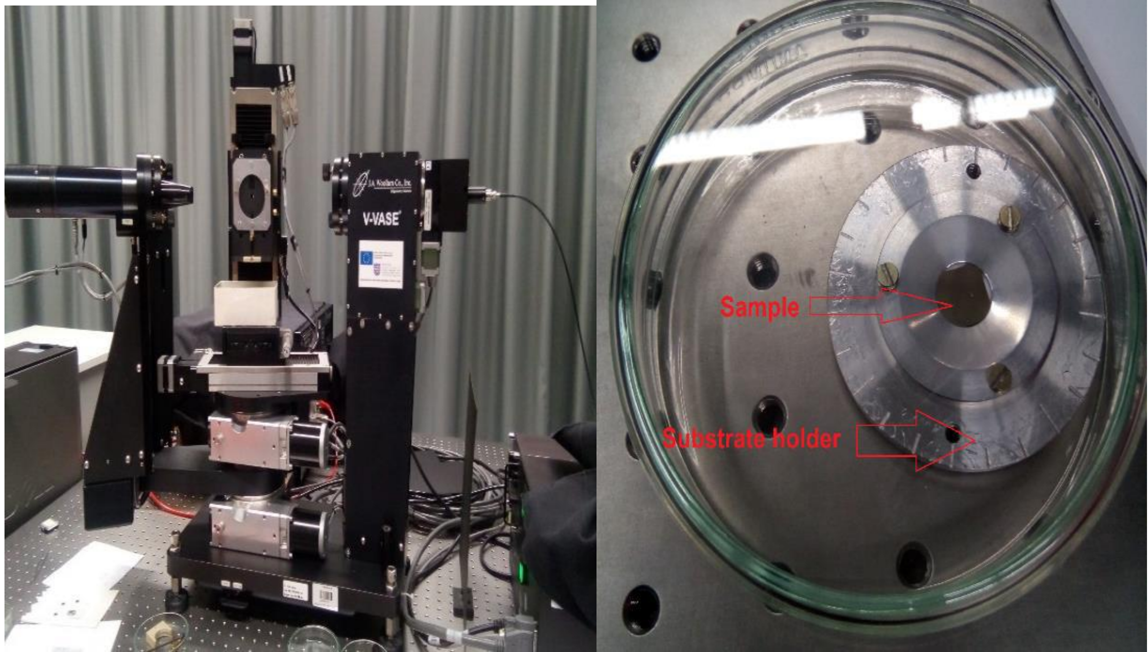

Figure IV.19: Spectroscopic ellipsometry

We used Cauchy oscillator to model the refractive index *n (λ)* and the absorption *k (λ)*.

samples	d [nm]	A	B [10^{-3}µm^{-2}]	C [10^{-3}µm^{-4}]	AK [10^{-3}]	BK [µm^{-1}]
1	207.4±0.5	2.020±0.004	8.8±0.6	9.7±0.5	0.01±0.02	5.1±1.7
2	206.5±0.8	2.051±0.003	13.1±0.4	6.4±0.3	0.07±0.06	4.0±0.6
3	167.7±0.5	2.087±0.004	9.6±0.7	12.2±0.5	0.18±0.09	3.8±0.4
4	161.1±0.4	2.132±0.004	11.4±0.7	15.7±0.5	0.82±0.17	3.3±0.2

5	157.5±0.4	2.180±0.005	9.9±0.8	22.1±0.6	2.19±0.32	2.9±0.1
6	164.0±0.4	2.242±0.005	30.2±1.2	22.0±1.1	28.35±0.08	1.78±0.04

Table IV.5: Layer thicknesses and Cauchy parameters of $Sc_xAl_{1-x}N$ layer.

Where:

$$n\,(\lambda) = A + \frac{B}{\lambda^2} + \frac{C}{\lambda^4} \qquad (IV-2)$$

$$K\,(\lambda) = Ak.exp\left[12400.Bk\,.\left(\frac{1}{\lambda} - \frac{1}{\gamma}\right)\right] \qquad (IV-3)$$

A, *B*, and *C* are the refractive indexes.

Ak and *Bk* are the absorption coefficient amplitudes and characterize the material's band gap.

$Sc_xAl_{1-x}N$ behaves similarly to AlN and is well described by the Cauchy model, which was the first assumption in this study.

We used equation (IV-3) to obtain the curves that are shown in the Figure (IV.21)

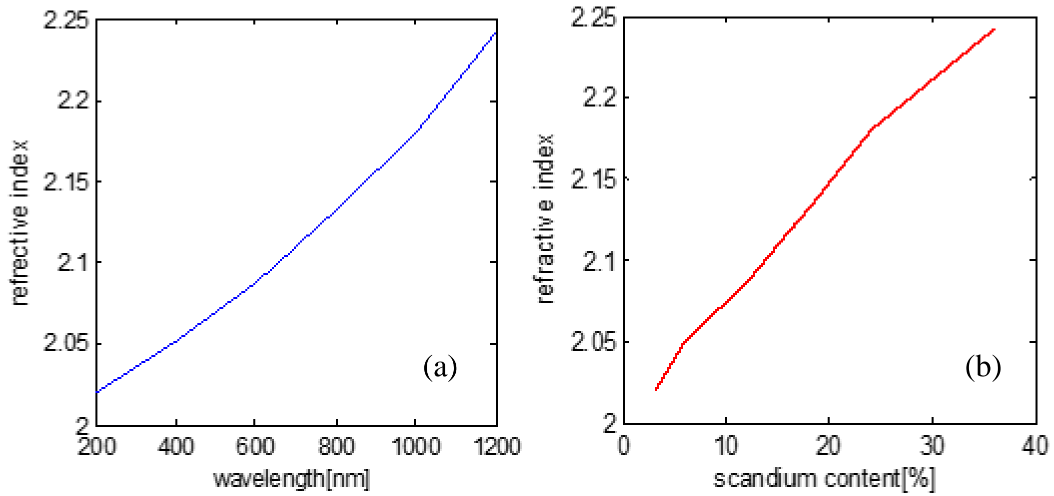

Figure IV.20: The relation between refractive index and wavelength(a), and scandium content(b).

Because the index decreases toward shorter wavelengths, ScAlN has anomalous dispersion, which is unusual for a transparent material (AlN).

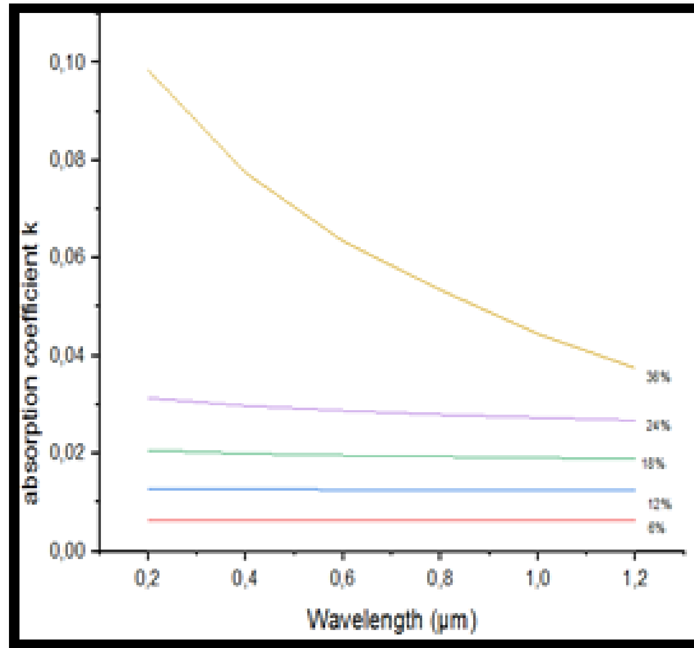

Figure IV.21: Absorption coefficient of ScAlN

Scandium content is proportional to refractive index and inversely proportional to bandgap, implying that scandium aluminum nitride is opaque.

Increased absorption with increasing Sc concentration due to a decrease in the band gap and higher absorption in the ultraviolet area is what UV-Vis spectroscopy has discovered and proven.

According to the formulae and curves, the absorption coefficient k is less than the reflecting index n, indicating that ScAlN layers are dielectric, allowing them to be employed in semiconductor devices and microelectronic applications.

IV.2.2.1.4 X-Ray Diffraction (XRD)

The detector in the machine shown below measures the intensity scattered at angle 2θ and was used to characterize the samples of the second group.

A sample holder is put on a goniometer circle to ensure that the sample is in the center, with respect to the incident x-ray and the detector.

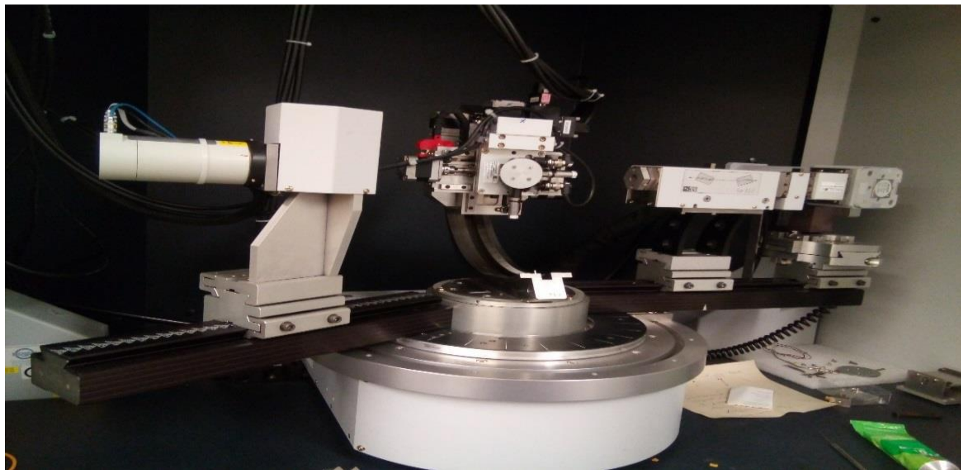

Figure IV.22: X-Ray Diffraction machine

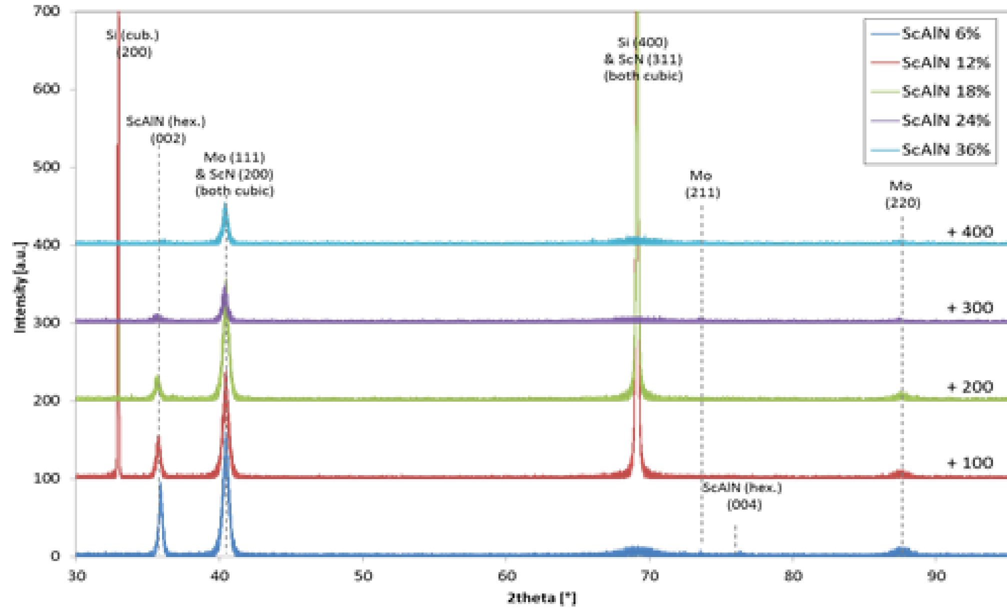

Figure IV.23: The X-ray diffractograms of the ScAlN thin films.

The atomic position in the crystal is represented by intensity. The structure is represented by 2theta (Bravais).

The symmetric reflexes (002), (004), and (005) could be used to derive the lattice constant c. Silicon's peak (200) is quite narrow (high intensity), indicating that it is a flawless crystal. Scandium aluminum nitride (002) is the dominant reflection, and the intensity of the ScAlN (0 0 2) orientated peak diminishes as scandium content increases, indicating that the c-axis crystallite size grows. Simultaneously, the c-axis orientation of the crystallites approaches the sample normal. Due to the thin film's continual growth, a perfect alignment of the c-axis crystallites toward the film surface has been achieved.

In contrast to a growing lattice constant c suggesting substantial film stress, the film is moved towards bigger angles, implying a smaller lattice constant.

The lattice constant can be calculated using this diagram:

$$c = \frac{\lambda}{\sin\left(\frac{2\theta}{2}\right)} \qquad (\text{IV} - 4)$$

λ = 1.5406 nm is the wavelength of the X-ray (Cu K alpha).

2θ is the angle of the X-ray reflection peak of ScAlN (002) in the first diagram.

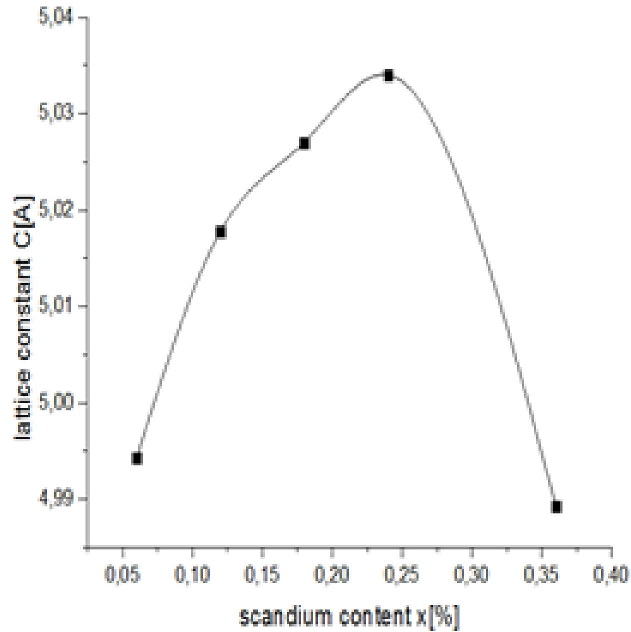

Figure IV.24: Lattice constant of ScAlN.

Because ScAlN has a hexagonal structure (scandium content less than 24 percent), the lattice constant climbs to a maximum of 5.034[Å] before falling, implying that when scandium content exceeds 24 percent, the structure turns cubic (transition in the crystal system).

IV.2.3 Third Group

The third group [Evatec AG, Switzerland] sputtered different ScAlN layers on silicon at 300 degrees Celsius. Platinum and titanium with a total thickness of roughly 100 nm are sandwiched between the layer and the substrate. Scanning electron microscopy (SEM) was used to determine the layer thicknesses of these samples, and X-ray spectroscopy was used to determine the scandium concentrations; the results are listed in Table IV.6.

Samples	Scandium content [%]	Thickness [nm]
1	14.4	918
2	10.7	994
3	7.5	990
4	4.2	997
5	1.6	1096
6	20.8	1052
7	25	1050
8	0	1064
9	25.1	1019
10	20.3	1030

Table IV.6: Layer thicknesses and concentrations of Scandium in ScAlN samples.

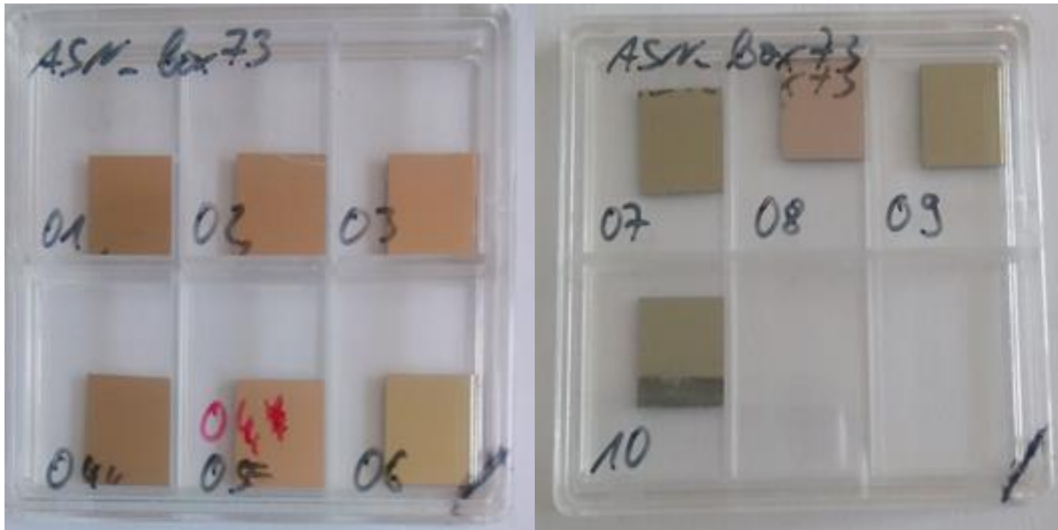

Figure IV.25: The samples of the third group

IV.2.3.1 Spectroscopic Characterization Techniques of the Third Group

IV.2.3.1.1 Spectroscopic Ellipsometry

At ambient temperature, ellipsometry measurements of ScAlN were made in the wavelength range of 200–1240 nm (energy range 1–6.2 eV) at angles of incidence of 65°,75°,70°.

Following characterization, we obtained these curves of and at various incidence angles based on photon energy.

For varying scandium concentrations, we only chose the curves of sample 8, 9, 2.

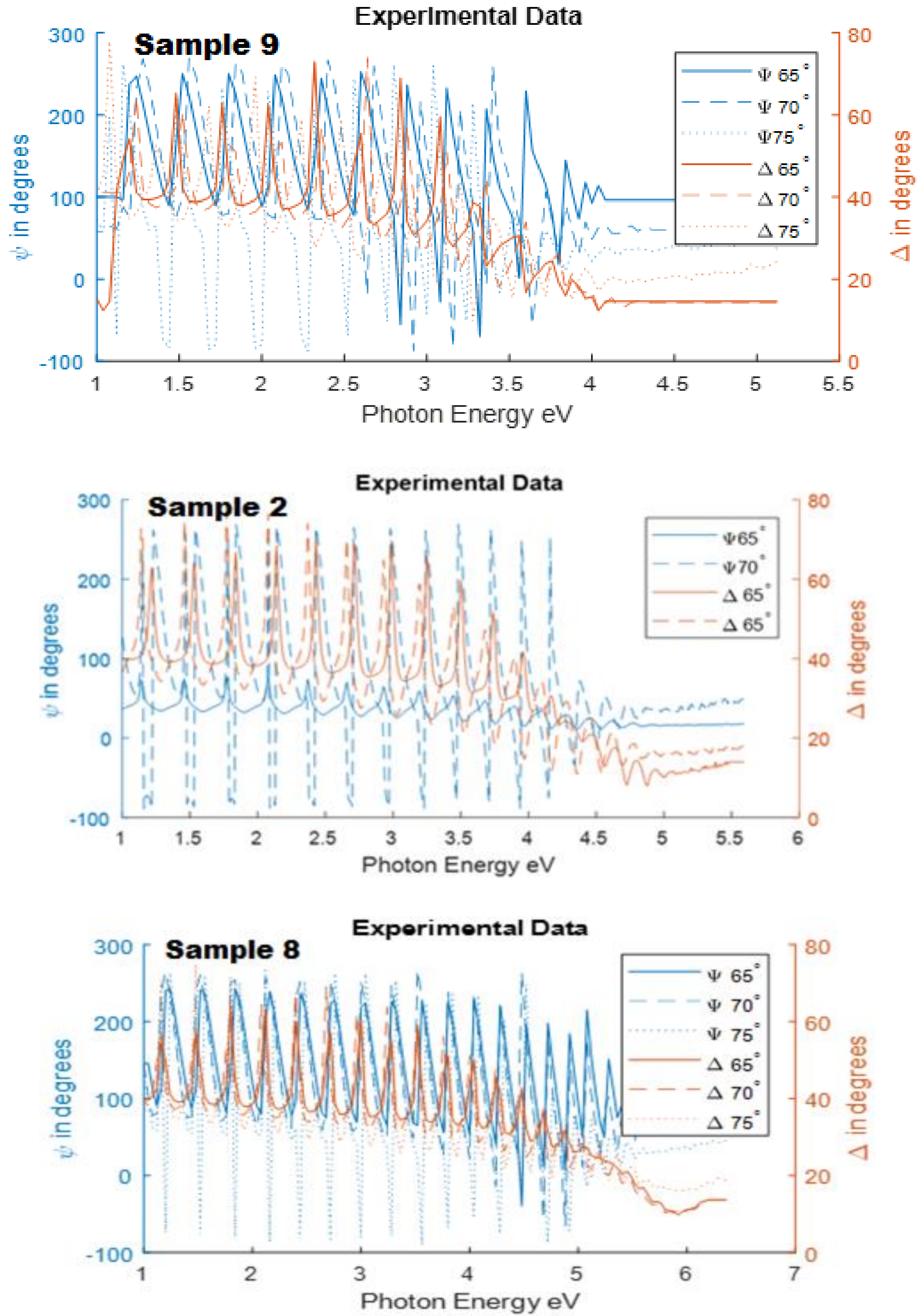

Figure IV.26: Spectral magnitude (Ψ) and phase (Δ) measured by ellipsometry at 75°, 70°, 65° on different samples.

Depending on the photon energy, we see a pseudo-periodic change in ellipsometry spectra. Interferences caused by reflections at the two interfaces (Air/thin film/substrate) account for this variance. It is worth noting that as the film thickness grows, so does the number of oscillations.

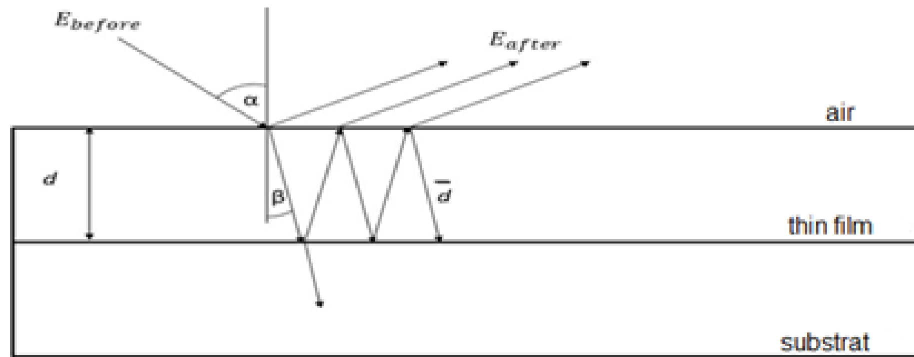

Figure IV.27: Air /thin film/substrate multiple wave interference.

The oscillation decreases with increasing energy in the UV region (> 3.5 eV), which is owing to the optical path difference being highly superior to the wavelength.

IV.2.3.2 Effective Medium Theory (EMT)

IV.2.3.2.1 Introduction

There has been a lot of interest in computing the optical properties of composite materials like ScAlN for a long time, partially because of their technical uses (microelectronic and electronic). Many studies in these sectors have focused on equations for the frequency-dependent effective permittivity (epsilon) of two components (scandium and aluminum) [83]. Optical qualities are modelled using a variety of theories, including 'rice theory,' finite-element, and effective medium.

The numerical technique of finite-element methods (FEM) is used to obtain approximate solutions to partial differential equations. The linear Maxwell's equations in the frequency domain are directly used in optical FEM. The goal of FEM is to calculate both the amplitude and phase information of the dispersed field from random rough surfaces, which can be directly compared to ellipsometry measurements and EMA (Effective Media Approximation) calculations [84, 85]. To determine optical quantities of multi-layer

systems with boundaries, Rayleigh-Rice theory is applied. This method is precise in the sense that it considers the propagation of perturbed electromagnetic fields (waves) across randomly rough barriers, considering all cross-correlation and auto-correlation effects [86]. EMA is significantly easier to understand mathematically than other theories. That is why we chose to work on this study utilizing EMA, which is best suited for ellipsometry spectroscopy [87].

Effective medium approximation models are a theoretical method of determining the optical constant of a component or a material if the latter is a mixture of two or three materials with known optical constants, volume fractions, and shape [88]. Only particles significantly smaller than the wavelength of the incoming light are suitable for EMA. Because the incident light is in the mid-infrared range (> 6 m) and the average size of the AlN particles should be in the nanometer scale, this criterion is met [85]. Further, Physical vapor deposition thin films typically have voids, flaws, and surface roughness of a few nanometers. Depending on the process of deposition, some materials have a range of optical constants. In addition, there is a layer made partially of substrate and partially of deposited material with a thickness in the order of the surface roughness. Any model used to estimate ellipsometry data must account for these effects. Effective medium approximations (EMA) have been effectively applied to ellipsometry models to quantify the influence of inclusions of a specific material within a host medium. The Maxwell-Garnet [89] effective medium theories are the two most often employed. This theory's applicability to ultrathin films will be examined further down: The effective dielectric function is then given by the well-known Maxwell Garnett formula.

$$< \mathrm{D} > = \varepsilon_{eff} \mathrm{E} \qquad (\mathrm{IV}-5)$$

$$\varepsilon_{eff} = f\varepsilon_a + (1-f)\varepsilon_b \qquad (IV-6)$$

$$\varepsilon_{eff} = \frac{< D >}{< E >} = \varepsilon_a + f(\varepsilon_a + \varepsilon_b)\frac{3\varepsilon_a}{\varepsilon_b + 2\varepsilon_a - f(\varepsilon_b - \varepsilon_a)} \qquad (IV-7)$$

Where: ε_{eff}; approximate effective permittivity

E: the electric field [V/m]

D: the electric displacement (flux density) [As/m^2]

ε_a, ε_b effective permittivity of AlN and Sc

f: volume fraction (ratio)

A simplified microscopic model, with the polarization of components represented by point dipoles, can be used to treat mixtures in an educational way [90].

Maxwell-Garnett: Different approximations to a generalized transport theory of composite systems can be obtained as Maxwell-Garnett theory (MGT). The Maxwell-Garnett relation links the effective medium permittivity(ε_{eff}), with the geometric and material parameters of a unit-cell with a spherical dielectric inclusion [91, 92].

Bruggeman: The Bruggeman coordination technique triggers a specific blending rule and provides for a more accurate assessment of the electrical reaction when the circular filler content is higher. The overall dielectric constant can be determined using a consideration-based model in which the medium is viewed as a network with haphazardly fused round incorporations, according to the Bruggeman hypothesis. The dielectric constant and volume division of the lattice and fillers were treated as independent of the state of the filler or accumulation in this model when the dielectric constant of the composite was determined [93]. The matrix and inclusion materials are not distinguished in this hypothesis [94].

Lorentz-Lorenz: the Lorentz-Lorenz model, which was previously solely used to simulate roughness in single-wavelength applications, only forecasts the spectrum dependency qualitatively and produces unsatisfactory results. [95].

IV.2.3.2.2 Implementation of EMA in Determination of ScAlN Dielectric Function

We needed the permittivity of both scandium and aluminum nitride to use the effective medium approximation [98]. The values for epsilon in aluminum nitride were obtained

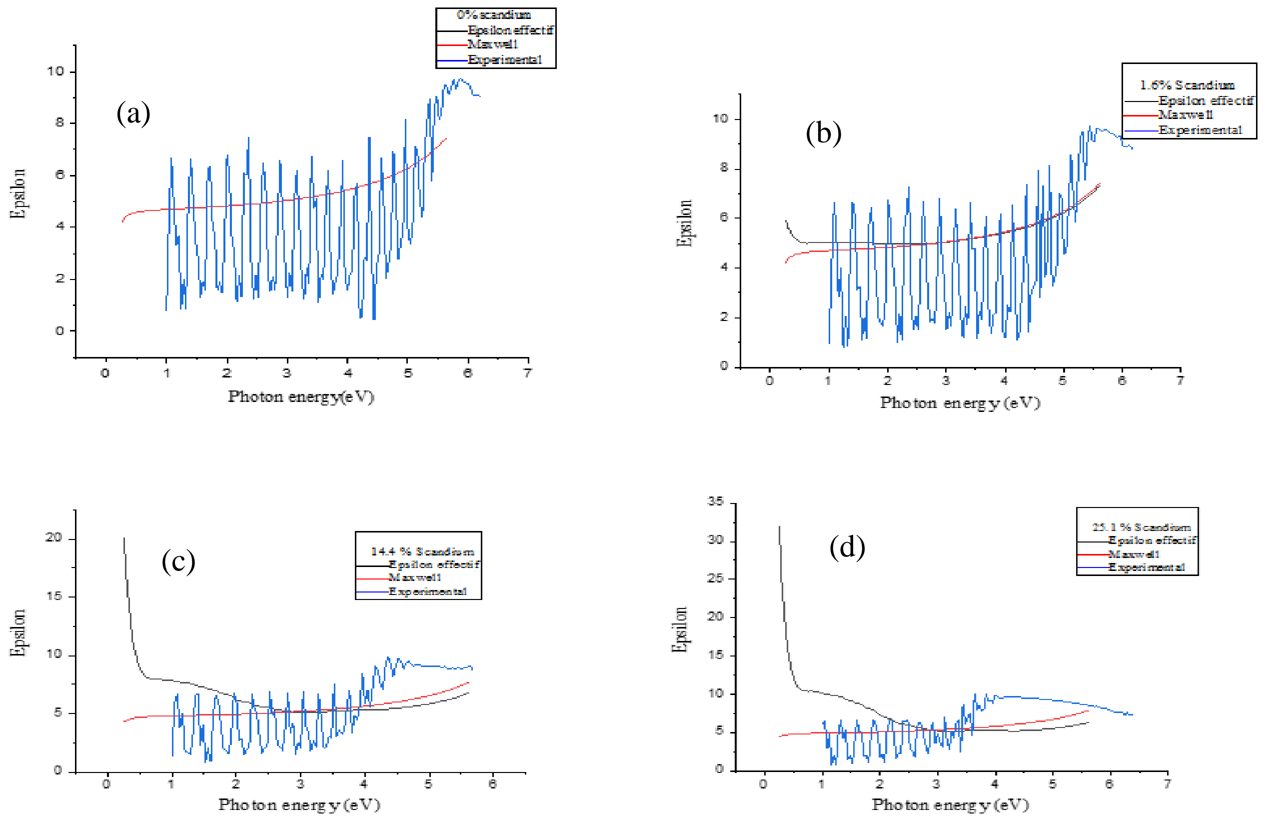

Figure IV.28: a, b, c, d are Epsilon effective, Maxwell and experimental results vs photon energy of Scandium Aluminum nitride with Scandium ratio of 0%, 1.6%, 14.4% and 25.1%, respectively.

from (Sigrist, M... (1987) Review [96]. In (Pastrnak,' J., & oskovcova,' L. 1966) [97], the epsilon values of Scandium are retrieved from the curves of epsilon real and Epsilon Imaginary. We used a plot digitizer to extract numerical values from the image in the reference presenting the curves. It transforms analogical two-dimensional graphs into numerical values (excel files). The EMA was then used to determine the final values of epsilon for various scandium over aluminum nitride alloy ratios by introducing the equation and variables into MATLAB 2018 [98]. The variations of epsilon as a function of energy, experimental, Maxwell Garnet, and effective medium approximation are represented by the blue, red, and black graphs above, respectively. We chose the four curves that stick out the most among the ten:

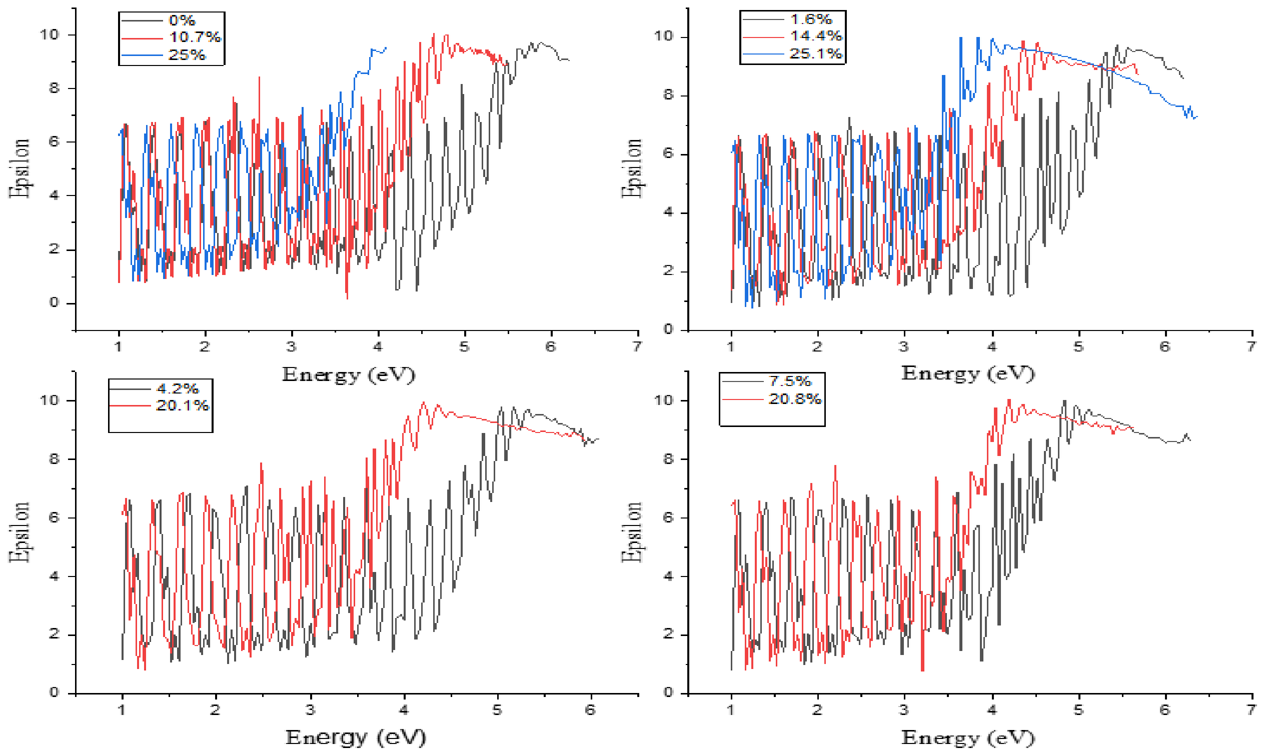

Figure IV.29: Experimental results of all samples 0% to 25.1% scandium vs photon energy.

The rise in effective epsilon values corresponds to the rise in scandium ratio. Furthermore, as compared to the epsilon experimental, the Maxwell Garnet and effective epsilon curves show slight variation. The curves, on the other hand, reveal that the effective epsilon in high scandium concentration samples has different values from the experimental data, particularly in the low energy regions. However, The Maxwell Garnet results are almost identical to the experimental results. We investigate the experimental results to differentiate how the scandium on aluminum nitride ratio affects the permittivity of the samples. The epitaxial growth of ScAlN was secured as a planning layer because of the samples being multilayers with platinum and titanium and the deposition being co-sputtering, generating multiple wave interference that explains the oscillation shown in the ellipsometry spectroscopy measurements [99]. Based on the photon energy, these findings revealed a pseudo-periodic variation in ellipsometry spectra. Interferences caused by reflections at the two interfaces of Air/ thin film/ substrate, account for this variation. The number of oscillations grows as the film thickness increases, and the scandium ratio

impacts the refractive index, which has a direct relationship with the interference that occurs, therefore the oscillation frequency is inversely proportional to the scandium ratio. Despite the increase in the scandium over aluminum ratio, there is little to no variation in the permittivity value between 1 eV and 4 eV. On the other hand, it rises gradually as the scandium ratio rises until it reaches about 15%, after which it begins to fall. That can be explained by the results provided by the curve of variation of c (lattice parameter), which is proportionally linked to epsilon. The variation in the lattice parameter makes the material extremely functional in the Ultraviolet region, which is why the epsilon variation was varied in the 5eV range.

IV.2.4 Fourth Group

The following data is presented in Figure II.34 and Table II.8 for the fourth group. Our samples were kept in a glass box with separations, with information about the sample written on top of the slot corresponding to the sample position (Figure II.34.a).

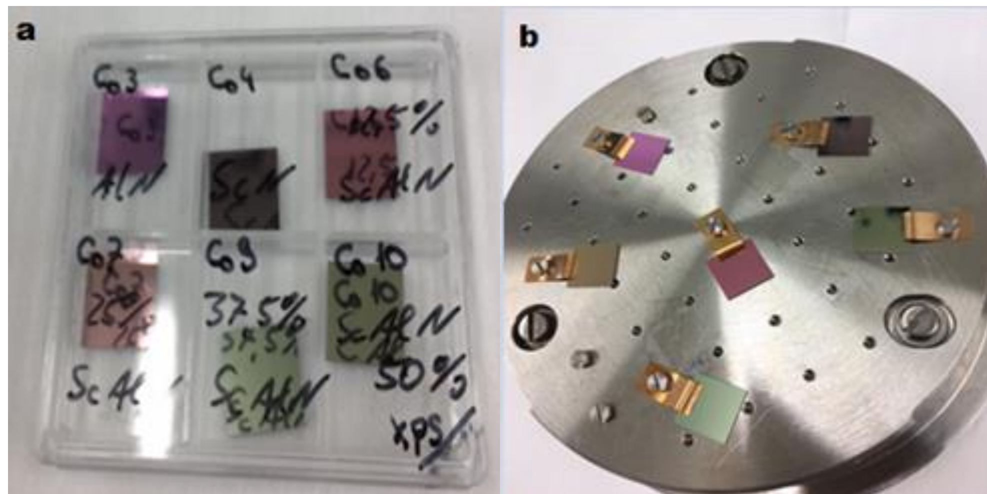

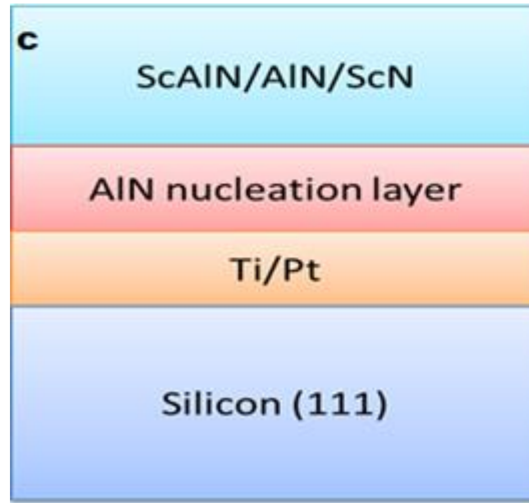

Figure IV.30: (a) ScAlN in transparent box, (b) ScAlN samples on the substrate holder, (c) the components of the sample ScAlN.

			Sputter power [%]	
samples	Sc/Al ratio [%]	1-x	Al	Sc
Co 3	0	100	100	0
Co 4	100	0	0	100
Co 6	34.77	65.22	50	50
Co 7	18.031	81.968	62.5	37.5
Co 9	2.035	97.964	87.5	12.5
Co 10	6.748	93.251	75	25

Table IV.7: Scandium and aluminum content in the ScAlN (scandium aluminum nitride) samples.

IV.2.4.1 Spectroscopic Characterization Techniques of the Fourth Group

IV.2.4.1.1 Fourier Transform Infrared Spectroscopy (FTIR)

The Bio-Rad FTS 3000 spectrometer was used to characterize the samples from the last group (Fig II.34). The samples were measured between 200 and 4000 1/cm at a 4.69° incidence angle. Two parabolic mirrors surround the chuck in the probe chamber. The IR light is guided and focused on the sample in the middle, covering the entire sample surface. The samples' IR reflectance was measured. Because the layers are essentially transparent to IR light, the spectra display a transmission behavior rather than a usual reflectance behavior, with the absorbed light indicating the position of the phonons. Due to many total reflections along the propagation path of the light, all spectra are absorption-like.

Figure IV.31: Bio-Rad FTS 3000 spectrometer.

The peaks of the spectra were modified using Origin for this. The peaks' wavenumber values are in good agreement with those found in the literature. There is just a tiny divergence with the experimental data acquired here, except for the E2low oscillation, which has lower wavenumbers depending on the mode. These phenomena can be explained as a small stress in the AlN (Aluminum nitride) layer (see Figure IV.33).

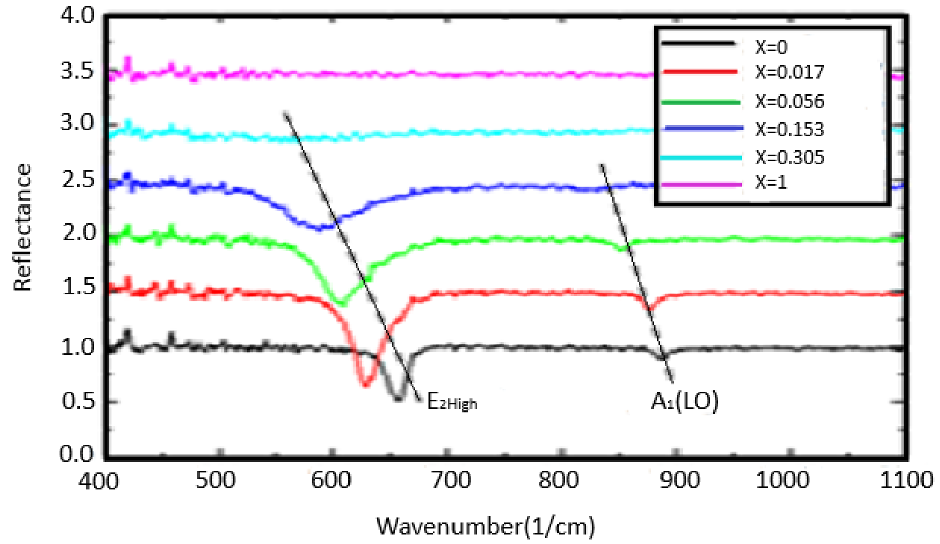

Figure IVV.32: Determination of the peak positions on the wavenumber as a function of the scandium content x in $Sc_xAl_{1-x}N$.

The peak position of the E2high phonons drops linearly as the scandium content x in the samples increases, and the E2high mode's course has a steeper slope.

This shift in frequency corresponds to a weakening of the binding caused by the substitution of scandium for aluminum.

Samples	**Sc content**	**Photon wave**	**FWHM**	**Photon wave**	**FWHM**	**Photon wave**	**FWHM**	**FWHM XR**
	%	1/cm	1/cm	1/cm	1/cm	1/cm	1/cm	°
		E_2^{high}	E_2^{high}	E_2^{high}	E_2^{high}	A_1(LO)	A_1(LO)	--
Co03	0	--	--	654.35339	19.30414	886.86014	11.93454	2.0094
Co09	1.7	628.33736	--	653.5729	19.38409	877.03508	15.309-67	1.6302
Co10	5.6	605.97344	--	647.46107	45.48176	850.34506	14.20367	1.6325
Co07	15.3	586.13034	--	655.72015	68.86951	822.32831	39.37961	1.7591
Co0-6	30.5	561.39379	--	--	--	792.0065	153.422	4.2237

Co04	100	250.52733	16.02057	--	--	--	--	2.3238

Table IVV.8: Comparison of the peak positions k of the vibrational modes E2high and A1 (LO) from Infrared Spectroscopy in [1/cm]

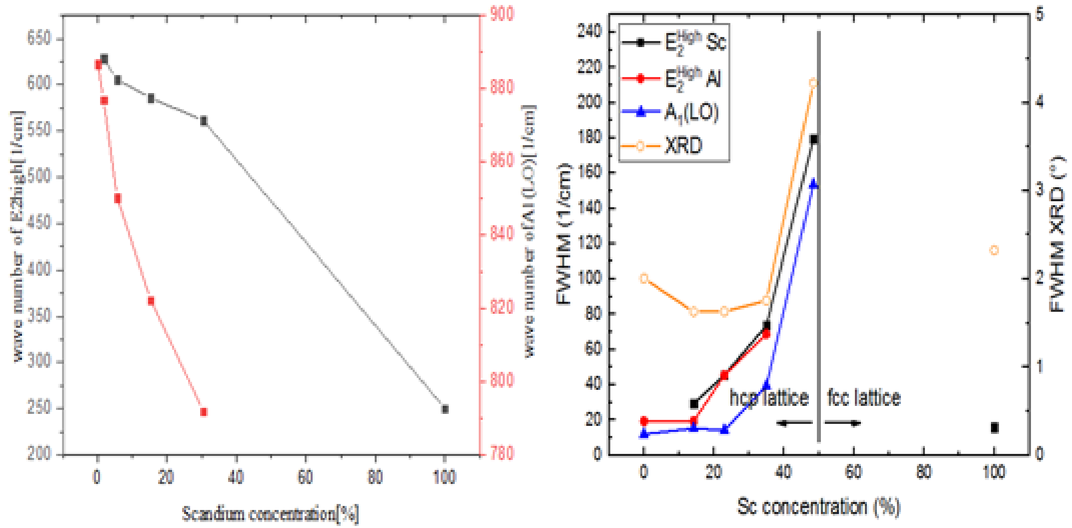

Figure IV.33: Graphical representation of the values in the Table III.8 for comparing the phonon positions of E_2^{high} and A_1 (LO)

The peak lengths of the phonons in the A1 (LO) and E2 bands from infrared spectra above the scandium concentration x demonstrate a correlation with the lattice constant's course. The distance between these modes changes due to changes in electrostatic forces, caused by polarity in the crystal system, and consequently impacts the size of the lattice parameter.

Over the half-widths of the decline in the quality of the crystal lattice with increasing x, infrared spectroscopy gives an equivalent to XRD.

- The (LO) modes have a higher frequency.
- Phonons belonging to the E2 representation are nonpolar, providing information about the stresses and the crystalline quality in the layers, while those with E1 and A1 symmetry are polar mode.
- The atomic displacement in ScAlN occurs along the C axis in A1mode (one-dimensional irreducible representation).

- This is owing to a non-strict backscattering arrangement in the ScAlN layer, in addition to the allowed E2 and A1 (LO) phonons.

IV.3 Conclusion

This part of the work focused on the material side of the work, before using a material we had to confirm its properties for that we used multiple sets of samples, four to be precise each type of samples grown under different conditions, different multilayer layout layouts and different Scandium percentages. Unfortunately, it was not possible to ensure epitaxial growth since Co-Sputtering does not offer that and MBE was not available at the time. The results proved that the samples grown at 300°C were of better-quality Wurtzite c-oriented and almost monocrystalline compared to the room temperature growth. The first set of samples was used to Figure out ScAlN material model for the deposition of the top electrodes and with bottom connections. This set of samples showed good quasi-monocrystalline behavior with a roughness in the order of 10 nm under SEM these results allowed the determination of ScAlN dielectric function using SE. The other sets of sample quality were not optimal, but it allowed us also to study the effects of connection layers and find the Band gap of the material and its lattice constants. We could conclude from this chapter that ScAlN in our samples grown with co-sputtering has a hexagonal structure up to approximately 22% then the material changes to cubic or separates into ScN and AlN making any samples with too high or too low percentages probably unusable for further investigations.

V. Simulating LEDs Based on ScAlN

V.1 Introduction

ScAlN (Scandium Aluminum Nitride) semiconductors are simulated and studied for usage in optoelectronic devices. It is recommended to simulate the ScAlN parameters in a general-purpose model to improve their qualities by reducing the emitted wavelength. The General-Purpose Device Model-Gpvdm program was created with the goal of simulating thin-film devices made of a variety of materials. It is used to speed up the development of devices like these. The term "simulation" refers to a virtual computer experience (experimentation with a model). It aids in the comprehension and visualization of the structure and the optical and electrical properties. It aids in saving time and the avoidance of material loss.

There are diverse types of software (Collection of instructions that enables a user to interact with the computer), including MATLAB, AMPS, PSE AG, COMSOL, and GPVDM (General Purpose Photovoltaic Device Model). The choice of software depends on its usefulness in relation to the requirements of the component and on its availability.

The objective is to make an optical simulation on a device of a light-emitting diode (LED) based on ScAlN. This gives the distribution of photons and their density as a function of the wavelength and the thicknesses of the layers for different percentages x of scandium (Sc) ranging from 0 to 25.1% according to the experimental values provided.

V.2 Software General-Purpose Device Model-GPVDM Description

Because it was meant to replicate organic solar cells, GPVDM was previously known as OPVDM. It has now been extended to imitate various sorts of devices, such as LEDs, OFETs, and a variety of different first, second, and third generation solar cells.

The General-Purpose Photovoltaic Device Model (GPVDM) is a software that solves the Poisson equation (V-1) in 1D and in the time domain, as well as the bipolar derivatives of the diffusion equations (V-2, V-3) and the carrier continuity equations (V-4, V-5).

$$\frac{d}{dx}\varepsilon_0\varepsilon_r\frac{d\emptyset}{dx} = q(n-p) \qquad (V-1)$$

$$J_n = q\mu_c n \frac{\partial E_c}{\partial x} + qD_n \frac{\partial n}{\partial x} \qquad (V-2)$$

$$J_p = q\mu_h p \frac{\partial E_h}{\partial x} - qD_p \frac{\partial p}{\partial x} \qquad (V-3)$$

$$\frac{\partial J_n}{\partial x} = q\left(R_n - G + \frac{\partial n}{\partial t}\right) \qquad (V-4)$$

$$\frac{\partial J_p}{\partial x} = -q\left(R_p - G + \frac{\partial p}{\partial t}\right) \qquad (V-5)$$

Where ε_0, ε_r the permittivity in vacuum and the relative permittivity of the medium.

q is the elementary charge on an electron, $\emptyset$ is the voltage profile.

n, p is the concentration of free electrons and free holes.

Jn, Jp is the electron current flux density and the whole flux density.

μc, μh is the electron mobility and hole mobility.

Ec, Ev is the mobility edge of free electrons, and free holes.

Dn, Dp is the diffusion coefficient of electrons and hole.

Rn, Rp is the net recombination rate of electrons and holes.

G is the free carrier generation rate. More information on how to solve the above equation and device modeling may be found in [100-101].

GPVDM software can already model thin-film devices made of a variety of materials. It includes advanced electrical and optical models that allow for precise and predictable simulations.

GPVDM allows researchers to investigate the impact of material properties (such as mobility, energy disturbances, and doping cross sections) and recombination on device performance. All internal properties of the simulated device, including current density, charge density, current-voltage characteristic, trapped carrier distribution, and energy space, are accessible via the software's graphical interface.

LED technology, on the other hand, will only improve if we can comprehend the principles of operation of their gadgets and how they can be enhanced.

Simulation is regarded as a good technique to gather this knowledge in this scenario.

V.3 Optical Properties

The optical features have piqued our curiosity as we try to Figure out how light interacts with matter in solid state physics. Sc-AlN are semiconductors with a relatively wide band gap and intriguing optical characteristics in the near ultraviolet (UV). However, before discussing the optical properties of Sc-AlN, it is necessary to first comprehend the material's electronic structure, which is linked to the electronic band structure and allows us to analyse and comprehend the nature of the bonds that form between the various elements of this material.

V.3.1 The Dielectric Constant ε(ω)

Y. Slimi at.al. Published a paper on Sc-AlN and its dielectric constant in 2021. The influence of the element scandium on the variation of characteristics such as permittivity was investigated (epsilon). $Sc_xAl_{x-1}N$ films with x ranging from 0 to 25.1 percent are used in the research.

We can see from Figure III.1 that as Scandium concentration increases, the values of the dielectric function of $Sc_xAl_{1-x}N$ decrease at low energies and increase as E_g>3.26eV. The high functionality of the material in the UV range explains this.

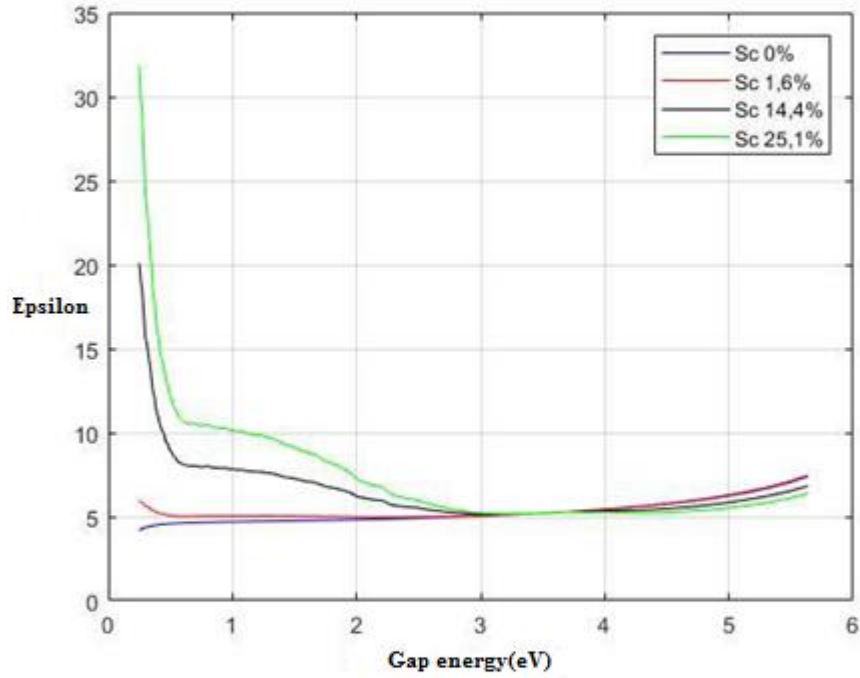

Figure V.1: Representation of the epsilon evaluation of ScAlN as a function of the gap energy for different percentage of scandium Sc = 0% 1.6% 14.4% and 25.1%.

A complicated frequency-dependent dielectric function with real and imaginary parts is used to measure a material's dielectric characteristics.

$$\varepsilon(\omega) = \varepsilon_1(\omega) + i\varepsilon_2(\omega) \qquad (V-6)$$

Where $\varepsilon_1(\omega)$ and $\varepsilon_2(\omega)$ are the real and imaginary parts of the dielectric function.

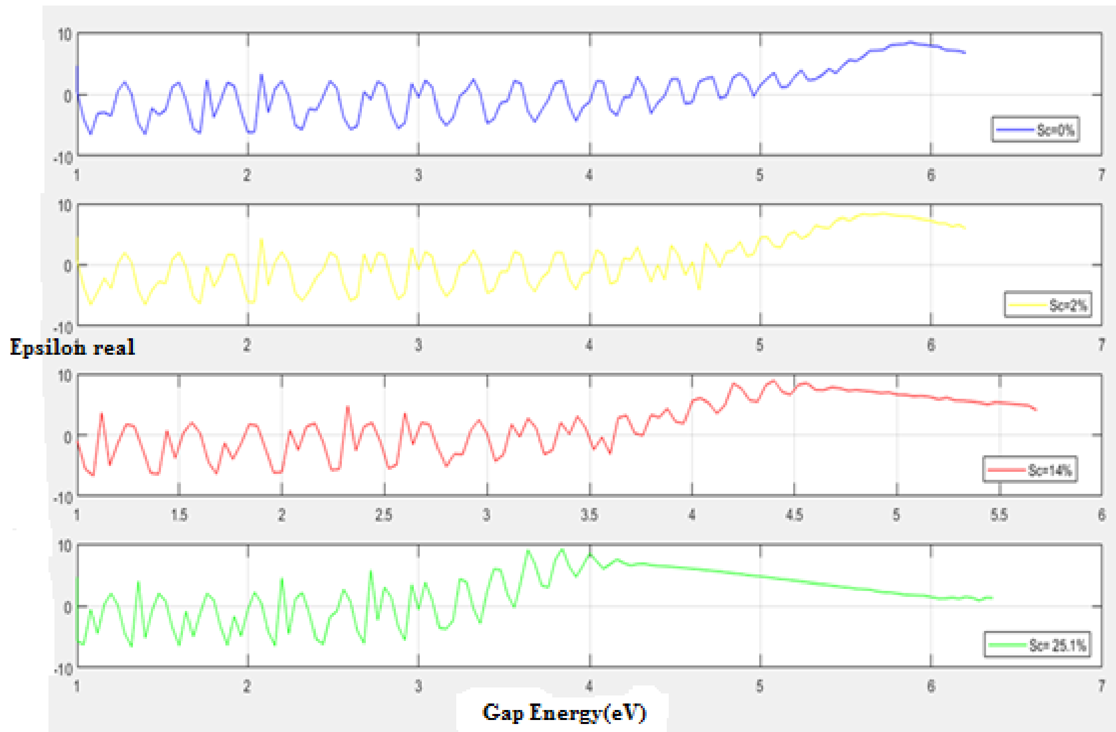

Figure V.2: Representation of the real epsilon evaluation of ScAlN as a function of the gap energy for different percentage of scandium Sc = 0% 2% 14% and 25.1%.

The following formulas can be used to calculate various optical parameters such as refractive index n, extinction coefficient k, absorption coefficient, and reflectivity R using the complex dielectric function:

$$n(w) = \frac{1}{\sqrt{2}}\left[\sqrt{\varepsilon_1{}^2(\omega)+\varepsilon_2{}^2(\omega)}\ +\varepsilon_1(\omega)\right]^{1/2} \quad (\text{V}-7)$$

$$K(w) = \frac{1}{\sqrt{2}}\left[\sqrt{\varepsilon_1{}^2(\omega)+\varepsilon_2{}^2(\omega)}\ -\varepsilon_1(\omega)\right]^{1/2} \quad (\text{V}-8)$$

$$\alpha(w) = \sqrt{2\omega}\left[\sqrt{\varepsilon_1{}^2(\omega)+\varepsilon_2{}^2(\omega)}\ -\varepsilon_1(\omega)\right]^{1/2} \quad (\text{V}-9)$$

$$R(\omega) = \frac{(n-1)^2+K^2}{(n+1)^2+K^2} \quad (\text{V}-10)$$

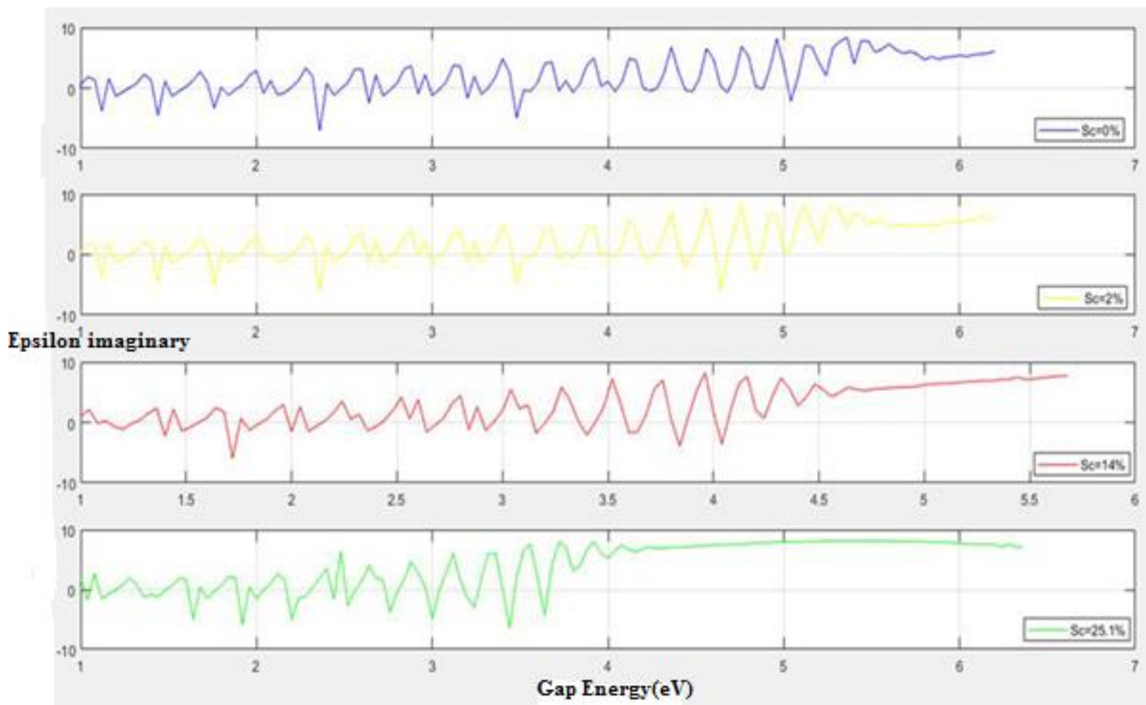

Figure V.3: Representation of the imaginary epsilon evaluation of Sc-AlN as a function of the gap energy for different percentage of scandium Sc = 0% 2% 14% and 25.1%.

V.3.2 Refractive Index n (ω)

A material's refractive index is a dimensionless parameter that characterizes it. It is regarded as a critical optical property in Sc-AlN semiconductors. The refractive index of the material must be accurately known to construct a good optoelectronic device. The refractive index of a substance is intricately linked to its electrical characteristics and band structure. The mathematical expression for the refractive index n (ω) is defined by equation (V-7) Figure (V.4) depicts the Sc-AlN alloy calculations graphically.

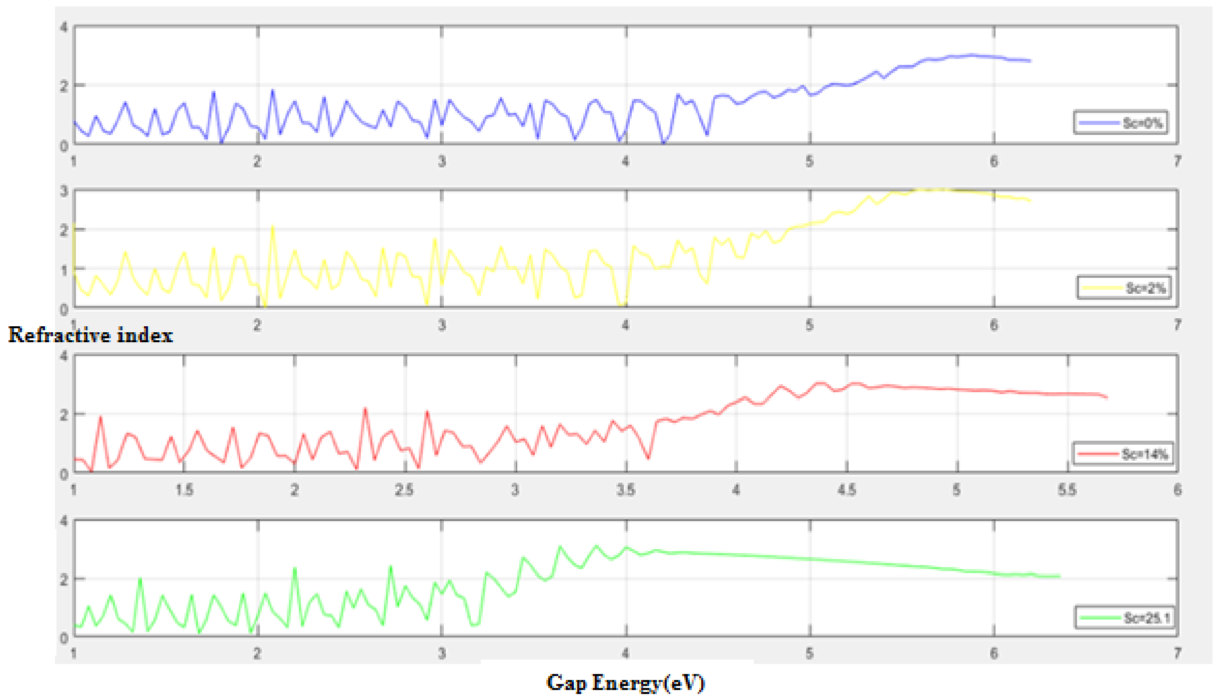

Figure V.4: The evaluation of the refractive index of Sc-AlN as a function of the gap energy for different percentage of scandium Sc = 0% 2% 14% and 25.1%.

The refractive index of Sc-AlN is proportional to the real part of the dielectric function, as shown in this diagram.

There are two distinct techniques of calculating the refractive index, both of which are theoretically correct. In the first method, it is computed based on the electrical behavior of the local fields and the material's molar volume. In the second method, a calculation is used to determine the band structure, which is then linked to the material's refractive index.

Because a semiconductor's band structure is inextricably linked to its optical behavior. Attempts to derive the refractive index using the gap energy have also been made. Several empirical relationships between the refractive index and the gap energy Eg have been proposed in this context [102-103]. In the literature, these relationships have been widely employed to determine various optoelectronic properties of various semiconductor groups. Tripathy [103] has developed an empirical relationship for calculating the semiconductor refractive index from gap energies. This relation (hereinafter referred to as the Tripathy relation) can be successfully used for a wide range of bandgaps in distinct groups of semiconductors:

$$n = n_0\left[1 + \alpha e^{-\beta E_g}\right] \qquad (V-11)$$

where n_0 =1.73, α =1.9017 and β = 0.539 eV -1, are parametric constants for a given temperature and pressure.

V.3.3 Extinction Coefficient K(ω)

The basic absorption of light exceeds the losses due to light scattering in small wavelength domains or when the gap energy is more than 3.26 eV.

If we assume that the scattering is zero, the extinction coefficient quantifies the strength of the interaction in a scattering phenomenon, and the extension coefficient equals the absorption coefficient.

We can readily obtain these two coefficients from the real and imaginary parts of the dielectric function; equations (V-8) and (V-9) explain the mathematical formulations of these coefficients; Figure (V.5) shows the extinction coefficient determined for the ScAlN alloy. The extinction coefficient of Sc-AlN is proportional to the imaginary part of the dielectric function, as shown in this diagram.

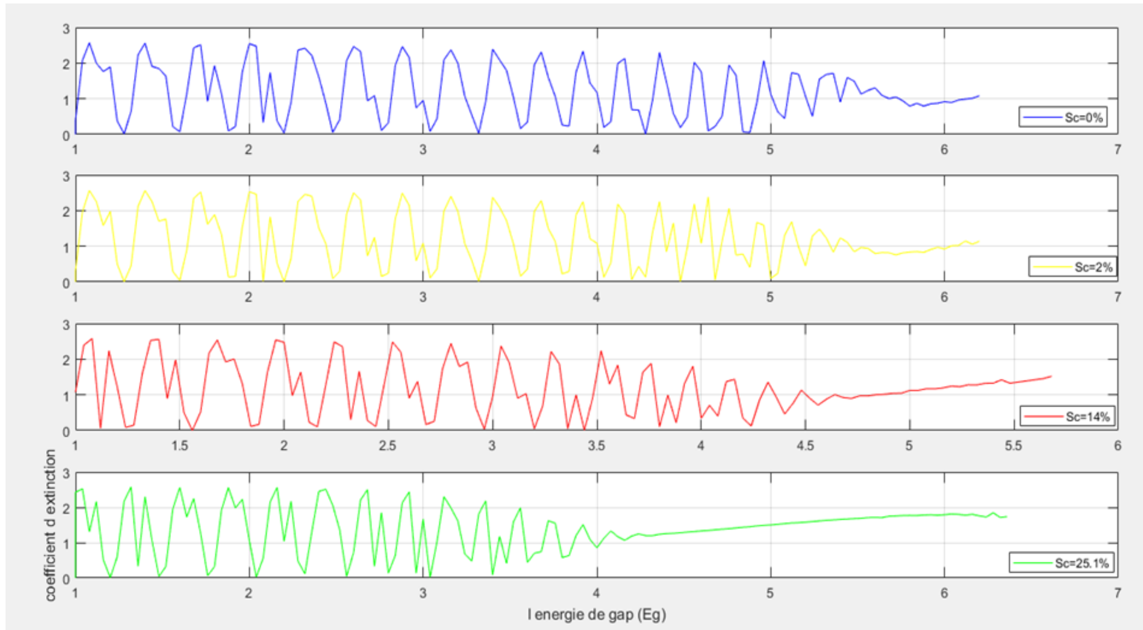

Figure V.5: The evaluation of the extinction coefficient of Sc-AlN as a function of the gap energy for different percentage of scandium Sc = 0% 2% 14% and 25.1%.

V.3.4 Reflectivity R (ω)

Reflectivity is the proportion of electromagnetic energy reflected from the surface of a material that has a certain thickness, so the reflectivity does not change with increasing thickness. The reflectivity or reflection coefficient of Sc-AlN is calculated from the refractive index n of this material using the expression (V-10) where the extinction coefficient k (ω) depends on the frequency. A small k (ω) can be assumed for weakly absorbing media. Also, k (ω) vanishes at remarkably high frequencies, i.e., k→0. In this case, the reflectivity of a material can be calculated from the high-frequency refractive index using the relationship:

$$R = \frac{(n-1)^2}{(n+1)^2} \qquad (\text{V}-12)$$

V.4 Piezoelectric properties

V.4.1 The Piezoelectric Effect

The term piezoelectricity refers to the property that some materials are electrically polarized, or generate a field or an electric potential, when subjected to mechanical stress. The brothers Jacques and Pierre Curie demonstrated in 1880 that piezoelectric materials have the unique property of generating a voltage when mechanically deformed [104], which is the phenomenon of direct piezoelectric effect. The opposing action of the electric field causes a mechanical deformation of the material, which is easily observable [105-106]. These two piezoelectric phenomena can be used interchangeably. The piezoelectric relationships can be stated mathematically as follows:

$P_i = e_{ij}k.\ Sjk$ (direct piezoelectric effect) (V-13)

$S_{ij} = d_{ji}k.\ Pk$ (inverse piezoelectric effect) (V-14)

Where P is the polarization, S the deformation tensor, e_{ij} and d_{ij} are the piezoelectric coefficients.

The dielectric displacement is indicated by the first subscript (i) while the mechanical deformation is indicated by the second subscript (j). If axis 3 is the polar axis, then axes 1 and 2 are the orthogonal axes in the plane normal to 3 [107]. The electric field and mechanical deformation are detected along the same polar axis, for example, d_{33}.

V.4.2 Electrical Properties of a Piezoelectric Material

Solid dielectrics known as piezoelectric materials are a type of solid dielectric. A dielectric material, by definition, is an insulator that does not carry electric current and, unlike metals, has no free electrons. As a result, the application of an external electric field can affect the electrical and optical properties of a dielectric substance, resulting in polarization. The charges within the material will separate, but the displacement will be finite, the induced polarization P will be parallel, and the displacement D will be proportional to the electric field E:

$$P = \varepsilon . \chi_e . E \qquad (\text{V} - 15)$$

$$D = \varepsilon . E \qquad (V-16)$$

Where χ_e is called the electric susceptibility, $\varepsilon = \varepsilon_0 (1+\chi_e)$ is the permittivity such that ε_0=8.85.10-12 F/m is the permittivity of free space, and ε/ε0 =1+ χe is called the relative dielectric constant.

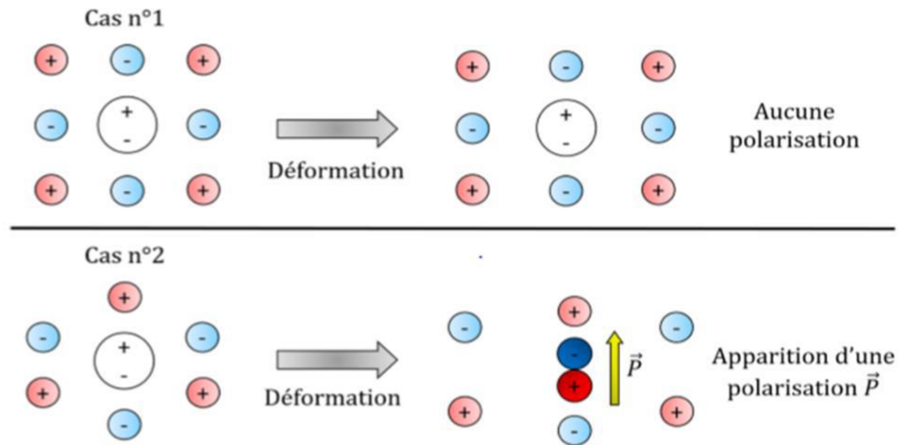

Figure V.6: Deformation of a crystal mesh: in the case n°1, the positive and negative charges remain merged: no electric polarization. In the case n°2, the charges dissociate appearance of a '*P*'.

The ability of a material to have piezoelectric qualities is determined by its crystal structure, while the piezoelectric effect itself is determined by the material. Twenty-one of the 32 crystal classes are non-Centro symmetric. Except for the 432 cubic class, all non-Centro symmetric crystal classes have been found as structures with piezoelectric capabilities. Ten of the twenty are polar crystal classifications that show polarization, such as wurtzite. This distribution is depicted in Figure V.9.

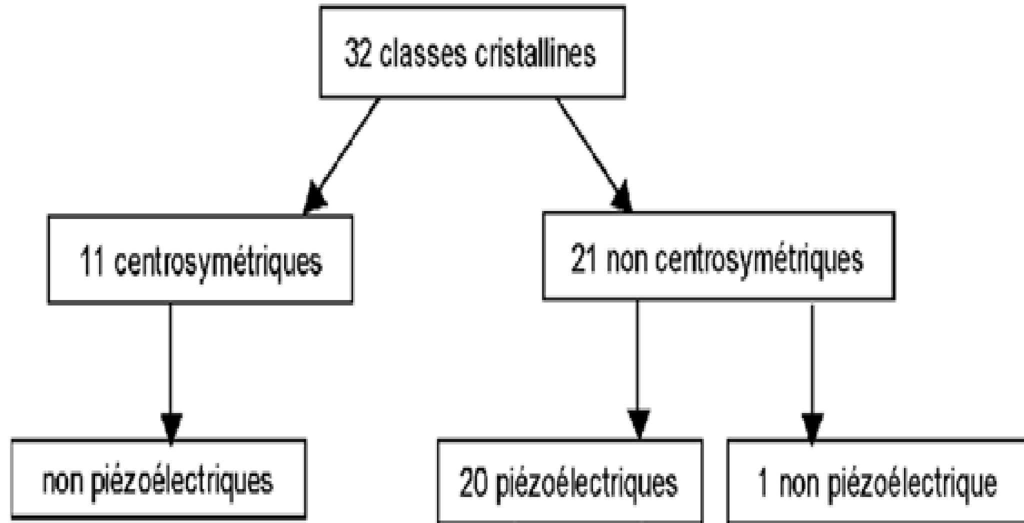

Figure V.7: Distribution of crystalline classes and their electrical owners.

Compared to other group III nitrides; we will focus on Wurtzite AlN as a piezoelectric material belonging to one of the ten classes of polar crystals that display spontaneous polarization (see Table V.1 [108]). Its piezoelectric response is the highest:

e_{33} = 1.46 C / m^2 [109] and d_{33} =5.1- 6.72 pm / V [110-111].

Table V.1: Piezoelectric coefficients of III-Nitrides alloys

x	$Al_xGa_{1-x}N$	$In_xGa_{1-x}N$	$Sc_xGa_{1-x}N$	$Sc_xAl_{1-x}N$
0	0.73	0.29	0.57	1.46
0.25	0.91	0.30	1.02	2.03
0.5	1.10	0.315	1.82	3.34

V.5 Modelling Theories of Optical Properties

The finite element technique, finite difference method, effective medium approximation, and Rayleigh-Ritz method are only a few of the approximate methods available for modelling optical properties. Differential equations, or more broadly partial differential equations, can be solved using these approaches. Figure V.8 depicts the evolution of

various simulation models for optoelectronic devices, together with their modelling approaches and essential properties.

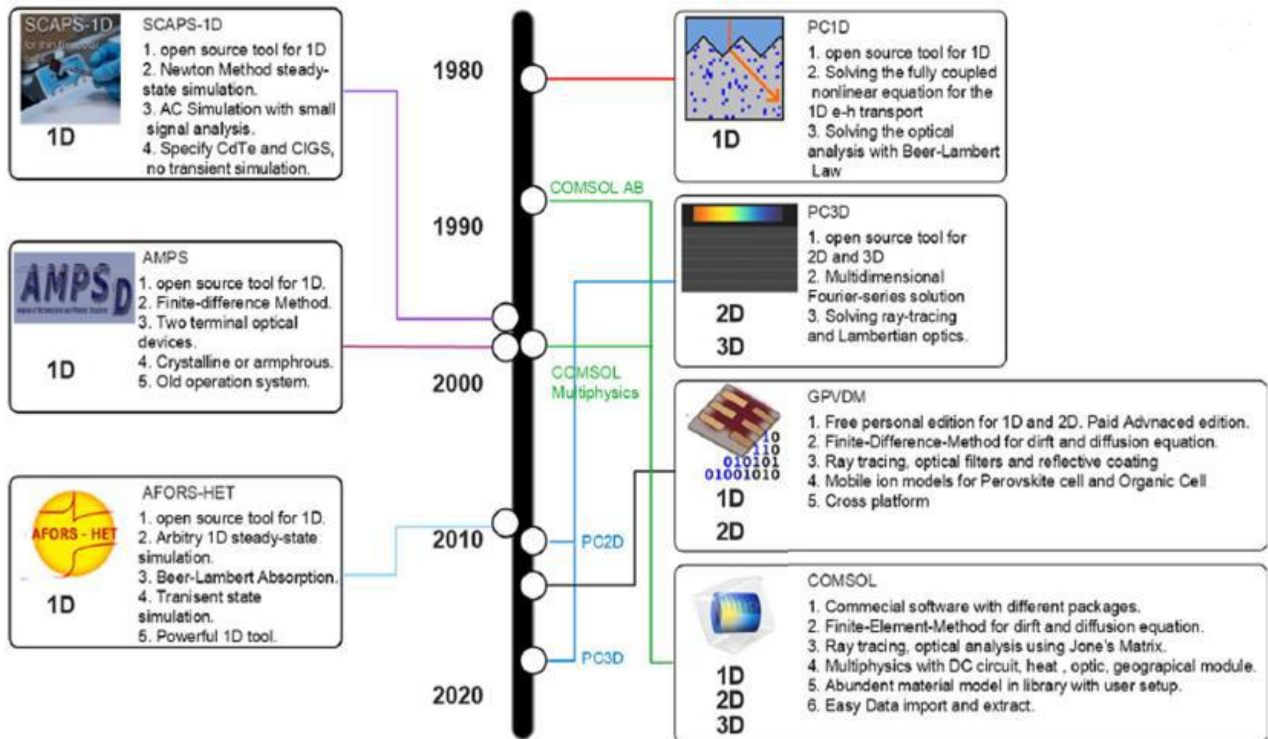

Figure V.8: Chronologies on the development of different simulation models and their numerical modelling methods for optoelectronic devices [112]

V.5.1 Finite Element Method (FEM)

The finite element method is a numerical approach for calculating approximate partial differential equation solutions (PDE). As a result, it can be used to solve a wide range of physics problems. The approach works by replacing a continuous domain with a collection of subdomains known as elements. Unknown continuous functions are represented in these elements by simple interpolation functions with unknown coefficients. The number of degrees of freedom is thus reduced to a limited number, implying that the solution of the entire system can be approximated by a finite number of unknown coefficients. After that, the answer is obtained through linearization or optimization. One of the key benefits of

FEM is that the size of the elements can vary based on the model, resulting in increased resolution and accuracy at points where it is required, such as at interfaces. Optical FEM is based on the frequency domain linear equations of Maxwell [96]. This method prefers to calculate the dispersed field's amplitude and phase data.

V.5.2 Maxwell's Equations

The behavior of electromagnetic fields and their interactions with matter are described by Maxwell's equations. We can review these equations in temporal and harmonic regimes in this section.

V.5.2.1 Maxwell's Equations in the Time Regime

E is the electric field, H is the magnetic field, D is the electric induction (or displacement), and B is the magnetic induction. Electromagnetic fields are classically described by four vector fields that depend on space r and time t: E is the electric field, H is the magnetic field, D is the electric induction (or displacement), and B is the magnetic induction. The four electromagnetic fields are related to their macroscopic sources (free charge density) and J (free current density) by Maxwell's equations, which are also dependent on space r and time t:

Maxwell Gauss

$$\nabla . D(r,t) = \rho(r,t) \qquad (\mathrm{V}-17)$$

Conservation of magnetic flux

$$\nabla . B(r,t) = 0 \qquad (\mathrm{V}-18)$$

Maxwell Ampère

$$\nabla \times H(r,t) = \frac{\partial D(r,t)}{\partial t} + J(r,t) \qquad (\mathrm{V}-19)$$

Maxwell Faraday

$$\nabla \times E(r,t) = -\frac{\partial B(r,t)}{\partial t} \qquad (\mathrm{V}-20)$$

In the presence of a macroscopic material, the fields *D (r, t)* and *H (r, t)* are related to the fields.

E (r, t) and *B (r, t)* through the constitutive relations:

$$D\ (r,t) = \ \varepsilon 0\ E\ (r,t) + \ P\ (r,t);\ P\ (r;\ t) = \ \varepsilon 0 \int dst - \infty \chi e\ (r,t-s)E\ (r,s) \qquad (V-21)$$

$$B\ (r,t) = \ \mu 0 H\ (r,t) + M\ (r,t);\ M\ (r;\ t) = \ \mu 0 \int dst - \infty \chi m\ (r,t-s)H\ (r,s) \qquad (V-22)$$

With ε_0 for vacuum permittivity and μ_0 for vacuum permeability. Through the electric susceptibility χe and χm the magnetic susceptibility m, the polarization field *P* and magnetization field *M* characterize the response of the material under investigation to the electromagnetic fields *E* and *H*. As a result, they represent the microscopic sources of the material's electromagnetic fields [113]. It is vital to remember that a material's polarization and magnetization are not instantaneous and depend on the *E* and *H* fields.

V.5.2.2 Maxwell's Equations in the Harmonic Regime

To establish Maxwell's equations in the harmonic regime (frequency), the relative dielectric permittivity $\varepsilon r\ (r,\omega)$ and relative magnetic permeability $\mu r\ (r,\omega)$ tensors must first be introduced:

$$\varepsilon r\ (r,\omega)\ = 1 + \ \int dtexp\ [-i\ \omega t]\ + \infty - \infty \chi e\ (r,t) = \ 1 + \int dt\ exp\ [-i\infty 0\omega t]\ \chi e\ (r,t) \qquad (V-23)$$

$$\mu r\ (r,\omega) = 1 + \ \int dtexp\ [-i\ \omega t] + \infty\infty - \infty \chi m\ (r,t) = \ 1 + \int dt\ exp\ [-i\infty 0\omega t]\chi m\ (r,t) \qquad (V-24)$$

Applying a time Fourier transform (dependence in $exp\ [-i\omega t]$) to the constitutive equations these become:

$$D\ (\omega;\ t) = \ \varepsilon 0\ \varepsilon r\ (r,\omega)E\ (r,\omega) \qquad (V-25)$$

$$B\ (\omega;\ t) = \ \mu 0\ \mu r\ (r,\omega)H\ (r,\omega) \qquad (V-26)$$

The tensors of relative dielectric permittivity $\varepsilon r\ (r,\omega)$and relative magnetic permeability $\mu r\ (r,\omega)$ are intrinsic properties of the material in question, and their dependency on frequency represents the material's dispersion phenomena. The harmonic Maxwell equations are generated by applying a Fourier decomposition to Maxwell's equations:

$$\nabla.[\varepsilon r\ (r,\omega)E\ (r,\omega)] = \rho\ (r,\omega) \quad (V-27)$$

$$\nabla \times H\ (r,\omega) = J\ (r,\omega) - i\omega\varepsilon 0\ \varepsilon r\ (r,\omega)E\ (r,\omega) \quad (V-28)$$

$$\nabla.[\mu r\ (r,\omega)H\ (r,\omega)] = 0 \quad (V-29)$$

$$\nabla \times E\ (r,\omega) = i\omega\mu 0\ \mu r\ (r,\omega)H\ (r,\omega) \quad (V-30)$$

Finally, in the absence of macroscopic sources (ρ(r; t) = 0 and J (r; t) = 0), these equations become:

$$\nabla.[\varepsilon r\ (r,\omega)E\ (r,\omega)] = 0 \quad (V-31)$$

$$\nabla \times H\ (r,\omega) = -i\omega\varepsilon 0\ \varepsilon r\ (r,\omega)E\ (r,\omega) \quad (V-32)$$

$$\nabla.[\mu r\ (r,\omega)H\ (r,\omega)] = 0 \quad (V-33)$$

$$\nabla \times E\ (r,\omega) = i\omega\mu 0\ \mu r\ (r,\omega)\ H\ (r,\omega) \quad (V-34)$$

V.5.3 Meshing

In several domains, the finite element approach is frequently utilized for design and simulation. The domains must be discretized into a set of elements called the mesh to use this method. The most popular shapes of elements for automatic meshing are triangles in 2D and tetrahedrons in 3D. The mesh quality in finite element approximation plays an essential influence in the correctness of the solutions [114]. A mesh containing poor elements, such as flat, long, or thin elements, might result in an ill-conditioned stiffness matrix, slowing down the solver or reducing the solution's accuracy. The number of finite elements utilized, and the fineness of the mesh are the most significant factors; the solution

will not converge if there are too few elements. On the other hand, if the mesh is too fine, the simulation will consume far more power than is required.

- ✓ The mesh can be produced in a variety of ways, but two are commonly utilized. The one with triangle pieces is unstructured, while the other has square elements [115].
- ✓ The unstructured mesh is the most important since it is generated by most FEM mesh generators and can result in irregular and complex areas. As seen in Figure (V.9), elements come in a variety of shapes, including triangles, quadrilaterals, tetrahedrons, hexahedrons, and prisms.

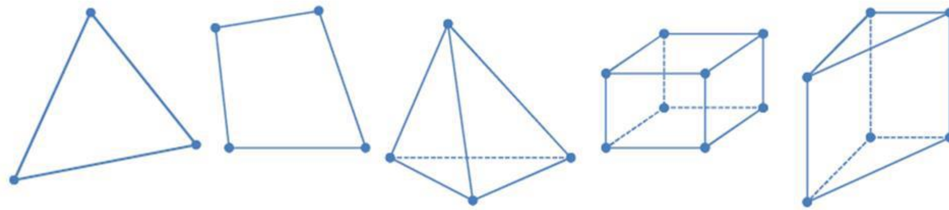

Figure V.9: Some types of mesh elements

The finite element method requires some pre-requisite validity conditions for unstructured meshes [116]:

- ❑ There must be no holes or overlaps between elements in the mesh. Furthermore, none of these elements can share two or more with another element on the edge, whether they be triangular elements in 2D or tetrahedral elements in 3D.
- ❑ The mesh must accurately depict the geometry while also respecting the geometry's edges.
- ❑ A size function that evolves in a flexible and continuous manner in the future must manage the mesh density. This function is either defined by the user or coupled to the local error estimator.
- ❑ The mesh must have high-quality elements: the best meshes have the most equilateral elements (equilateral triangles or equilateral tetrahedrons).

Three types of automatic methods can be found among the automatic methods. The first method is based on a simple decomposition that covers the domain and is then correctly updated to produce the final mesh. The leading-edge approach is used in the second type of method, whereas the Delaunay-Voronoi concept is used in the third type.

V.5.4 Grid-Based Meshing Method (Quadtree2D/Octree3d Methods)

A simple rectangular or triangular grid is employed in this method to cut out the domain, including beyond the geometry's edge. The domain's edges truncate the grid, and the intersection of the grid and those edges is relocated to form elements. After halving the rectangular element, the output is a triangular mesh. This method is easy and quick, but the quality of the components is poor, particularly the edge elements, and FEM necessitates a systematic discretization of these contours. Because it only generates features of the same size, using a regular grid has density restrictions. By providing changeable size grids, quadtrees in 2D and octrees in 3D can bypass this issue (FigureV.10). However, we should point out that this method's discretization at the edge is still a drawback. [117].

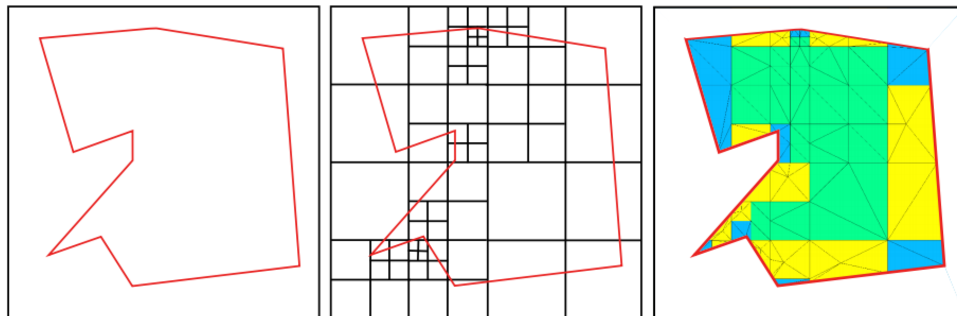

Figure V.10: Illustration of a grid (a 2D example) [116]

V.5.5 Frontal Method or Frontal Advancement

The principle of this method is as follows:

- We begin by discretizing the domain edges that make up the initial front (a collection of points that together form a mathematically closed curve or surface).

The front is presumably a curve/surface that separates the mesh able and non-mesh able parts.

- ❑ Inserting elements (triangles in 2D, tetrahedrons in 3D) in the mesh with at least one facet on the front is the next step. New pieces have been added to the front.
- ❑ In this method, generate elements until the front is empty and the grid is complete.

Figure (V.11). On a 2D domain, the mesh is shown below using front advancement.

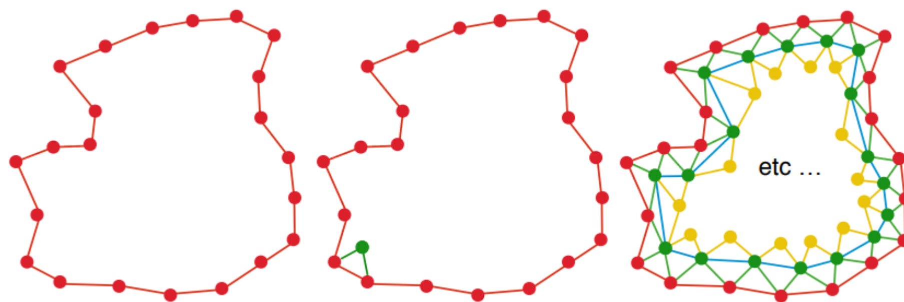

Figure V.11: Illustration of the edge advancement method [117]

Because of the laws regulating the production of additional elements, even if the method's principle is simple, the method's progression is difficult to create. To assure the convergence of the algorithm and the quality of the mesh, these criteria might be based on Delaunay's hollow circle (sphere) criterion and other conditions on the element's edge or shape [116] [118] [119]. Advancement approaches, on the other hand, typically adapt to domain and size limits. In this strategy, the initial front is quite crucial. In 3D, discretizing the domain edge surface becomes extremely sensitive and costly: if the first triangulation produces a poor beginning element, the front advancement can result in a very low-quality volume mesh.

The frontal technique has the advantage of producing a high-quality mesh, but at the cost of a complicated implementation and a high processing cost.

V.5.6 Meshing Method Based on Delaunay Triangulation

Setting up DT(P) triangles such that no point of P is inside the circumscribed circle of any of the DT(P) triangles is known as Delaunay triangulation of a set P of points in the plane [120]. The Delaunay triangulation of a set of points, to put it another way, is the triangulation that does the best job of avoiding tiny angles and insisting on the empty circle condition that there are no triangle vertices inside the dashed circles. Figure (V.12) compares the Delaunay triangulation to any other triangulation.

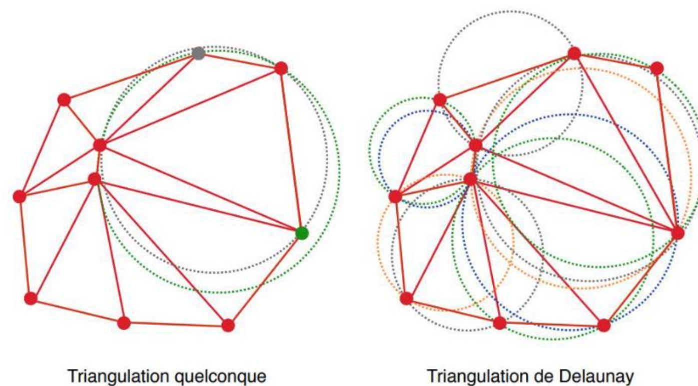

Figure V.12: Delaunay triangulation and any triangulation [120]

The Delaunay triangulation has two interesting characteristics for meshing [121]:

- There is no point inside any triangle's circumscribed circle. In 2D, this condition is known as the empty circle criterion, while in 3D, it is known as the empty sphere criterion. Several meshing algorithms exploit this criterion.
- In two dimensions, the Delaunay triangulation maximizes the least angle of all the triangle's angles. This condition is significant because it ensures that the triangulation and best mesh for a given collection of points are achieved. This "max min" property, on the other hand, is not possible in 3D and may result in undesired traits.

Delaunay triangulation of a group of points is a highly frequent meshing technique [116] [122] [123]. In practice, most meshing software today employs this method. The Delaunay

regularization and the continuous insertion of nodes interior to the domain are usually the two processes in domain meshing.

V.6 Rayleigh-Rice Theory (RRT) and Effective Media Approximation (EMA)

Most thin films appear to have flaws. Roughness and thickness non-uniformity are the two most significant flaws between them [124]. The optical characteristics of thin films are frequently influenced by the combination of these imperfections, and their neglect leads to incorrect or inaccurate optical characterization results. For the description of these optical features, several techniques based on the amplitude of the heights and the irregularity of the lateral dimensions of the roughness have been proposed. The effective medium approximation (EMA) is used to describe roughness when the lateral dimensions and heights are substantially lower than the incident light wavelength. A perturbation theory, such as the Rayleigh-Rice theory (RRT), can be utilized if the lateral dimensions of the roughness are comparable to or less than the wavelength, and the magnitudes of the heights are sufficiently smaller than the wavelength [125].

V.6.1 Rayleigh-Rice Theory (RRT)

The Rayleigh-Rice theory is a second-order perturbation theory for calculating the optical properties of multilayer systems, such as reflectance, transmittance, and ellipsometry parameters, which correspond to reflected and transmitted light. This method is accurate because it accounts for the propagation of perturbed electromagnetic fields (waves) between approximate random interfaces, as well as all inter-correlation and autocorrelation effects [126]. The vector perturbation approach to solving Maxwell's equations on rough surfaces is known as RRT. The electromagnetic field is estimated in the specular direction up to the second order of the perturbation parameter σ k0 (where σ and denote the RMS value of irregularities roughness heights and void wavenumber, respectively) [125]. The Rayleigh Rice approach simplifies analysis by reducing an infinite number of degrees of freedom in a system to a finite number.

V.6.1.1 The Effective Media Approximation (EMA)

The effective layer is defined by a thickness deff, and a complex dielectric function ε_{eff} or a complex refractive index neff in the effective medium approximation. In EMA [127], there are numerous formulas for expressing the dielectric function of this layer, although Bruggeman's formula is most used in the literature [128]. This formula can be used to derive the following equation to indicate the effective refractive index of this effective layer:

$$neff = \sqrt{\varepsilon eff} = \frac{\sqrt{\sqrt{\Omega^2 + 8n0^2n1^2} - \Omega}}{2} \qquad (V-35)$$

$$\Omega = (1-p)(n1^2 - 2n2^2) + p\,(n0^2 - 2n1^2) \qquad (V-36)$$

Where p represents the ambient refractive index (general case $n_0 = 1$), the refractive index of the material bounded by a rough surface and an effective layer density factor packing, respectively. Medium is parameterized by two effective layer parameters, d_{eff} and p, in this case.

V.7 Simulation of the Optoelectronic Device (LED)

The graphical interface of the GPVDM simulator makes it easy to use. It is sufficient to manipulate the icon (NEW SIMULATION) as shown in Figure III.13 to generate a structure model and run a simulation.

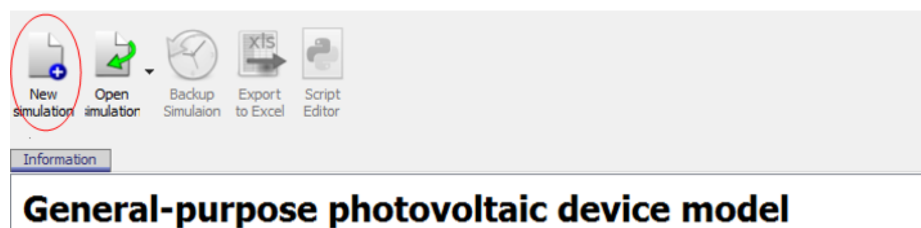

Figure V.13: welcome window of GPVDM.

The second step is to select the model to mimic it as well as the type of optoelectronic device from the options presented below:

- LEDs
- Organic solar cells

- Perovskite solar cells
- OFET (Organic Field Effect Transistors)
- Organic sensors
- Optical coatings (filters)
- Micro lenses

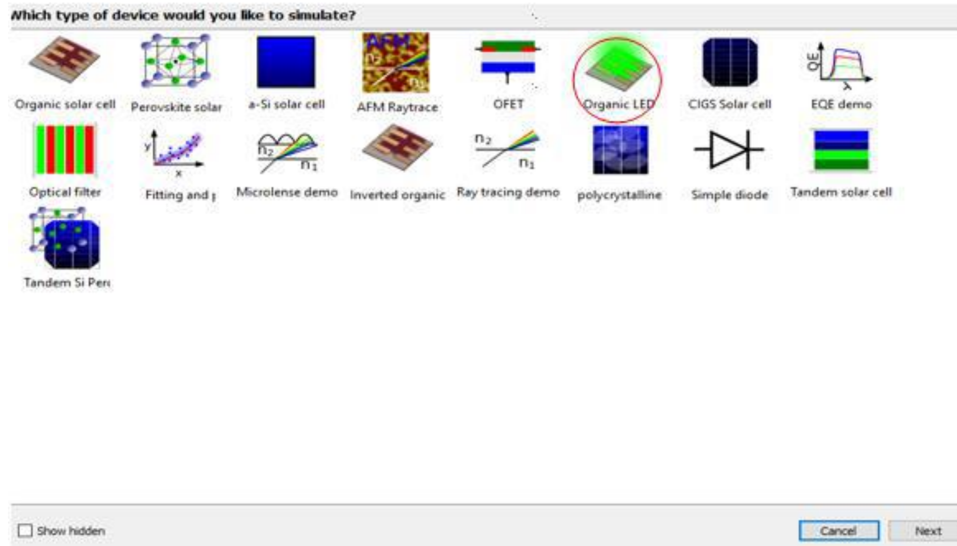

Figure V.14: Choice of the optoelectronic device for the simulation.

There are some materials that are not in Gpvdm, therefore we will have to create them. Adding the desired material from the icons (MATERIALS DATABASE) and (ADD MATERIAL) successively from the main window of Gpvdm containing the database (DATABASE).

This phase necessitates the use of the optical parameters we obtained from reference. The wavelength, absorption coefficient, and refractive index are the three parameters (see Figure V.15).

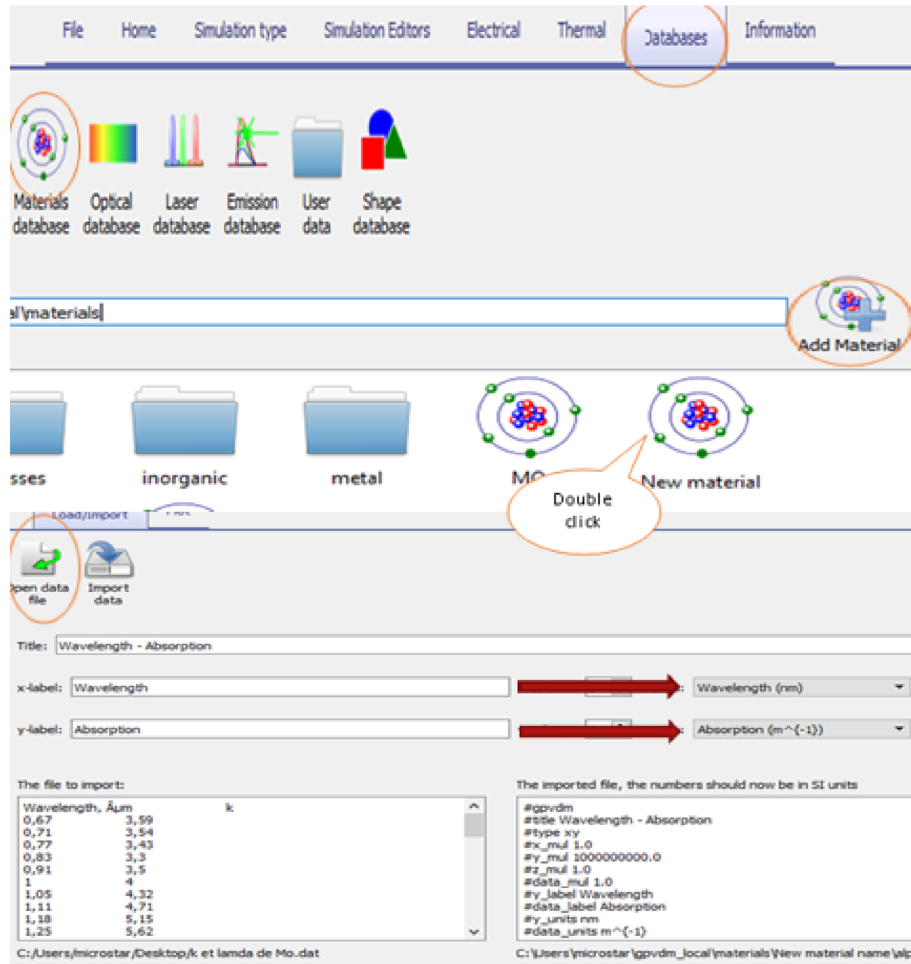

Figure V.15: Introduction of the optical parameters.

Then we get a window with specific characteristics that represents the layers of an LED (see Figure V.16). It is sufficient to adjust the layers to change the LED's parameters (LAYER EDITOR). This window displays the layer editor as well as information on the material's name, thickness, and the number of layers utilized in the LED structure. Layers can be chosen and set according to our requirements.

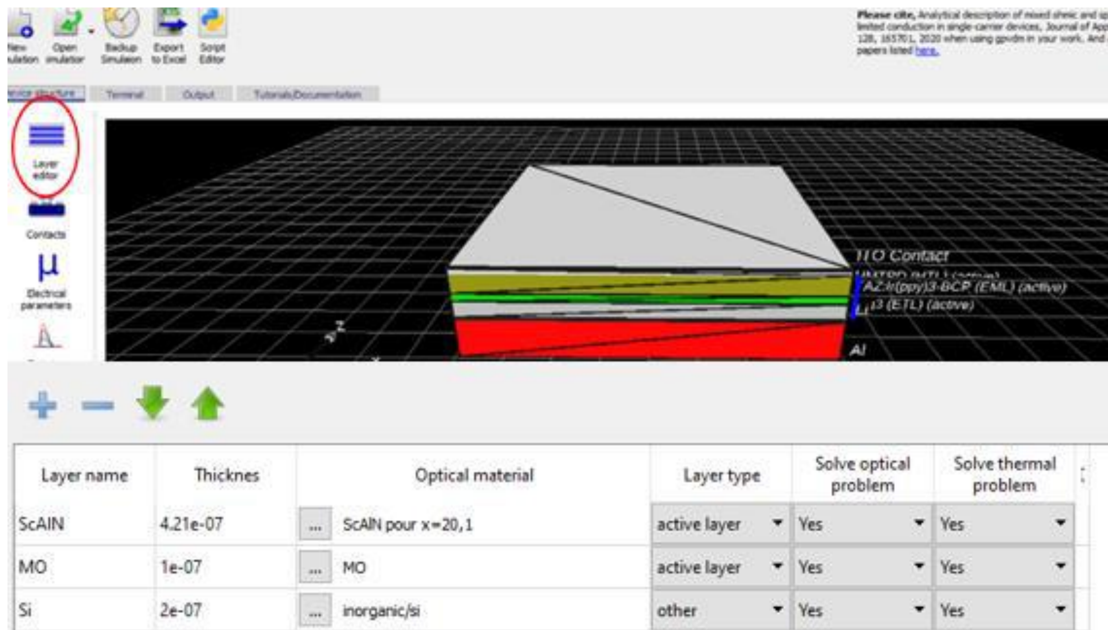

Figure V.16: The layer editor and the material types.

V.8 Results and Discussion

The simulation's findings are first displayed in a window that simulates the light emitted by the ScAlN-based LED that we simulated in the previous steps (see Figure III.17).

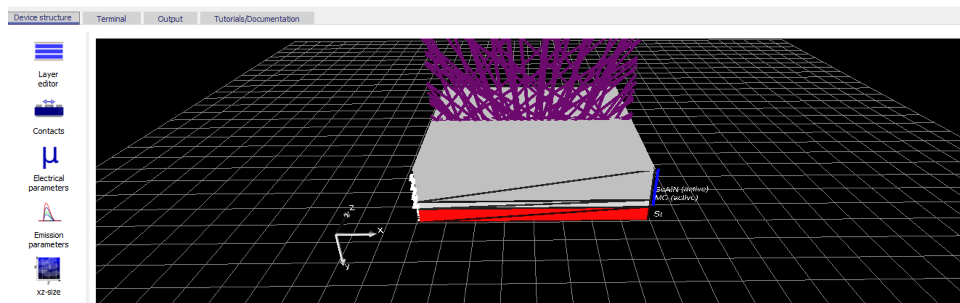

Figure V.17: The emitted light of a Sc-AlN based LED.

From then, we experimented with varying the percentage x of scandium in the LED: Sc-AlN structure.

This graph illustrates the influence of concentration on photon density and distribution over a concentration range of x = 0% to x=25.1%. For the x=0 percent case, Figures (V.18-19) show these variations as a function of wavelength and thickness.

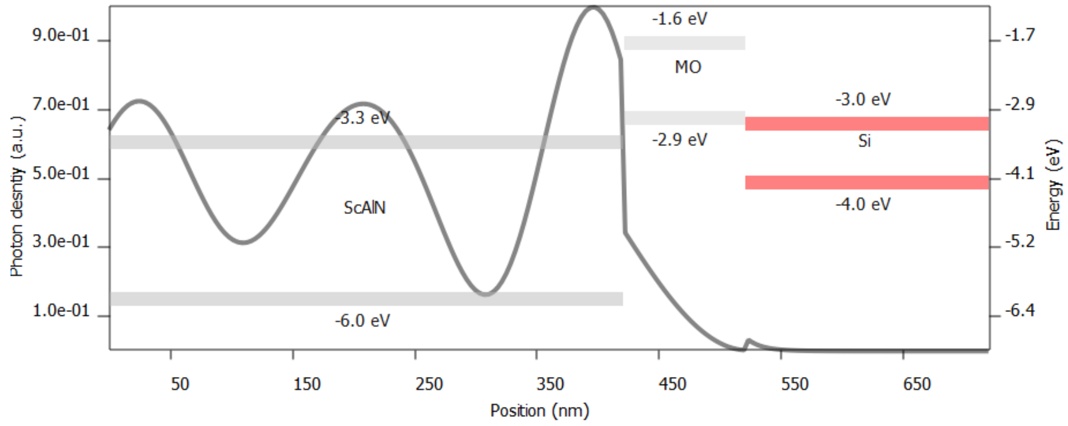

Figure V.18: Photon density for x=0%.

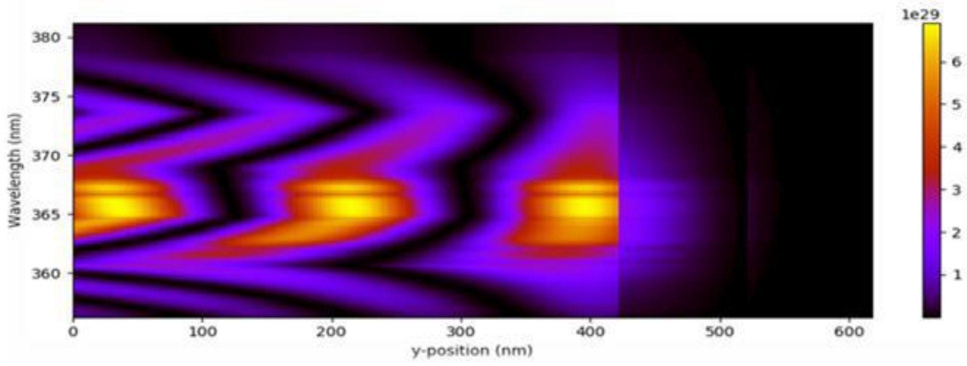

Figure V.19: The 2D photon distribution for x=0%

Figure V.20 depicts the evolution of this structure in three dimensions to highlight the three variables (density, wavelength, and thickness).

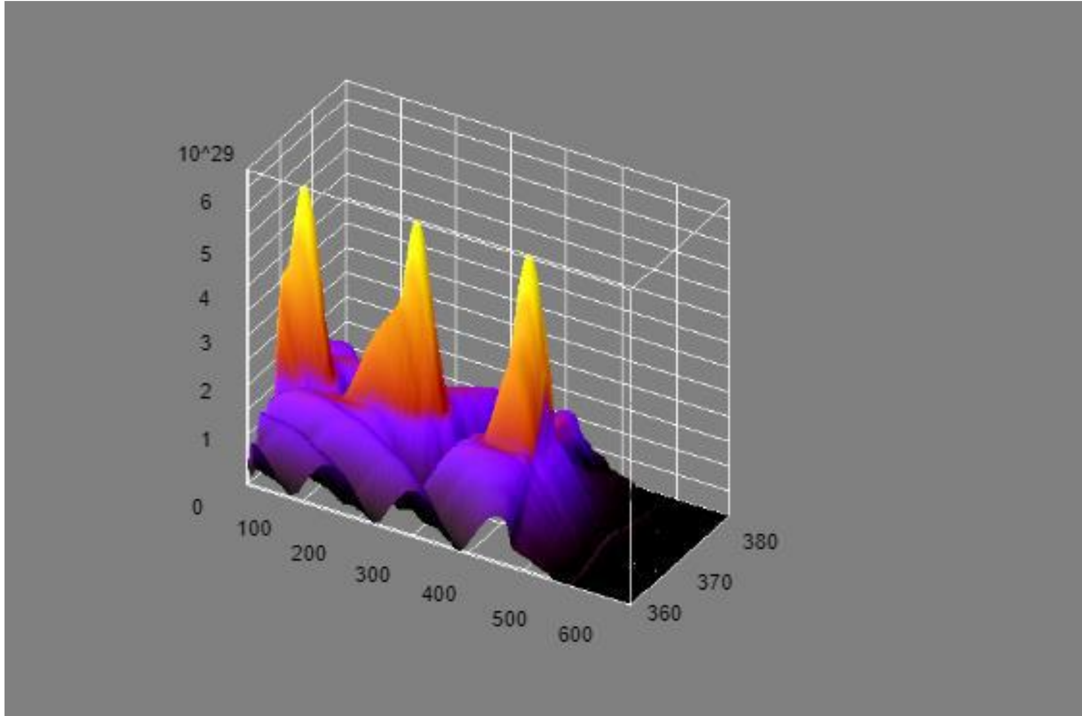

Figure V.20: 3D distribution of the photon density for x=0%

The following table shows the results for the different concentrations:

Table V.1: Results for the different concentrations

Photon density	2D Photon density distribution	3D Photon density distribution
x=0%	x=0%	x=0%
x=2%	x=2%	x=2%

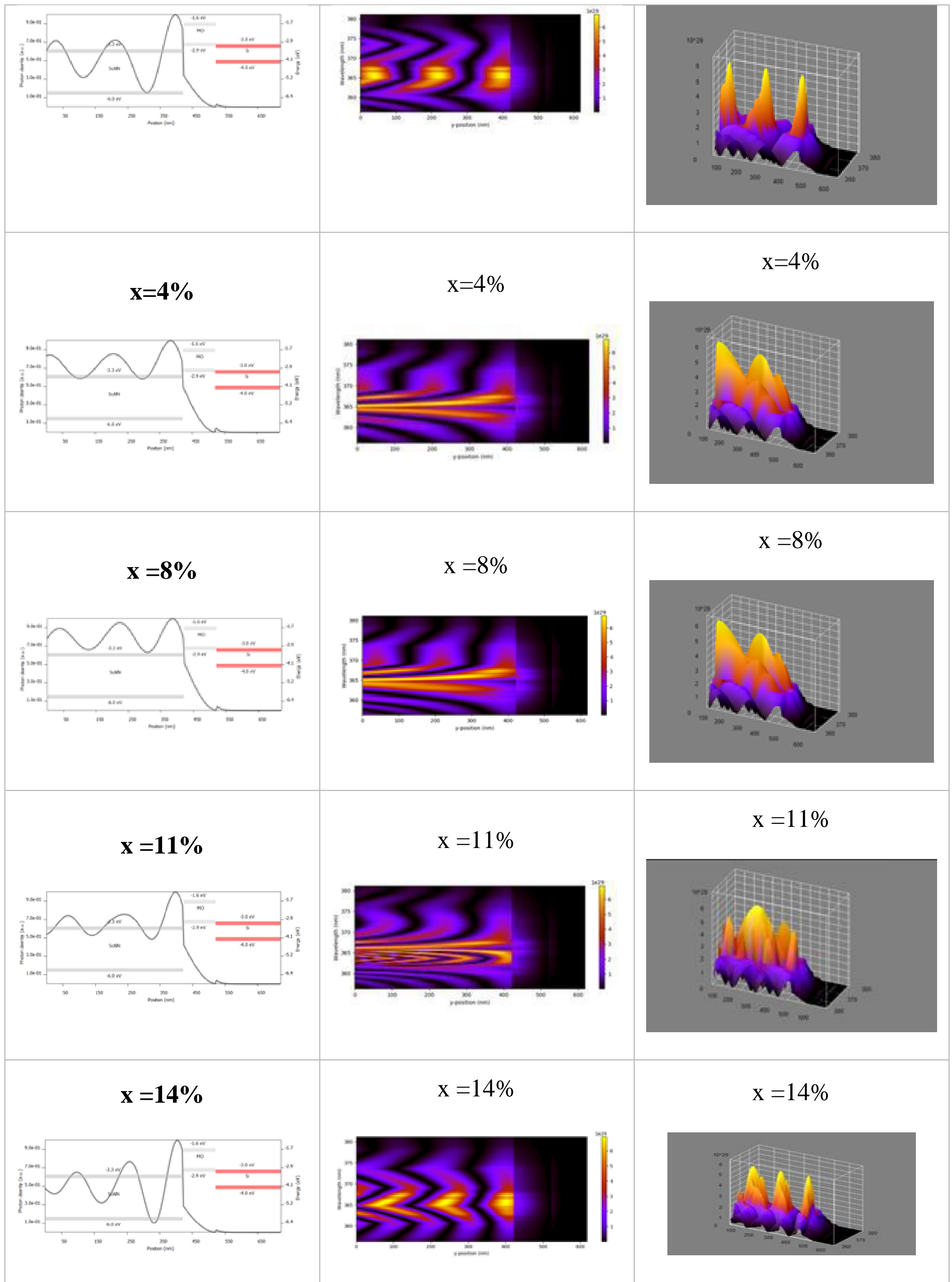
x=4%
x=4%
x=4%
x =8%
x =8%
x =8%
x =11%
x =11%
x =11%
x =14%
x =14%
x =14%

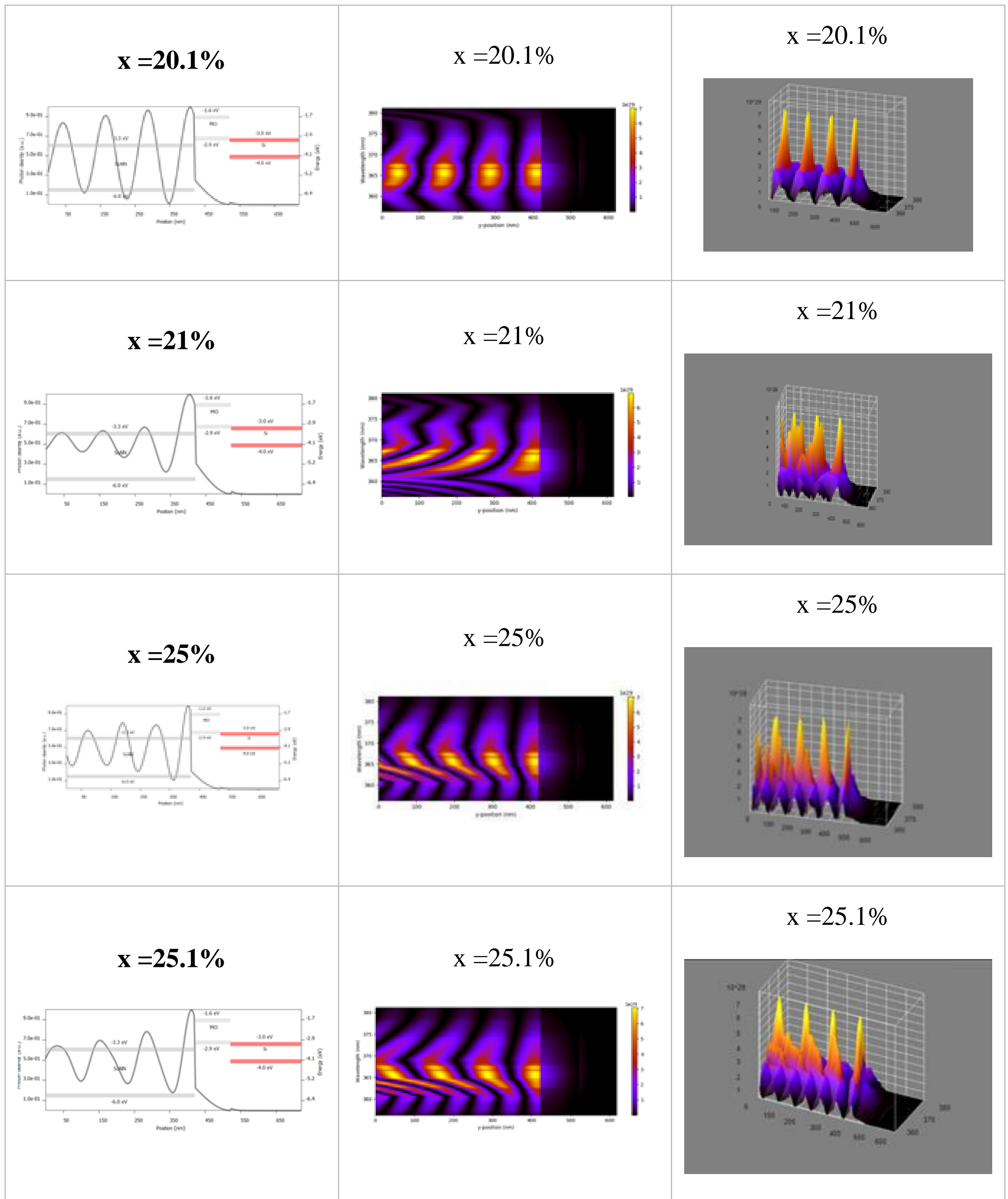

The photon distribution and density in 2D and 3D as a function of wavelength and position *y* (layer thicknesses) may be seen in the Figures above:

- ✓ As the scandium concentration x rises, the number of peaks rises with it.
- ✓ As the scandium concentration rises, the pitch (distance between the peaks) falls.
- ✓ With each rise in scandium concentration, the widening of the peaks grows sharper.
- ✓ The photon density has improved to a value of 7.1029, and this improvement is proportional to the scandium concentration.
- ✓ For the value of scandium x=20.1 percent, there is a photon distribution stability; this stability is due to saturation at the active layer.

Figure V.6 shows the LED layers as a band gap shift, with the thickness of each layer being 0.421 µm for the Sc-AlN layer, 0.100 µm for the Molybdenum layer, and 0.200 µm for the silicon substrate.

Because the distance between the hole's Fermi quasi-level and the edge of the electron band increases when the band gap moves, the electron density near the hole-rich contact decreases. In Figure V.7, the decline in electron population can be seen as an unpopulated dark zone. The exceedingly low carrier recombination rate causes the low electron density in these layers.

The other zones, on the other hand, have a high electron density, so positive charge carriers (holes) collide with negative charge carriers (electrons) and recombine under the emission of a photon that contains the energy that released the electron as well as the recombination of holes. The higher the material's band gap, the higher the photon's energy and the longer the wavelength of the light emitted.

V.9 Conclusion

From the obtained results it is safe to assume that ScAlN is a potential material for optoelectronic applications with a Sc (Scandium) ratio optimally at 25% we were able to simulate an LED response of the studied material at a wavelength of approximately 357nm. However, nm. However, this has room for improvement since the design lacks a top Electrode and only implemented the optical response of the studied material and the existing layers underneath. Giving the possibility of making a UV LED with a high flux output from wurtzite hexagonal c-planned Aluminum Scandium Nitride. The processing methods of the material could also be improved to enhance chip quality, thus the output

performance. Like what was cleared in the previous chapter the performance of the simulated chip increases with the scandium ratio until a certain percentage where the compound is not hexagonal ScAlN but either cubic ScAlN or separation of clusters of AlN and ScN what explains the drop in performance in the simulated chip.

.

VI. General conclusion

The goal of this project was to investigate and characterize thin films made of scandium aluminum nitride. Starting by investigating the structural and optical behavior of this system because the optical and structural mechanism of the ScAlN alloy is still a matter of debate.

Four groups of samples were characterized using various techniques to learn more about their structure, electronic, and optical characteristics. The Samples to achieve said purpose were prepared using Co-sputtering with two targets, which was done at various temperatures achieving scandium contents with varying percentages different crystal structures and thicknesses.

Prior to Studying the material for opto-electronical applications, confirmation of its properties was needed. For that purpose, multiple sets of samples were prepared and used. Four to be precise, each type of samples grown under different conditions, different multilayer layouts, and different Scandium percentages. Unfortunately, it was not possible to ensure epitaxial growth since Co-Sputtering does not offer high epitaxial growth, and MBE was not available at the execution time of the project. The results proved that the samples grown at 300°C were of better-quality Wurtzite c-oriented and almost monocrystalline compared to the room temperature growth. The first set of samples was used to figure out ScAlN material model for the deposition of the top electrodes and with bottom connections. This set of samples showed good quasi-monocrystalline behavior with a roughness in the order of 10 nm under SEM these results allowed the determination of ScAlN dielectric function using SE. The other sets of sample quality were not optimal, but it allowed us also to study the effects of connection layers and find the Band gap of the material and its lattice constants. We could conclude from this chapter that ScAlN in our samples grown with co-sputtering has a hexagonal structure up to approximately 22% then the material changes to cubic or separates into ScN and AlN making any samples with too high or too low percentages probably unusable for further investigations.

By using UV-Vis spectroscopy to analyze five samples with a molybdenum interlayer in the second group, we discovered that the ScAlN has a higher reflectance than the

molybdenum, which is an absorbent material in the (250-400 nm) spectrum and has a high reflectivity. Because ScAlN layers are thicker, there is greater oscillation in the UV band (250–400 nm) which is understandable since ScAlN as a semiconductor is transparent in the above-mentioned range. Thus, the expected multiple wave interferences witnessed due to the layer thickness.

The optical band gap was then estimated using the Kubelka-Munk equation, the results showed that the lattice constant gets smaller as the scandium percentage rises. Therefore, the binding energy and scandium concentration in the ultraviolet region are inversely proportional to a decrease in the distance between the conduction band and valance band, which leads to a decrease in the band gap. Only small traces of carbon can be found because it was removed by sputtering to a relatively high degree.

A significant amount of oxygen can be found on the sample. To find that much oxygen after such a long sputtering time could be a hint for oxygen incorporation during the manufacturing process of the sample itself. This incorporation of oxygen into the sample can be seen in the Al 2p peak as well as the Sc 2p peak.

The O1s core level state exhibits two components: Under consideration of literature about Al oxides as well as the different electronegativity of Sc and Al.

To know the variation of scandium content on the optical parameters we characterized the same samples by V-VASE ellipsometry. We used Cauchy oscillator to model the refractive index n (λ) because we expected the layer to be transparent up to at least 5eV. We found that ScAlN has anomalous dispersion because the index will decrease toward shorter wavelengths and normal dispersion usually occurs for transparent material (AlN). In addition, Scandium content proportional with a refractive index and inverse proportional with bandgap.

The absorption coefficient k is inferior to the reflective index n that means scandium aluminum nitride layers is dielectric material so we can used ScAlN for semiconductors devices and microelectronic applications.

To determine the lattice constant c in the hexagonal crystal we used X-ray diffraction and we found that the lattice constant is increasing (rises) because of the lattice's tendency to metastable h-ScN phase(scandium content is less than 24%) , reaches a maximum at 5.02[Å] then c lattice going down by progressive incorporation of scandium (more than 24%) This is where the transition from the wurtzite to the cubic structure begins.

from characterizing 10 samples by spectroscopic ellipsometry we got the curves of Ψ and Δ according to the photon energy to different incidence angles. We observed a pseudo-periodic variation in ellipsometry spectra depending on the photon energy. This variation is due to interferences resulting from reflections at the two interfaces Air /thin film/substrate. It is noted that when the film thickness increases, the number of oscillations increases accordingly.

In the UV region (>3.5 eV) we observe that the oscillation decreases with the increase of energy and that is due to the optical path difference being very superior to the wavelength.

We characterized six samples by infrared spectroscopy, it allows making a point about the optical phonon modes in $Sc_xAl_{1-x}N$-alloys, influenced by Scandium content x.

We obtained that for the phonons of the E_2^{high}, the peak position k decreases linearly with increasing scandium content x in the samples, with the course of the E_2^{high} mode has a steeper slope. A1 (LO) modes exhibit higher frequencies, and the atomic displacement takes place along the C axis of ScAlN.

In addition, infrared spectroscopy provides an equivalent to XRD over the half-widths of the decrease in crystal lattice quality with increasing x. The E_2^{High} and A1 (LO) modes are also visible in the infrared measurements for low scandium concentrations x.

From the obtained results it is safe to assume that ScAlN is a potential material for optoelectronic applications with a Sc (Scandium) ratio optimally at 25% we were able to simulate an LED response of the studied material at a wavelength of approximately 357nm. However, However, this has room for improvement since the design lacks a top Electrode and only implemented the optical response of the studied material and the existing layers underneath. Giving the possibility of making a UV LED with a high flux

output from wurtzite hexagonal c-planned Aluminum Scandium Nitride. The processing methods of the material could also be improved to enhance chip quality, thus the output performance. Similar to what was cleared in the previous chapter the performance of the simulated chip increases with the scandium ratio until a certain percentage where the compound is not hexagonal ScAlN but either cubic ScAlN or separation of clusters of AlN and ScN.

VII. References

References

[1] Samuelson, L. (2003). Self-forming nanoscale devices. Materials today, 6(10), 22-31.

[2] Pawlow, P. (1909). The dependency of the melting point on the surface energy of a solid body. Z. phys. Chem, 65(5), 545-548.

[3] Canham, L. (2000). Gaining light from silicon. Nature, 408(6811), 411-412.

[4] Chen, M. S., & Goodman, D. W. (2004). The structure of catalytically active gold on titania. science, 306(5694), 252-255.

[5] Björk, M. T., Thelander, C., Hansen, A. E., Jensen, L. E., Larsson, M. W., Wallenberg, L. R., & Samuelson, L. (2004). Few-electron quantum dots in nanowires. Nano Letters, 4(9), 1621-1625.

[6] Mårtensson, T. (2008). Semiconductor Nanowires: Epitaxy and Applications. Lund University.

[7] Han, T. (2008). Optical Properties of Low Dimensional Semiconductor Materials (Doctoral dissertation, KTH).

[8] Ashcroft, N. W., & Mermin, N. D. (1976). Solid State Physics (Saunders College, Philadelphia). Google Scholar, 404.

[9] Ridley, B. K. (2013). Quantum processes in semiconductors. Oxford university press.

[10] Hauge, H. I. T. (2017). Growth of hexagonal group-IV semiconductor nanowires.

[11] Khashoqji, M. M. (2016). Structural Characterisation of Novel Poly-aryl Compounds. The University of Manchester (United Kingdom).

[12] Speck, J. S.; Chichibu, S. F. (2009). Nonpolar and Semipolar Group III Nitride-Based Materials. MRS Bulletin, 34(5), 304–312. doi:10.1557/mrs2009.91

[13] Acharya, A. R. (2014). Group III–nitride semiconductors: preeminent materials for modern electronic and optoelectronic applications. Himalayan Physics, 5, 22-26.

[14] T. L. Tansley, in Group III nitrides, ed J. H. Edgar, INSPEC, UK pp.35-42 (1994).

[15] Song, J. J., Shan, W., & Gil, B. (1998). Group III nitride semiconductor compounds: physics and applications.

[16] Perlin, P., Jauberthie-Carillon, C., Itie, J. P., San Miguel, A., Grzegory, I., & Polian, A. (1992). Raman scattering and x-ray-absorption spectroscopy in gallium nitride under high pressure. Physical Review B, 45(1), 83.

[17] Xia, Q., Xia, H., & Ruoff, A. L. (1993). Pressure-induced rocksalt phase of aluminum nitride: A metastable structure at ambient condition. Journal of applied physics, 73(12), 8198-8200.

[18] Bernardini, F., & Fiorentini, V. (1999). Spontaneous versus piezoelectric polarization in III–V nitrides: conceptual aspects and practical consequences. physica status solidi (b), 216(1), 391-398.

[19] Bernardini, F., & Fiorentini, V. (2001). Nonlinear macroscopic polarization in III-V nitride alloys. Physical Review B, 64(8), 085207.

[20] Ponce, F. A., & Bour, D. P. (1997). Nitride-based semiconductors for blue and green light-emitting devices. nature, 386(6623), 351-359.

[21] Singh, D. K., Roul, B., Pant, R., Chowdhury, A. M., Nanda, K. K., & Krupanidhi, S. B. (2020). Different types of band alignment at MoS2/ (Al, Ga, In) N heterointerfaces. Applied Physics Letters, 116(25), 252102.

[22] Singh, D. K., Roul, B. K., Nanda, K. K., & Krupanidhi, S. B. (2021). Group III-Nitrides and Their Hybrid Structures for Next-Generation Photodetectors. Light-Emitting Diodes and Photodetectors: Advances and Future Directions, 149.

[23] Goto, T., Tsuneyoshi, J., Kaya, K., & Hirai, T. (1992). Preferred orientation of AlN plates prepared by chemical vapour deposition of AlCl3+ NH3 system. Journal of materials science, 27(1), 247-254.

[24] A. Dollet, Y. Casaux, M. Matecki, and R. Rodriguez-Clemente. (2002). Chemical vapour deposition of polycrystalline AlN lms from AlCl3-NH3 mixtures: II Surface

morphology and mechanisms of preferential orientation at low-pressure. Thin Solid Films, 406(1-2) :118131.

[25] Taniyasu, Y., Kasu, M., & Makimoto, T. (2006). An aluminium nitride light-emitting diode with a wavelength of 210 nanometres. nature, 441(7091), 325-328.

[26] Yeh, C. Y., Lu, Z. W., Froyen, S., & Zunger, A. (1992). Zinc-blende–wurtzite polytypism in semiconductors. Physical Review B, 46(16), 10086.

[27] Claudel, A. (2009). Elaboration et caractérisation de couches de nitrure d'aluminium AlN par CVD haute température en chimie chlorée (Doctoral dissertation, Institut National Polytechnique de Grenoble-INPG).

[28] He, M., Cheng, N., Zhou, P., Okabe, H., & Halpern, J. B. (1998). Preparation of nearly oxygen-free AlN thin films by pulsed laser deposition. Journal of Vacuum Science & Technology A: Vacuum, Surfaces, and Films, 16(4), 2372-2375.

[29] Vispute, R. D., Narayan, J., Wu, H., & Jagannadham, K. (1995). Epitaxial growth of AlN thin films on silicon (111) substrates by pulsed laser deposition. Journal of applied physics, 77(9), 4724-4728.

[30] Morita, M., Uesugi, N., Isogai, S., Tsubouchi, K., & Mikoshiba, N. (1981). Epitaxial growth of aluminum nitride on sapphire using metalorganic chemical vapor deposition. Japanese Journal of Applied Physics, 20(1), 17.

[31] Xie, J. L., & Wickramanayaka, S. (2014, December). Effect of process pressure on PVD AlN thin film. In 2014 IEEE 16th Electronics Packaging Technology Conference (EPTC) (pp. 849-850). IEEE.

[32] Martin, P. M. (2009). Handbook of deposition technologies for films and coatings: science, applications, and technology. William Andrew.

[33] Xiong, C., Pernice, W. H., & Tang, H. X. (2012). Low-loss, silicon integrated, aluminum nitride photonic circuits and their use for electro-optic signal processing. Nano letters, 12(7), 3562-3568.

[34] Stegmaier, M., & Pernice, W. H. (2013). Mode control and mode conversion in nonlinear aluminum nitride waveguides. Optics Express, 21(22), 26742-26761.

[35] Giba, A. E. (2018). Rare earth-doped aluminum nitride thin films for optical applications (Doctoral dissertation, Université de Lorraine; Universität des Saarlandes).

[36] Barrett, S. D., & Dhesi, S. S. (2001). The structure of rare-earth metal surfaces. World Scientific.

[37] Atwood, D. A. (Ed.). (2013). The rare earth elements: fundamentals and applications. John Wiley & Sons.

[38] Li, T., Mastro, M., & Dadgar, A. (Eds.). (2010). III–V compound semiconductors: integration with silicon-based microelectronics. CRC press.

[39] Kita, T., Ishizu, Y., Tsuji, K., Harada, Y., Chigi, Y., Nishimoto, T., ... & Izumi, H. (2015). Thermal annealing effects on ultra-violet luminescence properties of Gd doped AlN. Journal of Applied Physics, 117(16), 163105.

[40] Lozykowski, H. J., Jadwisienczak, W. M., Bensaoula, A., & Monteiro, O. (2005). Luminescence and excitation mechanism of Pr, Eu, Tb and Tm ions implanted into AlN. Microelectronics journal, 36(3-6), 453-455.

[41] Liu, T. C., Kominami, H., Greer, H. F., Zhou, W., Nakanishi, Y., & Liu, R. S. (2012). Blue emission by interstitial site occupation of Ce3+ in AlN. Chemistry of Materials, 24(17), 3486-3492.

[42] Wang, W., Zhang, P., Wang, X., Lei, X., Ding, H., & Yang, H. (2015). Bifunctional AlN: Tb semiconductor with luminescence and photocatalytic properties. RSC advances, 5(110), 90698-90704.

[43] Weingärtner, R., Erlenbach, O., Winnacker, A., Welte, A., Brauer, I., Mendel, H., ... & Zanatta, A. R. (2006). Thermal activation, cathodo-and photoluminescence measurements of rare earth doped (Tm, Tb, Dy, Eu, Sm, Yb) amorphous/nanocrystalline AlN thin films prepared by reactive rf-sputtering. Optical Materials, 28(6-7), 790-793.

[44] Wieg, A. T., Grossnickle, M. J., Kodera, Y., Gabor, N. M., & Garay, J. E. (2016). Nd: AlN polycrystalline ceramics: A candidate media for tunable, high energy, near IR lasers. Applied Physics Letters, 109(12), 121901.

[45] Koubaa, T., Dammak, M., Kammoun, M., Jadwisienczak, W. M., Lozykowski, H. J., & Anders, A. (2009). Spectra and energy levels of Yb 3+ in AlN. Journal of Applied Physics, 106(1), 013106.

[46] Wieg, A. T., Penilla, E. H., Hardin, C. L., Kodera, Y., & Garay, J. E. (2016). Broadband white light emission from Ce: AlN ceramics: High thermal conductivity down-converters for LED and laser-driven solid-state lighting. APL Materials, 4(12), 126105.

[47] Zanatta, A. R., Ribeiro, C. T. M., & Jahn, U. (2005). Optoelectronic and structural characteristics of Er-doped amorphous AlN films. Journal of applied physics, 98(9), 093514.

[48] Merkle, L. D., Sutorik, A. C., Sanamyan, T., Hussey, L. K., Gilde, G., Cooper, C., & Dubinskii, M. (2012). Fluorescence of Er 3+: AlN polycrystalline ceramic. Optical Materials Express, 2(1), 78-91.

[49] Ishikawa, R., Lupini, A. R., Oba, F., Findlay, S. D., Shibata, N., Taniguchi, T., ... & Pennycook, S. J. (2014). Atomic structure of luminescent centers in high-efficiency Ce-doped w-AlN single crystal. Scientific reports, 4(1), 1-5.

[50] Lavi, R., Jackel, S., Tzuk, Y., Winik, M., Lebiush, E., Katz, M., & Paiss, I. (1999). Efficient pumping scheme for neodymium-doped materials by direct excitation of the upper lasing level. Applied Optics, 38(36), 7382-7385.

[51] Sangla, D., Balembois, F., & Georges, P. (2009). Nd: YAG laser diode-pumped directly into the emitting level at 938 nm. Optics express, 17(12), 10091-10097.

[52] Ralf Higgelke., Is Scandium Aluminum Nitride better as GaN,elektroniket.de, 21. Januar 2019

[53] Schuster, J. C., & Bauer, J. (1985). The ternary systems Sc_Al_N and Y_Al_N. Journal of the Less Common Metals, 109(2), 345-350.

[54] Akiyama, M., Kano, K., & Teshigahara, A. (2009). Influence of growth temperature and scandium concentration on piezoelectric response of scandium aluminum nitride alloy thin films. Applied Physics Letters, 95(16), 162107.

[55] Tsui, H. C. L. (2016). Characterisation of scandium-based III-nitride thin films.

[56] Tonisch, K. (2010). ScAlN aus Alternative zu AlN: Herstellung und Eigenschaften gesputterter ScAlN-Schichten. PhD Thesis, Technische Universität Ilmenau.

[57] Zhang, S., Holec, D., Fu, W. Y., Humphreys, C. J., & Moram, M. A. (2013). Tunable optoelectronic and ferroelectric properties in Sc-based III-nitrides. Journal of Applied Physics, 114(13), 133510.

[58] Xu, Y. N., & Ching, W. Y. (1993). Electronic, optical, and structural properties of some wurtzite crystals. Physical Review B, 48(7), 4335.

[59] Wang, Q., Lu, Y., Fung, S., Jiang, X., Mishin, S., Oshmyansky, Y., & Horsley, D. A. (2016). Scandium doped aluminum nitride based piezoelectric micromachined ultrasound transducers. In Proc. Solid-State Sens., Actuators, Microsyst. pp. 436-439.

[60] Bartoli, F., Moutaouekkil, M., Streque, J., Pigeat, P., Hage-Ali, S., Boulet, P., ... & Talbi, A. (2017, October). Theoretical and experimental study of ScAlN/Sapphire structure-based SAW sensor. In 2017 IEEE SENSORS (pp. 1-3). IEEE.

[61] Bernard, J. E., & Zunger, A. (1987). Electronic structure of ZnS, ZnSe, ZnTe, and their pseudobinary alloys. Physical Review B, 36(6), 3199.

[62] Siegfried, S. A., Altynbaev, E. V., Chubova, N. M., Dyadkin, V., Chernyshov, D., Moskvin, E. V., ... & Grigoriev, S. V. (2015). Controlling the Dzyaloshinskii-Moriya interaction to alter the chiral link between structure and magnetism for Fe 1− x Co x Si. Physical Review B, 91(18), 184406.

[63] Cen, J. W., & Xu, J. L. (2010). Performance evaluation and flow visualization of a MEMS based vaporizing liquid micro-thruster. Acta Astronautica, 67(3-4), 468-482.

[64] Ravish Gupta, Jigyasha Maru, N. Pannaga. (2013). MEMS Technology & Application in Defense Navigation System. International Journal of Engineering Research & Technology (IJERT). ISSN: 2278-0181

[65] http://www.dlp.com/.

[66] Noé, C. (2014). Photobiomodulation en dermatologie : Comprendre et utiliser les LED. Doin.

[67] Eric Strandberg, LC & Jeff Robbins, LC, MIES. (2012) . THE BASICS of LEDs. LIGHTING DESIGN LAB 2915 – 4th Avenue South Seattle, WA 98119

[68] Epp, J. (2016). X-ray diffraction (XRD) techniques for materials characterization. In Materials characterization using nondestructive evaluation (NDE) methods (pp. 81-124). Woodhead Publishing.

[69] Verma, S. K. (2019). Engineered Nanomaterials and Phytonanotechnology:Challenges for plant Sustainability. Vol.87.Elsevier,

[70] Anatonis Nanakoudis. (2019).What is SEM? Scanning Electron Microscopy Explained. Thermo Fisher SCIENTIFIC.

[71] Ismail, A. F., Khulbe. C. K., Matsuura, T. (2019). RO membrane characterization. Reverse Osmosis; Elsevier: Amsterdam, the Netherlands, 57-90.

[72] Dincer,I. (2018).Comprehensive energy systems. Elsevier.

[73] Woollam, J. A. Spectroscopic Ellipsometry-Data Acquisition and Analysis. A Guide to use WVASE, 32. (2006).

[74] Rahman, M. S., Garcia, C. D., Bhalla, A., & Guo, R. (2014, September). Optical characterization of ferroelectric PZT thin films by variable angle spectroscopic ellipsometry. In Photonic Fiber and Crystal Devices: Advances in Materials and Innovations in Device Applications VIII (Vol. 9200, pp. 35-43). SPIE.

[75] Tsui, H. C. L. (2016). Characterisation of scandium-based III-nitride thin films.

[76] Gamaaz, A. (2002). Étude des carbures, nitrures et carbonitrures de titane par spectroscopie XPS, thèse, université Ferhat Abbas-Sétif.

[77] Haasch, R.T. (2014).X-ray photoelectron spectroscopy (XPS) and auger electron spectroscopy (AES). In Practical Materials Characterization (pp.93-132).New York, NY: Springer New York.

[78] H. P. Loebl, M. Klee, C. Metzmacher, W. Brand, R. Milsom, and P. Lok, “Piezoelectric thin AlN films for bulk acoustic wave (BAW) resonators,” Mater. Chem. Phys., vol. 79, nos. 2–3, pp. 143–146, Apr. 2003.

[79] Martín-Palma, R. J., & Lakhtakia, A. (2013). Vapor-deposition techniques. In Engineered Biomimicry (pp. 383-398). Elsevier Inc.

[80] Jimenez, F. J. (2012). Comprehensive Simulation of Sputter Deposition (Doctoral dissertation, University of Alberta).

[81] Xi, L., Zhang, H., Xie, X., Wang, E., Lin, X., Song, Y., …& Chen, G. (2022). Structure end Optical Properties of AlN Crystals Grown by metal Nitride Vapor Phase Epitaxy with different V/III Ratio. ACSomega,7(27),23497- 23502.

127

[82] Wang,Q., Lu., Mishin, S., Oshmyansky, Y., &Horsley,D.A.(2017). Design, Fabrication, and Characterization of Scandium Aluminum Nitride-Based Piezoelectric Micromachined. Ultrasonic Transducers. Journal of microelectromechanical systems,26(5), 1132-1139.

[83] Milton, G. W. (1981). Bounds on the complex permittivity of a two-component composite material. Journal of Applied Physics, 52(8), 5286-5293.

[84] Fodor, B., Kozma, P., Burger, S., Fried, M., & Petrik, P. (2016). Effective medium approximation of ellipsometric response from random surface roughness simulated by finite-element method. Thin Solid Films, 617, 20-24.

[85] Khan, M. A., Bao, J. F., Bao, F. H., & Zhou, X. (2019). Concentric split aluminum with silicon-aluminum nitride annular rings resonators. Micromachines, 10(5), 296.

[86] Čermák, M., Vohánka, J., Ohlídal, I., & Franta, D. (2018). Optical quantities of multi-layer systems with randomly rough boundaries calculated using the exact approach of the Rayleigh–Rice theory. Journal of Modern Optics, 65(14), 1720-1736.

[87] Ohlídal, I., Vohánka, J., Čermák, M., & Franta, D. (2017). Optical characterization of randomly microrough surfaces covered with very thin overlayers using effective medium approximation and Rayleigh–Rice theory. Applied Surface Science, 419, 942-956.

[88] J.A. Woollam, "Spectroscopic Ellipsometry-Data Acquisition and Anal-ysis," A Guide to Use WVASE, 32, 2006.

[89] Bergner, B. C., Germer, T. A., & Suleski, T. J. (2010). Effective medium approximations for modeling optical reflectance from gratings with rough edges. JOSA A, 27(5), 1083-1090.

[90] Garnett, J. M. (1904). XII. Colours in metal glasses and in metallic films. Philosophical Transactions of the Royal Society of London. Series A, Containing Papers of a Mathematical or Physical Character, 203(359-371), 385-420.

[91] Gutiérrez, Y., Ortiz, D., Alcaraz de la Osa, R., Saiz, J. M., González, F., & Moreno, F. (2019). Electromagnetic effective medium modelling of composites with metal-semiconductor core-shell type inclusions. Catalysts, 9(7), 626.

[92] Bohren, C. F., & Huffman, D. R. (2008). Absorption and scattering of light by small particles. John Wiley & Sons.

[93] Lee, Y. J., Kim, J. H., Ham, S., Ju, B. K., & Choi, W. K. (2018). Modeling large permittivity of poly (vinylidenefluoride-co-trifluoroethylene) and nanospring single-walled carbon nanotube-polyvinylpyrrolidone nanocomposites. AIP Advances, 8(8), 085113.

[94] Ciesielski, A., Skowronski, L., Pacuski, W., & Szoplik, T. (2018). Permittivity of Ge, Te and Se thin films in the 200–1500 nm spectral range. Predicting the segregation effects in silver. Materials Science in Semiconductor Processing, 81, 64-67.

[95] Aspnes, D. E., Theeten, J. B., & Hottier, F. (1979). Investigation of effective-medium models of microscopic surface roughness by spectroscopic ellipsometry. Physical Review B, 20(8), 3292.

[96] Slimi, Y., Bouafia, M., & Arres, A. (2021). Evaluation of scandium ratio effect on the permittivity (ε) of Sc-AlN by EMT modeling and spectroscopic ellipsometry measurement. Optik, 238, 166757.

[97] Aspnes, D. E. (1982). Local-field effects and effective-medium theory: a microscopic perspective. American Journal of Physics, 50(8), 704-709.

[98] Sigrist, M., Chassaing, G., François, J. C., Antonangeli, F., Zema, N., & Piacentini, M. (1987). Optical properties of scandium thin films. Physical Review B, 35(8), 3760.

[99] Pastrňák, J., & Roskovcová, L. (1966). Refraction index measurements on AlN single crystals. physica status solidi (b), 14(1), K5-K8.

[100] MacKenzie, R. C., Kirchartz, T., Dibb, G. F., & Nelson, J. (2011). Modeling nongeminate recombination in P3HT: PCBM solar cells. The Journal of Physical Chemistry C, 115(19), 9806-9813.

[101] MacKenzie, R. C., Shuttle, C. G., Chabinyc, M. L., & Nelson, J. (2012). Extracting microscopic device parameters from transient photocurrent measurements of P3HT: PCBM solar cells. Advanced Energy Materials, 2(6), 662-669.

[102] Moss, T. S. (1950). A relationship between the refractive index and the infra-red threshold of sensitivity for photoconductors. Proceedings of the Physical Society. Section B, 63(3), 167.

[103] Kumar, V., & Singh, J. K. (2010). Model for calculating the refractive index of different materials.

[104] Curie, J., & Curie, P. (1880). Développement par compression de l'électricité polaire dans les cristaux hémièdres à faces inclinées. Bulletin de minéralogie, 3(4), 90-93.

[105] Curie, J., & Curie, P. (1881). Contractions et dilatations produites par des tensions électriques dans les cristaux hémièdres à faces inclinées. Compt. Rend, 93, 1137-1140.

[106] Lew Yan Voon, L. C., & Willatzen, M. (2011). Electromechanical phenomena in semiconductor nanostructures. Journal of Applied Physics, 109(3), 3.

[107] Jaffe, H. (1958). Piezoelectric ceramics. Journal of the American Ceramic Society, 41(11), 494-498.

[108] Tsui, H. C. L. (2016). Characterisation of scandium-based III-nitride thin films.

[109] Bernardini, F., Fiorentini, V., & Vanderbilt, D. (1997). Spontaneous polarization and piezoelectric constants of III-V nitrides. Physical Review B, 56(16), R10024.

[110] Guy, I. L., Muensit, S., & Goldys, E. M. (1999). Extensional piezoelectric coefficients of gallium nitride and aluminum nitride. Applied Physics Letters, 75(26), 4133-4135.

[111] Wright, A. F. (1997). Elastic properties of zinc-blende and wurtzite AlN, GaN, and InN. Journal of Applied physics, 82(6), 2833-2839.

[112] Ghannam, R. Solar Energy Research in the Engineering Design Research Group.

[113] Brûlé, Y. (2016). Méthode des Eléments Finis pour les nanostructures métalliques : application au filtrage spectral dans le visible et extension au calcul modal en présence de dispersion (Doctoral dissertation, Ecole Centrale Marseille).

[114] Tang, Z., Le Menach, Y., Creusé, E., Nicaise, S., Piriou, F., & Nemitz, N. (2013). Residual and equilibrated error estimators for magnetostatic problems solved by finite element method. IEEE transactions on magnetics, 49(12), 5715-5723.

[115] Wiklund, H. (2006). Numerical calculations of optical structures using FEM. [41] George, P. L., & Frey, S. (2008). Mesh Generation. John Willey & Sons. Inc., New Jersey.

[116] GEORGE, P. L. ET FREY, S. (2008). Mesh Generation. John Willey & Sons. Inc., New Jersey,

[117] Filipiak, M. (1996). Mesh Generation, Version 1.0. Technology Watch Report, Edinburgh Parallel Computing Centre, the University of Edinburgh.

[118] Mavriplis, D. J. (1995). An advancing front Delaunay triangulation algorithm designed for robustness. Journal of Computational Physics, 117(1), 90-101.

[119] Du, Q., & Wang, D. (2006). Recent progress in robust and quality Delaunay mesh generation. Journal of Computational and Applied Mathematics, 195(1-2), 8-23.

[120] Nanjappa, A. (2012). Delaunay Triangulation in R3 on the GPU.

[121] Dinh, V. Q. (2016). Vers une simulation par éléments finis en temps réel pour le génie électrique (Doctoral dissertation, Université Grenoble Alpes (ComUE)).

[122] Ho-Le, K. (1988). Finite element mesh generation methods: a review and classification. Computer-aided design, 20(1), 27-38.

[123] Delone, B. N. (1934). Sur la sphere vide. Bull. Acad. Science USSR: Class Sci. Math., 793-800.

[124] Ohlídal, I., Franta, D., & Nečas, D. (2017). Ellipsometric and reflectometric characterization of thin films exhibiting thickness non-uniformity and boundary roughness. Applied Surface Science, 421, 687-696.

[125] Franta, D., & Ohlídal, I. (2005). Comparison of effective medium approximation and Rayleigh–Rice theory concerning ellipsometric characterization of rough surfaces. Optics communications, 248(4-6), 459-467.

[126] Čermák, M., Vohánka, J., Ohlídal, I., & Franta, D. (2018). Optical quantities of multi-layer systems with randomly rough boundaries calculated using the exact approach of the Rayleigh–Rice theory. Journal of Modern Optics, 65(14), 1720-1736.

[127] Aspnes, D. E., Theeten, J. B., & Hottier, F. (1979). Investigation of effective-medium models of microscopic surface roughness by spectroscopic ellipsometry. Physical Review B, 20(8), 3292.

[128] Blanco, J. R., & McMarr, P. J. (1991). Roughness measurements of Si and Al by variable angle spectroscopic ellipsometry. Applied optics, 30(22), 3210-3220